

Research

DECOVALEX-THMC Project

Task A

Influence of near field coupled THM phenomena on the performance of a spent fuel repository

Report of Task A1

Edited by:

Son Nguyen, Canadian Nuclear Safety Commission, Canada
Lanru Jing, Royal Institute of Technology, Sweden

February 2007

Research

DECOVALEX-THMC Project

Task A

Influence of near field coupled THM phenomena on the performance of a spent fuel repository

Report of Task A1

Preliminary scoping calculations

Edited by

Son Nguyen, Canadian Nuclear Safety Commission, Canada

Lanru Jing, Royal Institute of Technology, Sweden

With contributions from:

Lennart Börgesson, Clay Technology AB, Sweden

Masakazu Chijimatzu, Hazama Corporation, Japan

Petri Jussila, Helsinki University of Technology, Finland

Son Nguyen, Canadian Nuclear Safety Commission, Canada

Jonny Rutqvist, Lawrence Berkeley National Laboratory, USA

February 2007



This report concerns a study which has been conducted for the Project DECOVALEX-THMC. The conclusions and viewpoints presented in the report are those of the author/authors and do not necessarily coincide with those of the SKI.

Foreword

The DECOVALEX-THMC project is an ongoing international co-operative project that was started in 2004 to support the development of mathematical models of coupled Thermal (T), Hydrological (H), Mechanical (M) and Chemical (C) processes in geological media for siting potential nuclear fuel waste repositories. The general objective is to characterise and evaluate the coupled THMC processes in the near field and far field of a geological repository and to assess their impact on performance assessment:

- during the three phases of repository development: excavation phase, operation phase and post-closure phase;
- for three different rocks types: crystalline, argillaceous and tuff;
- with specific focus on the issues of: Excavation Damaged Zone (EDZ), permanent property changes of rock masses, and glaciation and permafrost phenomena.

The project involves a large number of research teams supported by radioactive waste management agencies or governmental regulatory bodies in Canada, China, Finland, France, Germany, Japan, Sweden and USA, who conducted advanced studies and numerical modelling of coupled THMC processes under five tasks:

- **Task A:** Influence of near field coupled THM phenomena on performance assessment, initiated by CNSC, Canada.
- **Task B:** The Excavation Disturbed Zone (EDZ). MHC studies of the EDZ, initiated by SKB, Sweden.
- **Task C:** Excavation Damaged Zone (EDZ) in the argillaceous Tournemire site, France, initiated by IRSN, France.
- **Task D:** Permanent permeability/porosity changes due to THM and THM processes, initiated Department of Energy, USA.
- **Task E:** THM Processes Associated with Long-term Climate Change: Glaciations case study, initiated by OPG, Canada.

Work defined in these five tasks are divided into different phases or steps so that the progress can be monitored and achievements documented in project reports.

The present report presents the definition, achievements and outstanding issues of the first phase of Task A, Task A-1, concerning a preliminary THM analysis of a near field model of a repository.

Lanru Jing, Fritz Kautsky, Ove Stephansson and Chin-Fu Tsang

Stockholm, Sweden
February 2007

Summary

This report presents the definition of the first phase, Task A-1, of the Task A of the international DECOVALEX project. The task is a working example of how interaction between THMC modelling and SA analysis could be performed. Starting with the technical definition of the Task A, the report presents the results of preliminary THM calculations with a purpose of an initial appreciation of the phenomena and material properties that must be better understood in subsequent phases. Many simplifications and assumptions were introduced and the results should be considered under these assumptions. Based on the evaluation of the multiple teams' results, a few points of concern were identified that may guide the successive phases of Task A studies:

1. The predicted maximum total stress in the MX-80 bentonite could slightly exceed the 15 MPa design pressure for the container. The MX-80 bentonite exhibits very nonlinear THM behaviour and small variations in the assumed input properties could significantly influence the results. A systematic model calibration with laboratory data will have to be performed in order to predict stresses in the bentonite with more confidence.
2. The preliminary results show that a damage zone could be formed around the waste emplacement boreholes; the extent of this damage zone, as well as its hydraulic and mechanical properties, should be better predicted.
3. In addition to unsaturated properties of both the rock and buffer, the variation of rock permeability with stress or strain could have significant effects on the re-saturation time of the bentonite. Permeability functions specific to the granite under consideration will have to be developed.

Content

Foreword

Summary

	Page
1. Task A-1 definition	1
1.1 Introduction	1
1.2 Description of the repository used in the case study	2
1.3 Anticipated evolution and performance of the repository	7
1.4 Uncertainty	10
1.5 Work statement for Task A-1	10
References	16
Appendix A	16
2. CNSC's preliminary THM modelling of Task A-1	25
2.1 Introduction	25
2.2 General Modelling approach	25
2.3 Mathematical model and governing equations	27
2.4 Equations of nonlinear poro-elasticity for the unsaturated bentonite	29
2.5 T-H-M input properties	31
2.6 Modelling results	34
2.7 Conclusions	36
References	36
3. DECOVALEX-THMC Task A-1 – modelling report by STUK	39
3.1 Introduction	39
3.2 The model	39
3.3 The analyses	43
3.4 Discussion	46
References	47
4. SKI/LBNL's modeling of Task A-1 using ROCMAS	61
4.1 Introduction	61
4.2 Description of the ROCMAS code	61
4.3 FEM mesh and material properties	66
4.4 Modeling sequences and boundary conditions	68
4.5 Analysis of mechanical rock mass failure	68
4.6 Results of coupled THM analysis	69
4.7 Summary and conclusion	71
References	71
5. SKB/Clay team's preliminary THM modelling of Task A-1	85
5.1 Introduction	85
5.2 Finite element code	85
5.3 Element mesh	90
5.4 Material models and properties	92
5.5 Modelling approach and boundary conditions	102
5.6 Primary results	104
5.7 Summary and conclusions	113
References	116

6. Report of Task A-1: preliminary THM analysis of the near field	117
6.1 Introduction	117
6.2. Results of the thermal analysis	118
6.3 Result of preliminary THM analysis	120
6.4 Conclusions	127
References	127
7. Comparison and discussion	157
7.1 Comparison of Task A-1 Results between models	157
7.2 Concluding remarks	161
References	161

1. Task A-1 Definition

T.S. Nguyen, Canadian Nuclear Safety Commission

1.1 Introduction

The rationale and general definition of Task A of DECOVALEX-THMC are given in Nguyen (2003). The objective of Task A is to assess the implications of coupled THM processes in the near field of a typical repository on its long term performance. The proposed work is an actual working example where the engineering experts (in D-THMC) would work in collaboration and interact with performance/safety analysts and experimentalists on a realistic case study of a repository. The proposed work is an example of integration of model development/calibration and interpretation of laboratory and in-situ data towards the final goal of building confidence to the PA process. Task A is divided into the following subtasks:

1. Preliminary THM analysis of the near field: develop a preliminary THM model of the near field of the repository, including one room and one pillar and perform one set of preliminary calculations. The properties of the geological and engineered barriers will be similar to the ones being used by the PA analyst.
2. Model development and calibration: this phase is necessary to fine tune our tools (THM computer codes) and build confidence in these tools. During this phase, exchange of information and feedback between modelers and experimentalists will be promoted.
 - a. Development of THM models of the rock, taking into account damage mechanics. Laboratory experiments and in-situ experiments are available to calibrate the model. Of concern is the strength criteria, and the change in elastic parameters and permeability and the onset of crack propagation. It is proposed that the TSX experiment, at the URL, Whiteshell, Canada will be the in-situ experiment to be considered for model calibration of HM effects with the inclusion of damage mechanics.
 - b. Development of THM model for unsaturated clay barriers. Laboratory tests are available (or will be made available) as well as in-situ experiments. It is proposed that the same TSX experiment be the in-situ experiment to be considered for model calibration.
3. Final THM analysis of the near field
 - a. The safety indicators would be: temperature, damage zone determination, change in permeability, re-saturation of the engineered barriers, swelling stresses, perturbation in the hydraulic head distribution. These indicators will be the output required from the research teams and would be fed back to the PA/SA analyst.
 - b. The analysis would be performed for a period of one thousand years and would include the following phases: excavation and waste emplacement (30 yrs); observation and monitoring period (70 yrs) and post-closure period (200 to 1000 yrs).
4. Communication between the THM modelers, the PA/SA analysts (OPG/AECL),

and the experimentalists (AECL) is promoted during the whole project. In particular, at the end of task A-3, the results of the THM analyses would be communicated to the PA/SA analyst, who would provide feedback on how the PA/SA results could be affected, or if necessary, would perform a revised PA/SA.

The present work package constitutes a detailed task definition for subtask A-1.

1.2 Description of the repository used in the case study

The repository being considered is based on one of the several Canadian case studies. The repository has many common components to Swedish and Finnish concepts: similar corrosion-resistant container; similar horizontal borehole geometry and the bentonite being considered is the Swedish MX-80 bentonite. The detailed description and the anticipated evolution of such a repository are given by McMurry et al. (2003). We provide here a summary of the main features of interest.

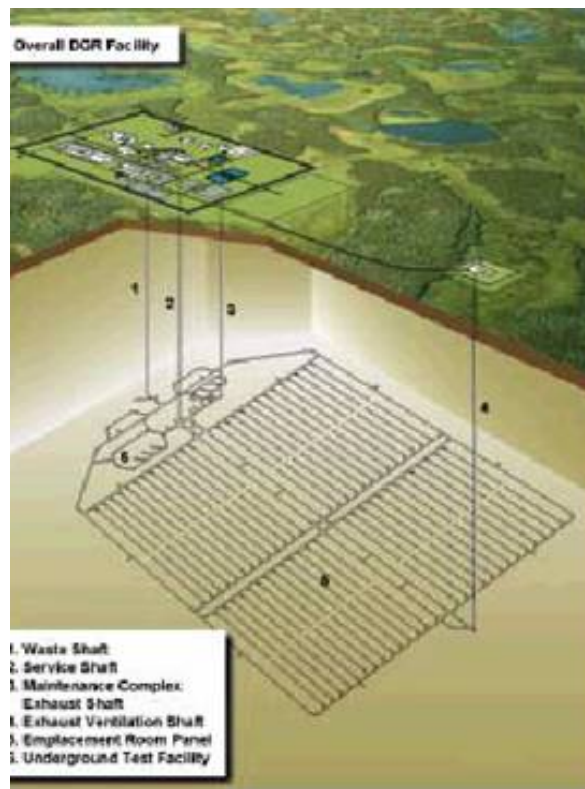


Figure 1.1: Repository layout (McMurry et al. 2003)

The repository being considered would be constructed at a nominal depth of 650 m in a stable crystalline rock of the Canadian Shield (Fig. 1.1) and would consist of a network of horizontal access galleries and emplacement rooms or boreholes. Several room geometries are being considered (Fig. 1.2); however in this project, we will look at the horizontal borehole geometry (Fig. 1.2.c).

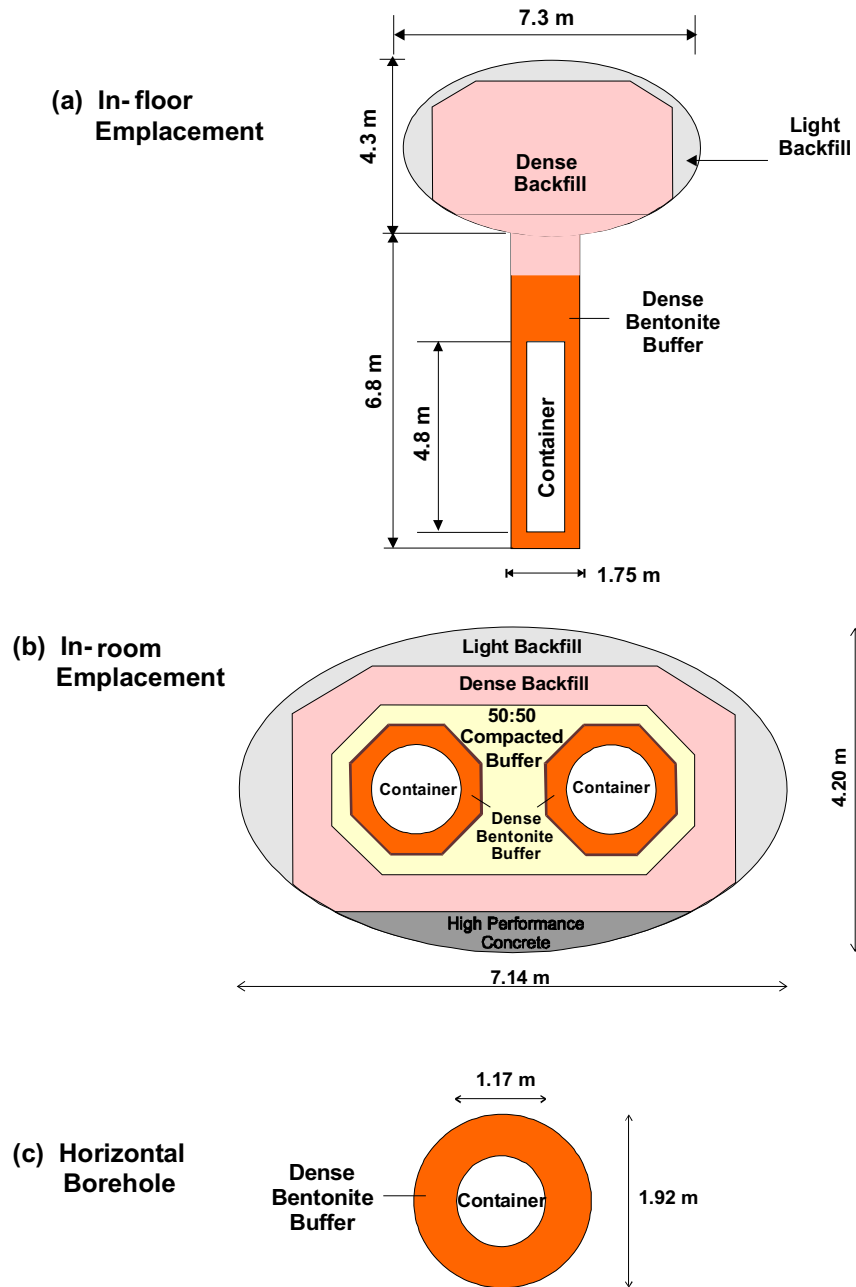


Figure 1.2: Alternative geometrical configurations (McMurry et al, 2003)

The repository relies on a multiple-barrier system in order to ensure the long term safety of humans and the environment. These barriers are:

1. The waste form. CANDU reactors in Canada are fuelled by ceramic pellets of un-enriched Uranium dioxide. These pellets are placed inside Zircaloy-4 fuel sheaths, closed by a welded zirconium alloy plug at the end. Each loaded and closed fuel sheath forms a fuel element. The fuel elements (standard number is 37) are in turn welded together to form a fuel bundle (Fig. 1.3). It is expected that the repository would contain 3.6 millions bundles of used CANDU fuel. At emplacement, the used fuel bundles would have a minimum age of 30 years after the reactor discharge.

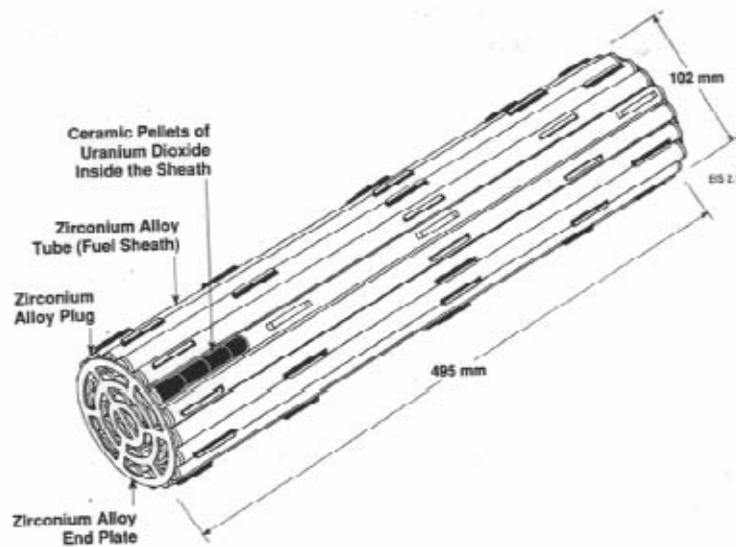


Figure 1.3: Candu fuel bundle (McMurry et al, 2003)

2. The container (Fig. 1.4). The container being considered is similar to the Swedish and Finnish containers. It would encapsulate 324 fuel bundles in 6 layers, and have a total mass of 23.5 Mg. A 25 – 30 mm thick outer copper shell will provide a corrosion barrier. The copper shell is not designed to withstand stresses. The structural resistance is provided by an 80-100 mm thick inner steel shell, designed to withstand a pressure of 15 MPa (from hydrostatic pressure and swelling pressure from the buffer), plus an additional 30 MPa from future glaciations. The maximum design temperature for the exterior surface of the container is 100 °C, in order to minimize thermal effects on the repository seals, such as the bentonite buffer.
3. The buffer. The buffer is a bentonite-based clay material. The main mineral responsible for swelling property of the buffer is montmorillonite. Under saturation, the bentonite expands several times if unrestrained; under confinement, a swelling pressure would develop. The main functions of the buffer are:
 - To limit the corrosion rate of the container by inhibiting the movement and modifying the chemistry of the groundwater
 - To conduct heat away from the container
 - To keep the container in place
 - To provide a mechanical buffer between the container and the rock
 - To reduce the potential for microbial activity.
4. The geosphere. The geosphere is a plutonic rock mass of the Canadian Shield (Fig. 1.5). The Canadian Shield is formed by large bodies of igneous rock called plutons which crystallized more than 2 billion years ago from magma. The topography of the Shield is flat, with the highest elevation at about 500 masl (Fig. 1.6). Therefore, the hydraulic gradients are low across the Shield (of the order of 0.1%). The main functions of the geosphere are to:
 - Protect the repository from natural events (such as earthquakes and glaciations) and human intrusion
 - Limit the rate of contaminant transport to the biosphere

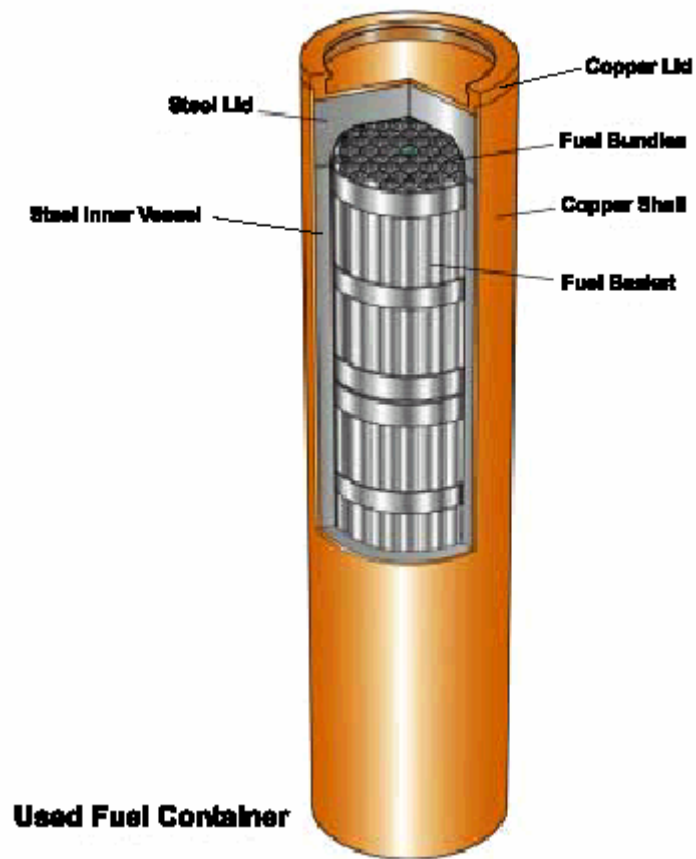


Figure 1.4: Used fuel container (Russell and Simmons 2003 cited in McMurry et al. 2003)

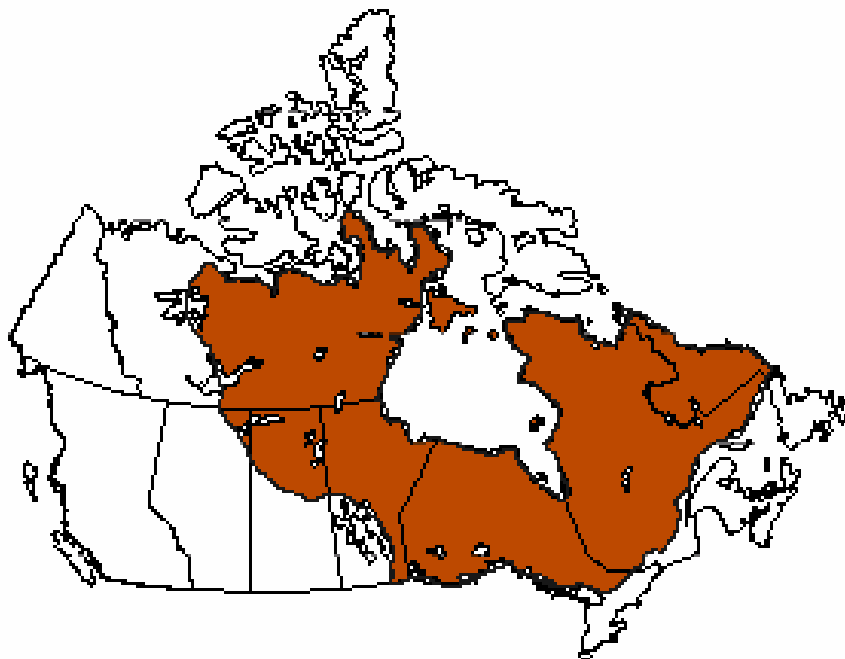


Figure 1.5: The Canadian Shield (McMurry et al. 2003)

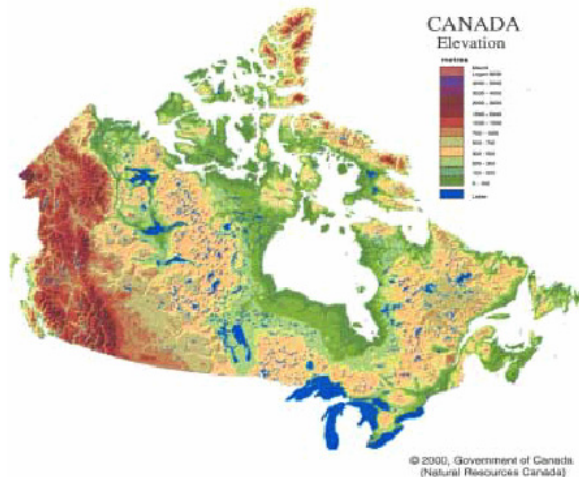


Figure 1.6: Topography of Canada

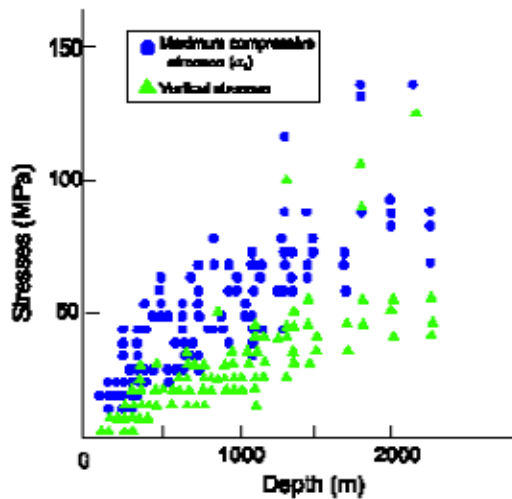


Figure 1.7: In-situ stress in Canadian Shield (Herget and Arjang, 1990 cited in McMurry et al.)

In-situ stress at different locations of the Shield has been compiled by Herget and Arjang (1990) and is shown in Fig. 1.7. In general, the minor principal stress is vertical and results from the weight of the overburden, while the major principal stress is sub-horizontal and oriented NE to E. The degree of fracturing in a typical plutonic rock mass of the Canadian Shield generally decreases with depth. Qualitatively, depending on the degree of fracturing, the rock mass could be classified as: fracture zone (FZ), highly fractured rock (HFR), moderately fractured rock (MFR), sparsely fractured rock (SFR) and intact rock (IR) (Fig. 1.8). Quantitatively, the degree of fracturing translates into the following equivalent permeability range: 10^{-15} - 10^{-12} m^2 (FZ), 10^{-12} - 10^{-15} (HFR), 10^{-15} - 10^{-18} m^2 (MFR), 10^{-18} - 10^{-21} (SFR) and $<10^{-21}$ m^2 (IR). The permeability distribution at a typical site is shown in Fig. 1.9, while a compilation of permeability variation with depth is given in Fig. 1.10. It could be seen that outside of the FZ, HFR are found at the top 200-300 m, followed by MFR down to 500 m, followed by SFR. At depths greater than 1000m, the rock is essentially intact. That type of rock distribution has a profound influence on the nature and chemical-physical properties of the groundwater. At depth less than 300 m, one finds a shallow, advective groundwater zones with low salinity, showing significant interaction with infiltrating water from the surface. At greater depths, the water is brackish to saline. This is a stagnant zone of groundwater, whose age are in the order of millions years. The salinity of the deep water results in a higher density, up to 1.1 as compared to fresh water.

1.3 Anticipated evolution and performance of the repository

In a base scenario (McMurry et al., 2003), which is judged to be the most likely situation, there is no release of contaminant from the repository for at least 10,000 years and most probably for 100,000 years. However, the excavation and operation of the repository, and its thermal output will perturb the existing conditions in the engineered barriers and in the geosphere. The anticipated evolution for the next 10,000 years of the engineered and natural (geosphere) barriers is determined based on modeling of similar repository, study of natural analogues and expert judgment. This evolution is summarized as follows:

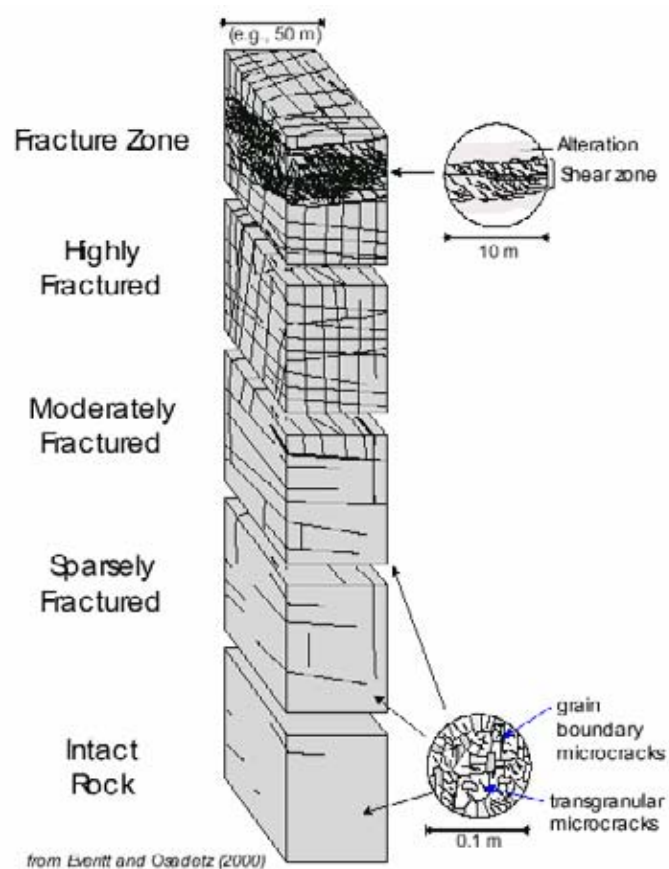


Figure 1.8: Illustration of crystalline rock fracturing (Everitt and Osadetz cited in McMurry et al. 2003)

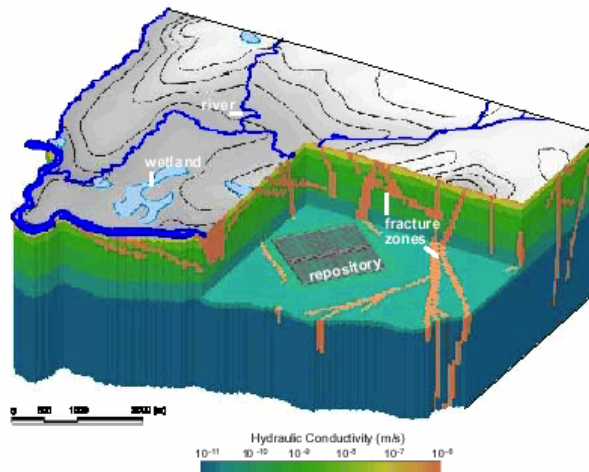


Figure 1.9: Typical permeability distribution (McMurry et al. 2003)

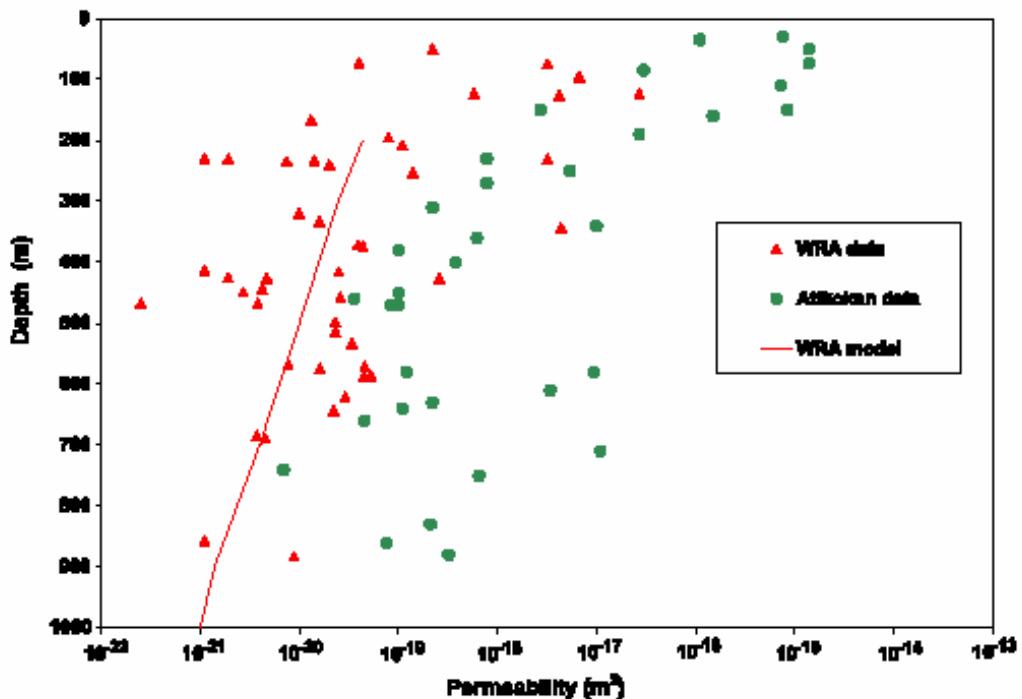


Figure 1.10: Permeability distribution (Stevenson et al. ,1996 and Ophori and Chan 1996, cited in McMurry et al. 2003)

a) 0-100 years: During this time period, the repository would be open and actively monitored. Approximately 11,000 containers of used fuel would be emplaced and filled up rooms would be progressively sealed during a 30 years operational period, covering an area of 2 km². The operational period would be followed by 70 years of monitoring when the access tunnels would be kept open. The initial thermal output from the repository is 13 MW, and the initial radioactivity is 10²⁰ Bq. During this time period, it is expected that:

- The thermal output would decrease by a factor of four and radioactivity drops by a factor of ten, at 100 years.
- The peak temperature on the outer surface of the containers is less than 100 °C.

- The bentonite near the container dries out and desiccates. Bacterial activity is non-existent to minimal due to heat, desiccation, lack of water and nutrient.
- The copper container surface reacts with oxygen to form a thin corrosion layer. Localized corrosion processes are not possible due to lack of water and microbes.
- At 100 years, the thermal plume would extend approximately 100 m around the repository
- Microcracking occurs in the rock around the opening due to excavation and possibly thermal stresses. This results in a change in the permeability and mechanical properties of the rock.
- The rock has to supply water to the unsaturated bentonite, resulting in an inward gradient. This is countered by the thermally generated pore pressure increase that creates an outward gradient.

b) 100-1000 years: At the beginning of this period, all access shafts and tunnels would be closed. There would be high physical, chemical and biological gradients between the different components of the repository, and between the repository and the geosphere. These gradients are the driving forces for the evolution of the repository/geosphere system. It is expected that during that period:

- The radioactivity drops by a further factor of 30; the thermal output drops to 1.3 MW
- The bentonite and seals are expected to be fully saturated by the end of this period. As water enters the bentonite, swelling pressures start to develop and would be transmitted to the container. After full resaturation, the full hydrostatic pressure would also be transmitted to the container. Under these loads, the copper shell would compress into the steel shell, which is expected to retain its shape. With the presence of water, pit corrosion would start at specific locations of the container surface, however the penetration depths are expected to be less than several mm.
- At 1000 years, the thermal plume would extend a few hundreds meters around the repository.

c) 1,000 – 10,000 years: In this time period, the repository and its components and the geosphere gradually reach an equilibrium state. It is expected that:

- Radioactivity drops by a further factor of two. Thermal output from the repository drops to approximately 4.4 MW. The thermal plume reaches its largest extent hundreds to thousands of metres in all direction, however the temperature has dropped to maximum values between 30-60°C.
- Since all oxygen has been consumed by microbes, corrosion of the container due to pitting and uniform corrosion has stopped.
- The porewater in the sealing material (and in the buffer) becomes more saline due to the ingress of groundwater that mixes with the starting porewater.
- The fuel remains intact. The buildup of He from alpha decay produces an increase internal pressure; however this pressure is well within the structural resistance of the cladding.

1.4 Uncertainty

Each element of the above base case scenario is subject to a relative degree of confidence, depending on the current state of knowledge. We review here the elements with the higher degree of uncertainty as listed by McMurry et al. (2003), which are of relevance to THM processes. In Task A of DECOVALEX-THMC, we hope to provide a higher degree of confidence in these elements by scoping calculations and model calibration. These elements are:

1. The temperature field has been calculated with pure thermal models. There is a need to confirm the thermal results with coupled THM models.
2. The anticipated loads on the container due to buffer swelling are expected to be non-uniform, but there is only limited analysis on both the nature of these non-uniform loads and their effect on the container's longevity.
3. The nature and extent of shrinkage and cracking of the buffer near the container is not yet well characterized.
4. Swelling characteristics of a wide range of bentonite-based buffer have been relatively well studied in the laboratory, but need to be confirmed for site-specific conditions.
5. The saturation rate of the repository has to be confirmed for site specific conditions. For example in BMT1 of DECOVALEX III, it is shown that the resaturation rate is largely dependent on the permeability or the degree of fracturing of the rock mass. The resaturation of a repository involves complex THM coupling, and should be analysed with coupled THM models. The time for full resaturation of a repository varies between 10 to 1000 years depending on the rock. From a safety point of view, without full resaturation, minimal corrosion of the container, and minimal microbial activity in its vicinity are expected .
6. The container weighs 25 Mg and its effect on the plastic deformation of the saturated bentonite has not been examined in detail.
7. The interfaces between the components of the system could be preferential pathways for groundwater, contaminants or microbes. There is a need to develop coupled THM models for these interfaces and demonstration tests to calibrate these models.
8. Fracture development and propagation in the geosphere around the repository have to be better understood and quantified.
9. The effects of THM coupling on the groundwater flow field in the geosphere has to be better understood and quantified, in particular in anisotropic and fractured crystalline rock. The effect of salinity on groundwater flow has to be included.

1.5 Work statement for Task A-1

In Task A-1, we will strive to address as much as possible the uncertainties listed above. The detailed technical specifications of the repository layout, including the geometry, the heat output, and the basic properties of the engineered and geological barriers are given in Appendix A, provided by OPG. Based on these specifications, and using repetitive symmetry, we will perform THM calculations for one web of a borehole/pillar as shown in Figure 1.11. The work is defined as follows:

1. Perform simple T calculations to determine the combination of borehole-to-borehole and container to container centerline distances that would result in an outside temperature of 100 °C for the container. The borehole-to-borehole centerline distance varies in a range of 25 to 70 m, and the centerline spacing between containers in a range of 5.6 to 8 m. Assume that the bentonite remains at the emplaced water content of 16%, corresponding to a 60% degree of saturation.
2. From 1 above, adopt a combination of pillar width and container distance that minimizes the repository area. Perform first a steady state HM analysis to establish pre-excavation conditions using the boundary conditions shown in Fig. 1.12. The values of the in-situ stress are given in Appendix A. Perform a transient HM analysis for 30 years to simulate the operational phase of the repository. Assume the borehole is open and maintained at atmospheric pressure during that phase.
3. At time 30 years, assume all boreholes are instantaneously filled with container and bentonite. The container heat output is shown in Figure 1.13. Perform THM analysis up to 1000 years.
4. The required output will be detailed next, as listed in Table 1.1. In light of the results obtained, the research teams should assess how much of the uncertainties listed in the previous section they have resolved.

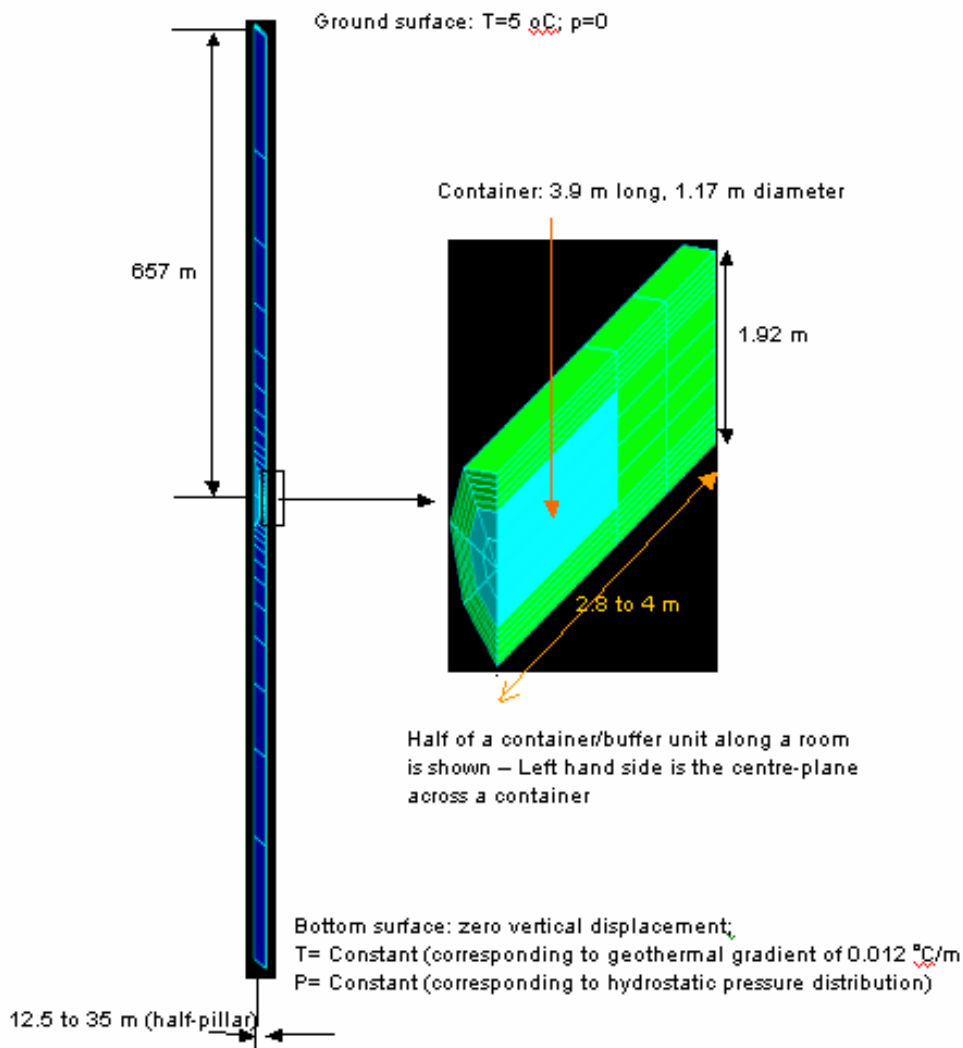


Figure 1.11: Geometry and Boundary Conditions for a room/pillar half unit

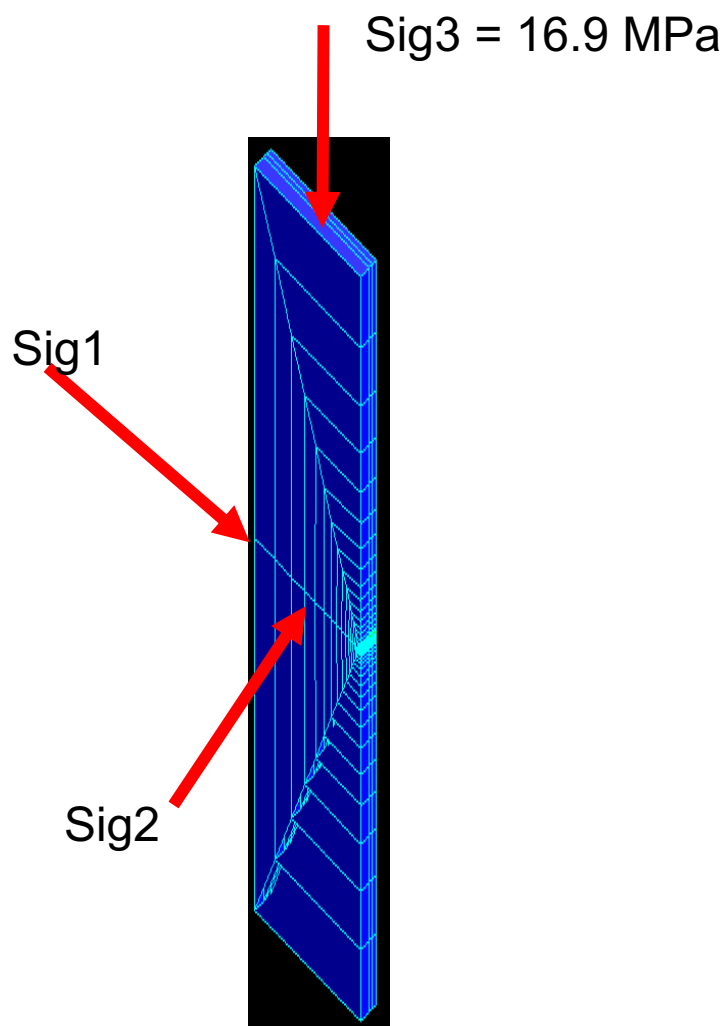


Figure 1.12: In-Situ Stresses at repository depth of 657 m

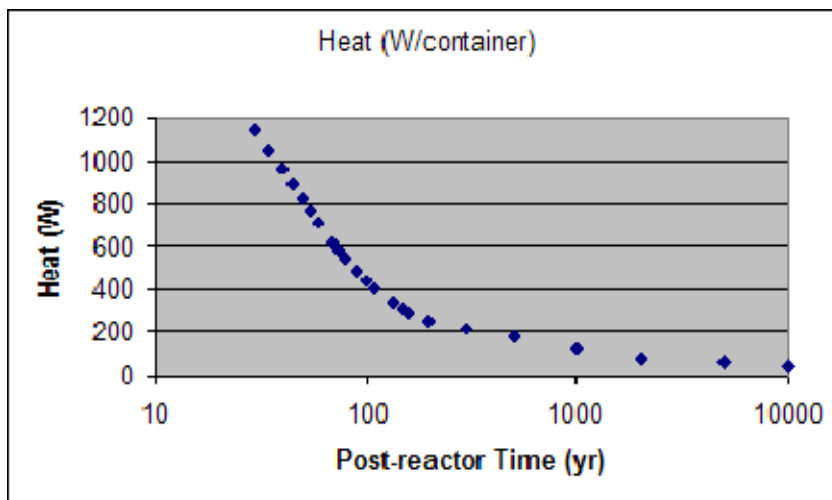


Figure 1.13: Power output from container

1.5.1 Output specifications

For the rock mass, contour plots of temperature, pore pressure, factor of safety for rock mass failure and permeability are required at times: 30 years, 100 years, 1000 years, at the times corresponding to the maximum temperature and full resaturation at point B1. Output specification in bentonite is listed in Table 1.1.

Table 1.1 Points in bentonite where time history curves are required (T= temperature, θ = volumetric water content; σ = total stress)

Point	x (m)	y (m)	z (m)	Output values
B1	0.585	0	0	T, θ , σ_{xx}
B2	0	0.585	0	T, θ , σ_{yy}
B3	0	-0.585	0	T, θ , σ_{yy}
B4	0.96	0	0	T, θ , σ_{xx}
B5	0.7725	0	0	T, θ , σ_{xx}
B6	0	0	2.45	T, θ , σ_{zz}
B7	0	0	-3.43	T, θ , σ_{zz}
B8	0.585	0	2.45	T, θ , σ_{xx}
B9	0	0.585	2.45	T, θ , σ_{yy}
B10	0	-0.585	2.45	T, θ , σ_{yy}

1.5.2 Basic material properties

Rock mass basic properties

The following basic properties of the rock mass at a depth of 657 m are assumed:

Density: 2650 kg/m³

Young's modulus: 60 GPa

Poisson's ratio: 0.202

Biot's coefficient: 0.36

Coefficient of linear thermal expansion: $10 \times 10^{-6} \text{ } ^\circ\text{C}^{-1}$

Thermal conductivity: 3 W/m²°C

The permeability varies with depth as in Table A.5 of Appendix A.

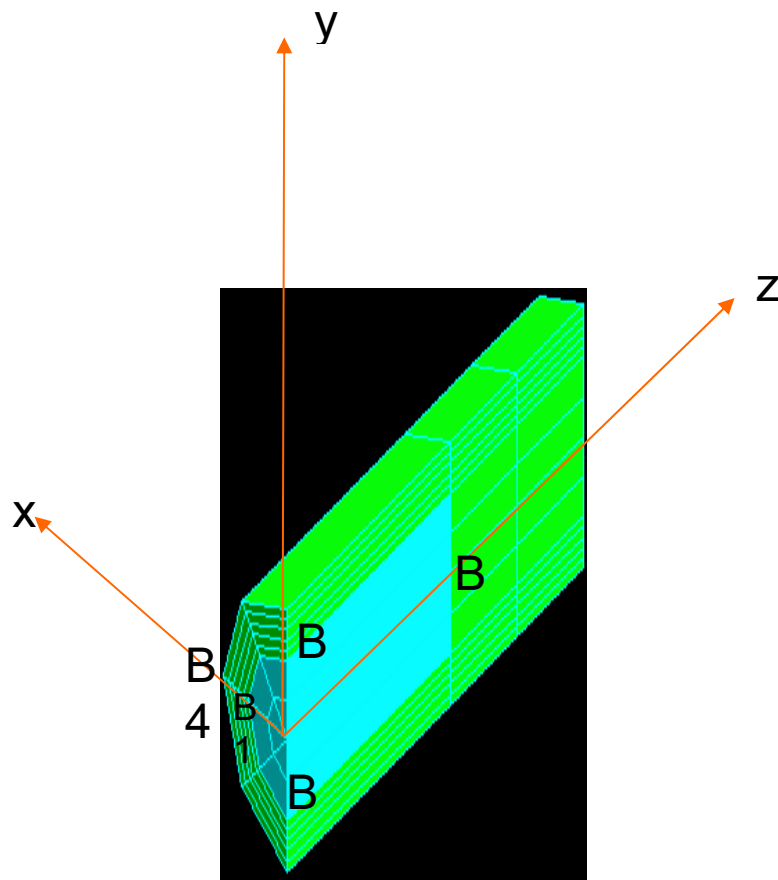


Figure 1.14: Typical output points in the buffer

Rock mass permeability function

The rock mass permeability is assumed to be a function of the effective porosity. This function is derived from experimental data on sparsely fractured rock, with a permeability range of 10^{-19} to 10^{-17} m². The permeability function is shown in Fig.1.15.

Rock mass failure criterion

We will adopt Hoek and Brown's failure criterion, expressed in term of effective stress:

$$\sigma'_{1f} = \sigma'_3 + \sqrt{m\sigma_c\sigma'_3 + s\sigma_c^2} \quad (1.1)$$

with:

σ'_{1f} = major effective principal stress at failure

σ'_3 = minor effective principal stress

σ_c is the uniaxial compressive strength m, and s are empirical constants.

References

- Borgesson, L. and Hernelind, J., *Coupled thermo_hydro-mechanical calculations of the water saturation phase of a KBS-3 deposition hole - influence of hydraulic rock properties on the water saturation phase*. SKB report TR-99-41, SKB, 102 40 Stockholm, Box 5864. 1999.
- Herget, G. and Arjang, B., *Update on ground stresses in the Canadian Shield, Proc. Specialty Conf. Stresses in Underground Structures, Ottawa, Canada*. CANMET, Canadian Government Publishing Centre Supply and Services, Ottawa, Canada. 1990.
- McMurry, J., D.A. Dixon, J.D. Garroni, B.M. Ikeda, S. Stroes-Gascoyne, P. Baumgartner and Melnyk, T.W., *Evolution of a Canadian deep geologic repository: base scenario*. OPG report 06819-REP-01200-10092-R00, OPG, NWMD, 700 University Avenues, Toronto, Ont. Canada M5G 1X6. 2003.
- Nguyen, T.S., *Influence of near field coupled thm phenomena on performance assessment, Canadian Nuclear Safety Commission, Version 2*. October 2003.
- Pusch R., *The buffer and backfill handbook, part 2: materials and techniques*, SKB report TR-02-12, SKB, 102 40 Stockholm, Box 5864. 2001.

Appendix A: Technical specification from OPG

(Recommended for Horizontal Borehole Concept for DECOVALEX-THMC model, Revision 0a, 15 April 2004)

A.1 Introduction

This Technical Specification defines parameters for a proposed deep geologic repository (DGR) design based on horizontal borehole emplacement of used nuclear fuel. These parameters are based on preliminary analyses, and may be used as input data into more detailed thermal, hydraulic and mechanical calculations within the DECOVALEX-THMC Task A.

A.2 Technical requirements

The technical specifications for the DGR horizontal borehole emplacement method are listed in Table A.1. These specifications are based on a CANDU used fuel container emplaced in boreholes in Canadian Shield rock. They are similar to the SKB and Posiva KBS-3H concept (Hokmark and Falth, 2003), but not identical. For example, the container dimensions are slightly different, the thermal power is lower (1140 W vs approx. 1700 W), and there is a larger gap between container assembly and borehole for emplacement tolerance (50 mm rather than 42 mm).

Additional details regarding parameter values are provided in Tables A.2 to A.5, and Figure A.1. Further discussion on the choice of parameter value is given in Section 3 of this document.

The in-situ rock stresses to be used for the mechanical analysis are (Baumgartner et

al. 1995, App.B):

$$\begin{aligned}
 \sigma_1 &= 0.1345MPa / m_{depth} + 18.5MPa && < 300m \\
 \sigma_1 &= 0.00866MPa / m_{depth} + 56.3MPa && \text{from 300 to 1400m} \\
 \sigma_1 &= 0.0403MPa / m_{depth} + 12.1MPa && > 1400m \\
 \sigma_2 &= 0.1112MPa / m_{depth} + 9.9MPa && < 300m \\
 \sigma_2 &= 0.00866MPa / m_{depth} + 40.7MPa && \text{from 300 to 1660m} \\
 \sigma_2 &= 0.0293MPa / m_{depth} + 6.4MPa && > 1660m \\
 \sigma_3 &= \sigma_v = 0.0260MPa / m_{depth}
 \end{aligned}$$

where σ_v = vertical stress; and $\sigma_1, \sigma_2, \sigma_3$ are the major, intermediate and minor principal stresses respectively.

For design purposes, it is conservatively assumed that the repository boreholes are oriented with their longitudinal axis perpendicular to the highest principal stress. For comparison purposes, an assessment should also be carried out at the time of highest stress for the condition when the boreholes are oriented in the more favourable direction, with the maximum principal stress aligned with the boreholes longitudinal axis.

A two-stage failure criterion is recommended for assessment of the rock formation, specifically the Hoek and Brown empirical criterion, where:

$$\sigma_{1f} = \sigma_{3f} + \left(m \cdot \sigma_c \cdot \sigma_{3f} + s \cdot \sigma_c^2 \right)^{1/2} \quad (\text{A.1})$$

Two peak compressive strength design limits shall be used in the structural analyses (Baumgartner et al. 1996). The recommended failure parameters for the excavated borehole are: $\sigma_c = 100MPa$, $m = 16.6$ and $s = 1$ and the failure parameters for the post-emplacement borehole are: $\sigma_c = 150MPa$, $m = 25$ and $s = 1$.

A.3 Discussion

This Technical Specification defines the preliminary repository layout parameters that should be used for the thermo-mechanical evaluation of the proposed DGR design. These parameters have been selected to offer a design that is expected to comply with the design requirements, principally that the UFC surface temperature will remain below 100°C, and that the excavations will remain stable during the preclosure period (including the excavation, operation and extended monitoring periods) and the postclosure period of the repository (including a glaciation cycle). However, the dimensions have not been verified by detailed calculations yet so remain to be finalized, in particular the container spacing and borehole spacing.

The rationale for selecting certain parameter values is provided in the remainder of this section.

Table A.1: Technical Specifications for Horizontal Borehole Container Emplacement

Design Feature	Design Specification	Discussion
Used Fuel Container (UFC):		
UFC length (mm)	3867	
UFC outer diameter (mm)	1168	
UFC Buffer Jacket Assembly:		
Outer diameter (mm)	1818	
Outer steel shell thickness (mm)	25	
Overall length (mm)	4517	
Assembly/rock gap (mm)	50	
Buffer Rings:		
Initial inner diameter (mm)	1168	UFC OD
Initial outer diameter (mm)	1768	UFC OD + (2 x 300 mm)
Buffer End Plugs:		
Outer diameter (mm)	1818	
Length (mm)	300	
Distance Blocks:		
Outside diameter (mm)	1818	
Outer shell thickness (mm)	13	
Length (mm)	1083	Based on 5.6 m UFC spacing
Emplacement Borehole:		
Borehole diameter (mm)	1918	
UFC orientation (Single row along borehole centre)		Same as KBS-3H
UFC spacing, centre-to-centre (m)	5.6	Nominal value. Range under consideration is 5.6 - 8 m.
Number of UFCs / borehole	52	
Distance from borehole end (rock) to first UFC assembly (m)	1.083	One distance block
Distance from bulkhead to last UFC assembly (m)	1.083	One distance block
Concrete bulkhead length (m)	6	Included in borehole length (nominally 3 x borehole diameter)
Borehole length (m)	300	Depends on UFC spacing. Nominal value based on 52 x 5.6 m + 2 distance blocks + bulkhead. 300 m maximum as specified for KBS-3H
Turning access length (m)	25	
Total room length (m)	325	Borehole + access length
Repository Layout:		
Minimum container capacity	11,111	
Number of repository sections	4	
Number of boreholes / section	54	54 boreholes/section x 52 containers/borehole x 4 sections = 11232 containers
Borehole spacing (centre-to-centre) (m)	50	Range from 25 to 70 m under evaluation
Repository width (m)	1400	4 x room length + access tunnels (approx.)
Repository length (m)	2800	54 x room spacing + access tunnels (approx.)
Repository area (km ²)	3.9	(approx.)

Table A.2:UFC Heat Output as a Function of Time

Post-reactor Discharge Time (years)	Heat Generation (W/container)
30	1139
35	1045
40	962
45	887
50	821
55	762
60	709
70	618
75	580
80	546
90	488
100	441
110	403
135	337
150	311
160	297
200	261
300	222
500	182
1,000	126
2,000	85.9
5,000	62.4
10,000	44.9
20,000	26.0
35,000	14.1
50,000	8.89
100,000	2.75
200,000	1.03
250,000	0.95
500,000	0.92
1,000,000	0.92
10,000,000	0.62

Table A.3: UFC and Granite Material Properties

Property	Inner Shell	Outer Shell	Granite
Material	SA 516-70 for shell, SA 105 for ends	OFP Copper	Granite
Thermal conductivity (W/m°C)	59	380	3.0
Specific heat (kJ/kg°C)	0.460	0.390	0.845
Density (kg/m ³)	7800	8930	2650
Porosity (%)	0	0	0.3
Young's modulus (GPa)	200	117	60
Poisson's ratio	0.30	0.3	0.25
Yield stress (MPa)	260	N/A	N/A
Ultimate tensile strength (MPa)	485	N/A	N/A
Thermal expansion coefficient (10 ⁻⁶ /°C)	12	16	10
Strain to Failure	N/A	29%	N/A

Table A.4: Sealing Material Thermo-Mechanical Properties *

Property	Buffer	Gapfill ⁺
Composition	Bentonite blocks	Bentonite pellets
Density (kg/m ³)	1600 dry 1850 as-placed	1400 dry 1400 as-placed
Porosity (%)	41	49
As-placed saturation (%)	60	5
Gravimetric moisture content (%)	16 as-placed 26 saturated	2 as-placed 36 saturated
EMDD (kg/m ³)	1400	1180
Thermal conductivity (W/m°C)	0.4 dry 1.25 saturated	0.4 dry 1.25 saturated
Specific heat (kJ/kg°C)	0.8 dry	0.8 dry

* "dry" means with 4% residual water saturation level "as-placed" means with as-placed water Saturation level.

+ Gapfill properties are averaged over the gap space. Pellets will be higher density. Properties will change with saturation, and as the interior buffer blocks swell and expand into the more porous gapfill.

Table A. 5: Geosphere permeability profile

Layer	Depth (m)	Thickness (m)	Layer Permeability (m²)	Zone Type
1a	0 - 10	0-10	1×10^{-12}	Sediment
1b	0 - 10	0-10	1.3×10^{-15}	Overburden
1c	0 - 10	0-10	7×10^{-14}	Shallow rock
2	10 - 30	20	7×10^{-15}	Shallow rock
3	30 - 70	40	7×10^{-15}	Shallow rock
4	70 - 150	80	8×10^{-17}	Shallow rock
5	150 - 300	150	7×10^{-18}	Middle rock
6	300 - 500	200	3×10^{-18}	Deep rock
7	500 - 700	200	7×10^{-19}	Deep rock
8	700 - 900	200	1×10^{-19}	Deep rock
9	900 - 1100	200	1×10^{-19}	Deep rock
10	1100 - 1500	200	1×10^{-19}	Deep rock

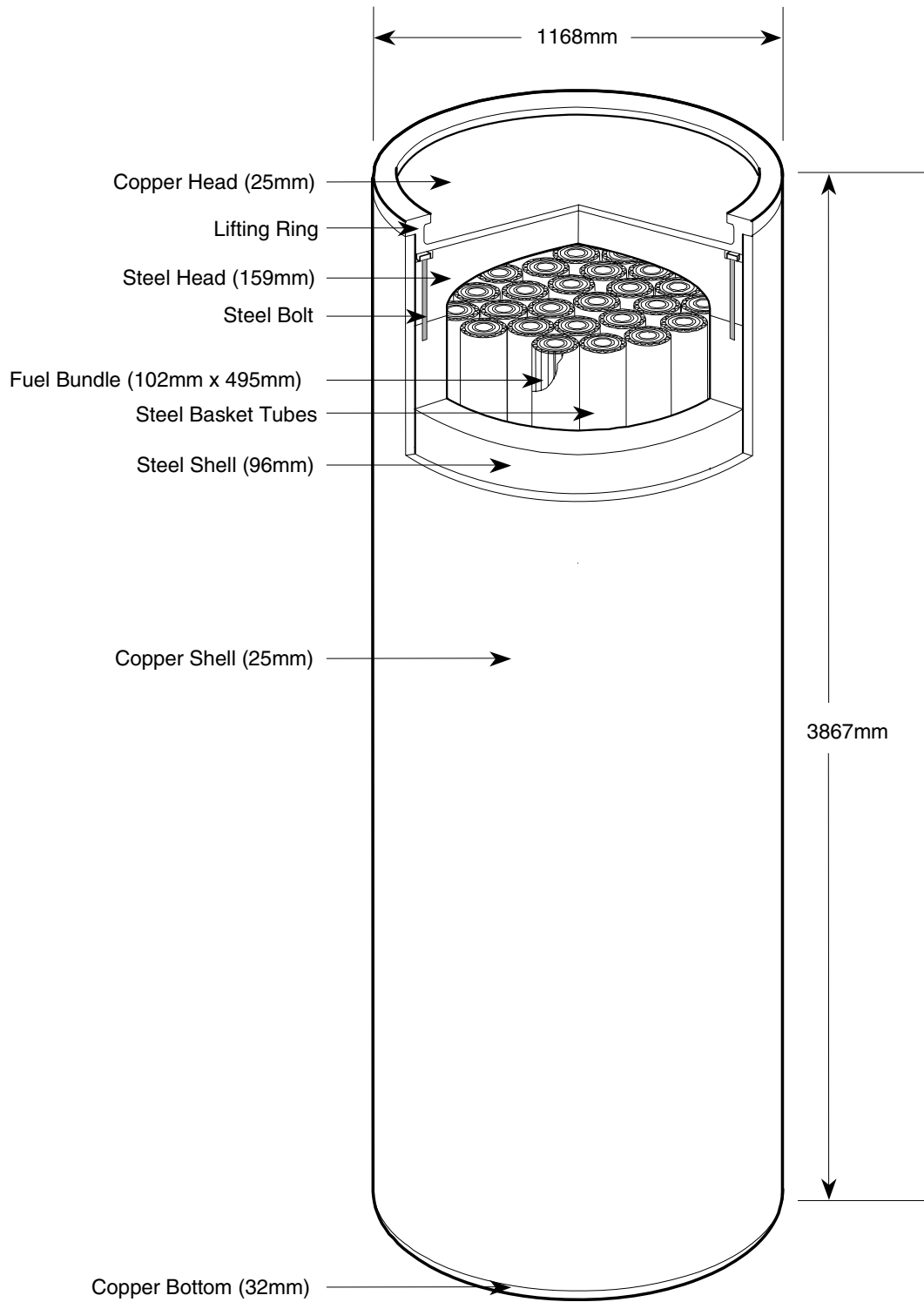


Figure A. 1: Container design showing copper outer shell, inner steel vessel, and fuel assemblies inside support tubes.

A3.1 Used Fuel Container

The used fuel container (UFC) container is the IV-324-hex configuration (Russell and Simmons, 2003), which is designed to hold 324 CANDU used fuel bundles. Figure A.1 shows the container and dimensions.

A3.2 Used Fuel Container Assembly

The horizontal borehole concept consists of the emplacement of a series of UFCs within horizontally bored rooms up to 300 m in length. Each UFC is surrounded with highly compacted bentonite blocks, held in contact against the UFC by a cylindrical perforated steel shell. The entire assembly is then inserted into the horizontal borehole and moved along to its final position as one package.

In the horizontal borehole emplacement design considered here, the annular thickness of the bentonite blocks is 300 mm. There is no air gap between the UFC and the bentonite blocks, nor between the steel shell and the bentonite. The steel shell is 25 mm thick, including the ends. This gives an outer diameter for the UFC assembly of 1818 mm (1168 mm UFC diameter, plus 2 x 300 mm bentonite, plus 2 x 25 mm steel shell) and an overall length of 4,517 mm (3867 mm container, plus 2 x 300 mm bentonite, plus 2 x 25 mm end plates).

A 50-mm annular gap has been provided between the UFC buffer jacket assembly and the borehole perimeter. This gap is slightly larger than the KBS-3H design, to allow more assembly tolerance. In this design, with 300-mm bentonite buffer thickness and 50-mm gap, it is recommended that the gap space be filled with gapfill pellets as specified in Table 4. After saturation and equilibration, the averaged buffer properties across the borehole volume (ring buffer and gapfill) are estimated as 2000 kg/m³ density (EMDD = 1370 kg/m³). This is expected to be sufficient to ensure little microbial activity at the container surface, low permeability, and a swelling pressure of at least 1 MPa at groundwater salinities up to 100 g/L (McMurry et al. 2003; Dixon et al. 2002).

The assembly should be assumed to be positioned centrally in the borehole (Hokmark and Falth, 2003), so the annular gap will be uniform.

The perforated steel shell is penetrated by uniformly spaced holes occupying 50% of the surface area.

Between each emplaced UFC, a monolithic sealing “distance” block is installed to space the heat-generating UFC assemblies along the borehole so as to meet thermal criteria, offer radiation shielding and provide a seal. The distance block is assembled in a similar manner as the UFC buffer jacket assemblies, with a cylindrical perforated steel shell to maintain block integrity during handling. Due to the low mass of the distance-block assembly compared to the UFC buffer jacket assembly, the thickness of the cylindrical perforated steel shell is reduced to 13 mm. The nominal length of the distance block will be 1083 mm to give a UFC spacing of 5.6 m centre to centre, although this length may change depending on the final selected UFC spacing.

A3.3 Emplacement Borehole

Previous design work for the Canadian Shield setting considered an elliptical cross section excavation for the UFC emplacement room. The ellipse shape was selected to

optimise the stresses at the room periphery based on a best estimate of the anticipated in-situ rock stress. In view of the variation in stress orientation likely to be encountered in practice within a fractured rock mass, the thermo-mechanical stress analysis carried out at that time considered stresses both in the optimal orientation and in the unfavourable 90° offset condition. Both orientations resulted in the prediction of local cracking and possible spalling of rock from the excavation surface as the repository reached peak rock temperature. In both cases the damage zone was restricted to the surface 200-300 mm of rock, and in neither case was gross failure of the chamber predicted. Given these results and the comparative simplicity of excavating a circular borehole, the present specifications are based on circular emplacement boreholes.

The borehole diameter is 1918 mm, based on 1818 mm UFC assembly diameter plus 2 x 50 mm air gap.

A3.4 Repository Layout

SKB is evaluating a repository layout based on a borehole spacing of 40 m and a UFC spacing of 7.4 to 8.0 m, for broadly similar UFC and borehole dimensions, but 50% more heat output (Hokmark and Falth, 2003).

Two layouts have been considered during preliminary analyses for the present repository - a borehole spacing of 25 m together with a UFC spacing of 5.6 m, and a borehole spacing of 70 m with the same UFC spacing of 5.6 m. It is presently considered likely that the 25 m borehole spacing does not meet rock stress requirements, while the 70 m borehole spacing is likely larger than required.

Since the DECOVALEX THMC models should provide a more accurate evaluation of temperatures and stresses, it is recommended that DECOVALEX modellers start with an assumed 50 m borehole spacing and 5.6 m container spacing, and then revise these as needed in order to obtain an acceptable design point, with varying the borehole spacing preferred for cost reasons.

A3.5 Site

The reference design concept is a single-level repository located at about 670 m depth. After each borehole is filled, it is sealed from the access tunnel by a concrete bulkhead. It is estimated that the emplacement of the containers will take about 30 years. It is assumed that the repository will be actively monitored for another 70 years, and then all remaining access shafts and tunnels would be filled with backfill, sealed, and the repository fully closed.

Within the bulk rock around the repository, the permeability of the rock can be approximated as isotropic and horizontally uniform, with the permeability profile variation with depth as considered in a recent OPG Third Case Study for a hypothetical Canadian Shield setting, see Table 5. The groundwater at the repository horizon is reducing with a Total Dissolved Solid content of 25 kg/m³ (principally CaCl₂ and NaCl).

The geothermal gradient at the site is 0.012 °C/m. The average surface temperature is 5°C.

REFERENCES

- Baumgartner, P., Bilinsky, D. M., Onofrei, C., Ates, Y., Bilsky, F., Crosthwaite, J. L. and Kuzyk, G. W., *The In-room Emplacement Method for a Used Fuel Disposal Facility – Preliminary Design Considerations*. AECL Technical Record, TR-655, COG-94-533. 1995.
- Baumgartner, P., Bilinsky, D. M., Ates, Y., Read, R. S., Crosthwaite, J. L. and Dixon, D. A. *Engineering for a disposal facility using the in-room emplacement method*. Atomic Energy of Canada Limited Report, AECL-11595, COG-96-223. 1996.
- Dixon, D.A., Chandler, N. and Baumgartner, P., *The influence of groundwater salinity and interfaces on the performance of potential backfilling materials*. 6th Inter. Workshop on Design and Construction of Final Repositories. Brussels, Belgium. 2002.
- Hokmark, H. and Falth, B. *Thermal dimensioning of the deep repository*. SKB Technical Report TR-03-09. Stockholm, Sweden. 2003.
- McMurry, J., Dixon, D., Garroni, J., Ikeda, B., Stroes-Gascoyne, S., Baumgartner, P. and Melnyk, T., *Evolution of a Canadian deep geologic repository: Base scenario*. Ontario Power Generation, Nuclear Waste Management Division Report 06819-REP-01200-10127-R00. Toronto, Canada. 2003.
- Russell, S.B. and G.R. Simmons. *Engineered barrier system for a deep geological repository in Canada*. Proc. 2003 Inter. High Level Radioactive Waste Management Conf., Las Vegas, USA. 2003.

2. CNSC's preliminary THM modelling of Task A-1

T.S. Nguyen, Canadian Nuclear Safety Commission, Canada

2.1 Introduction

The DECOVALEX-THMC project is an international co-operative project, initiated by SKI, the Swedish Nuclear Power Inspectorate, to support the development of mathematical models of coupled T(Thermal) H(Hydrological) M(Mechanical) and C (chemical) processes in the host rock of potential sites for nuclear fuel waste repositories. The objective of Task A of DECOVALEX-THMC is to assess the implications of coupled THM processes in the near field of a typical repository on its long-term performance. The proposed work is an actual working example where the engineering experts would work in collaboration and interact with performance/safety analysts and experimentalists on a realistic case study of a repository. The proposed work is an example of integration of model development/calibration and interpretation of laboratory and in-situ data towards the final goal of building confidence to the PA process. The repository we consider is a hypothetical repository in the Canadian Shield. The geological setting, the physical characteristics of the spent fuel, engineered barriers and host rock, as well as the geometrical configuration of the repository are given detailed in Chapter 1.

This chapter presents the CNSC's results for sub-task A-1 for the preliminary and simplified modelling of the THM behaviour in the near field of the repository.

2.2 General Modelling approach

First we performed uncoupled transient thermal analysis of one emplacement horizontal borehole as shown in Figure 2.1. Assuming repetitive symmetry, the side boundaries are prescribed as adiabatic. The top boundary corresponds to the ground surface and is maintained at a constant temperature of 5oC. The geothermal gradient is 0.012oC/m; the bottom boundary is at a depth of 1650 m, and consequently is maintained at a constant temperature of 25oC. The heat generated by the waste varies as a function of time as shown in Figure 1.13. The spacing between the containers in one borehole is represented by $2c$; the centreline distance between the borehole is represented by $2p$ as shown in Figure 2.1. The reference design is: $p=27.5$ m and $c=2.8$ m. In the uncoupled thermal analyses, we used different alternative combinations of p and c in order to determine their effects on the maximum temperature.

In order to save computer time, we include only a section of a room-and-pillar unit, spanning 50 m above and below the centreline of the horizontal emplacement borehole (Figure 2.2).

In order to predict the T-H-M near-field behaviour, a coupled T-H-M transient analysis was performed with the latest version of the FEM code FRACON (Nguyen et al., 2005), using the reference dimensions as shown in Figure 1.11 .

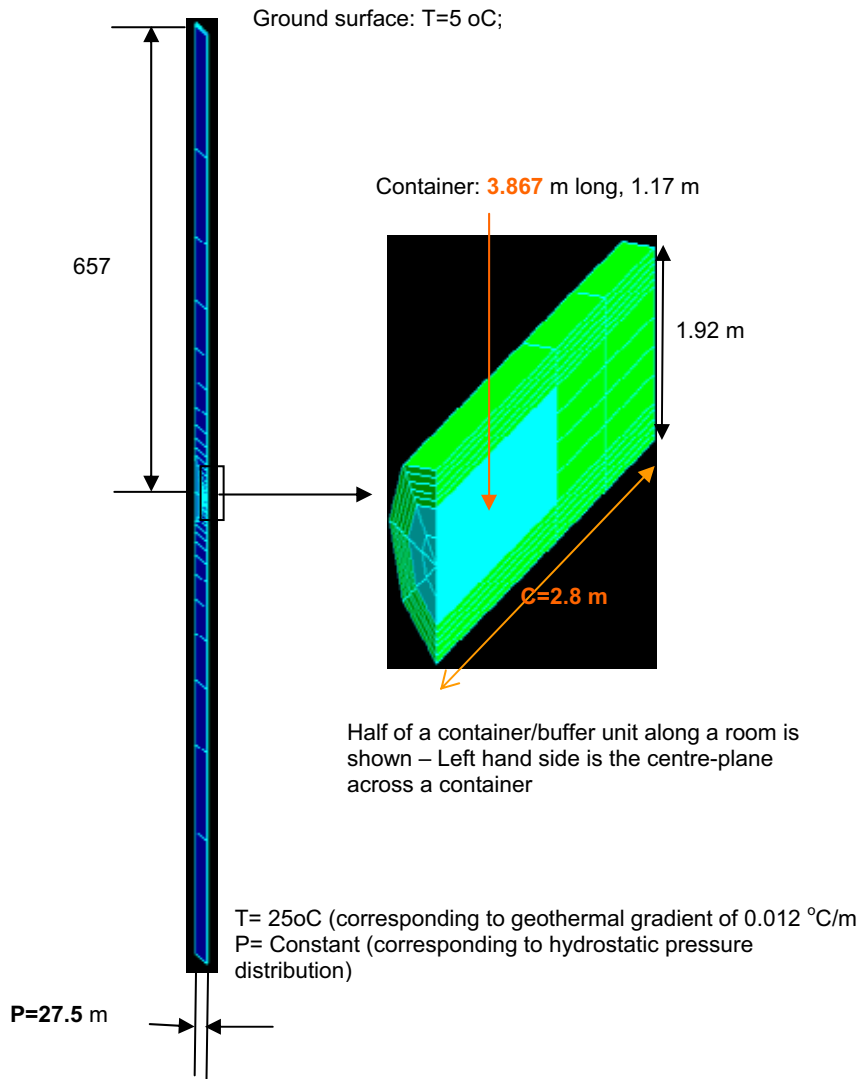


Figure 2.1: Finite element model and boundary conditions for thermal analyses

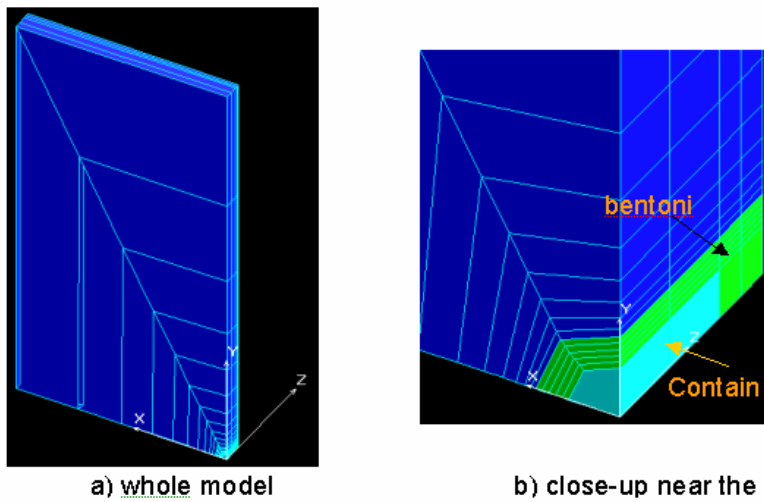


Figure 2.2: Finite element model for coupled THM analysis

The governing equations incorporated in the FRACON code were derived from an extension of Biot's theory of poro-elasticity to include the T-H-M behaviour of saturated and unsaturated rock and bentonite. A detailed description of the governing equations and the constitutive relationships for the MX-80 bentonite are given in Sections 2.3 and 2.4.

In addition, we assumed symmetry by including only the top half of the geometry. The top boundary is subjected to an overburden stress of 17 MPa; zero normal displacement is imposed on the bottom ($y=0$) and right ($z=0$) boundaries from symmetry considerations. The left boundary is subjected to the maximum horizontal in-situ stress of 62 MPa which prevails at a depth of 650 m. As a further simplification, we ignored the minimum horizontal stress, and instead assumed plane strain conditions (e.g. the front and back boundaries are maintained at zero normal displacements). The top boundary of the model is prescribed a time history of the temperature resulting from the output of the uncoupled thermal analyses that considered the whole domain. All other boundaries are adiabatic from symmetry considerations. From a hydraulic point of view, the top boundary is maintained at a constant pressure of 6.45 MPa, which corresponds to hydrostatic conditions at 650 m depth. All other boundaries are impermeable, due to symmetry.

As specified in Chapter 1, the analyses were performed in the following sequential stages:

- i) The whole web of rock was consolidated under the overburden and maximum in-situ stresses in order to establish the initial stress and pore pressure in the system.
- ii) Excavation was simulated by suddenly changing the elements inside the borehole into void elements, and at the same time imposing atmospheric pressure ($p=0$) inside the borehole. This stage was simulated for a period of 70 years.
- iii) Emplacement of the container and the bentonite was simulated by instantaneously changing the properties of the elements inside the borehole. The properties of the bentonite and container are described in section 2.5. We specify time $t=0$ at the start of this phase which we simulated for a period of 1000 years.

As detailed in section 2.5, some input properties of the rock and bentonite were directly specified by OPG (Appendix A). However many THM properties have to be assumed, from the authors' experience with similar projects (Nguyen, Selvadurai and Armand, 2005), or from the literature.

2.3. Mathematical model and governing equations

The prediction of the T-H-M behaviour of the bentonite and the rock was performed by solving the following coupled equations of poroelasticity, for a variably saturated material, with the Finite Element code FRACON:

$$\frac{\partial}{\partial x_i} \left(\kappa_{ij} \frac{\partial T}{\partial x_j} \right) + q = \rho C \frac{\partial T}{\partial t} \quad (2.1)$$

$$\begin{aligned}
& \frac{\partial}{\partial x_i} \left(\frac{\rho_w k_{ij} K_r}{\mu} \left(\frac{\partial p}{\partial x_j} + \rho_w g_j \right) \right) - \frac{\partial}{\partial x_i} \left(D_T \frac{\partial T}{\partial x_i} \right) \\
& + \rho_w \left[G_s (1-n) \frac{dw}{dp} \right] \frac{\partial p}{\partial t} + \rho_w \left[\frac{-nS}{K_w} + S \left(S - G_s \frac{w}{n} \right) \frac{n-\alpha}{K_s} \right] \frac{\partial p}{\partial t} \\
& + \rho_w (S\alpha) \frac{\partial}{\partial t} \left(\frac{\partial u_k}{\partial x_k} \right) + \rho_w S ((1-\alpha)\beta - n\beta_w - (1-n)\beta_s) \frac{\partial T}{\partial t} = 0
\end{aligned} \tag{2.2}$$

$$G \frac{\partial^2 u_i}{\partial x_i \partial x_j} + (G + \lambda) \frac{\partial^2 u_j}{\partial x_i \partial x_j} + \alpha S \frac{\partial p}{\partial x_i} - \beta K_D \frac{\partial T}{\partial x_i} + F_i = 0 \tag{2.3}$$

The primary unknowns of the above equations are: T, temperature; u_i , displacement, and p, pore pressure (tension is positive). These variables are functions of both the spatial variables (x_i) and time (t).

The above equations were derived within the framework of Biot's (1941) theory of consolidation, from energy, mass and momentum conservation considerations. A summary of the meaning and hypotheses used for each equation is given as follows:

a) Equation of heat conservation: Equation (2.1) is the equation of conservation of heat, where heat conduction is assumed to be the only mechanism of heat transport. In this equation, κ_{ij} is the thermal conductivity tensor (W/m⁰ C), ρ is the density of the bulk medium (kg/m³), C is the bulk specific heat of the medium (J/kg/ ⁰ C) and q accounts for distributed heat generation in the poroelastic medium (W/m³).

b) Equation of pore water flow: Equation (2.2) is the equation of pore water flow in the saturated-unsaturated porous medium, derived from considerations of mass conservation.

The first term of the equation results from a generalization of Darcy's law of water flow in variably saturated porous media. In this term, k_{ij} is the saturated permeability tensor (m²); K_r (non-dimensional) is the relative permeability of unsaturated media and is a function of the degree of saturation S (For $S=1$, $K_r=1$); μ (kg/m/s) is the viscosity of water, ρ_w is the density of water, which are both functions of temperature.

The second term represents vapor flow due to thermal gradients. In this term D_T (m²/s) is the coefficient of thermal vapour diffusivity.

The third term represents water retention due to the unsaturated state of the medium. In this term, w is the gravimetric water content, n is the porosity and G_s is the specific gravity of the solid particles. When the medium is fully saturated, w is independent of p and this term becomes zero.

The fourth term represents water retention due to compressibility of the water and the solid phase, where $1/K_w$ is the coefficient of compressibility of water (Pa⁻¹) and $1/K_s$ is the coefficient of compressibility of the solid phase (Pa⁻¹).

The fifth term represents water retention due to the consolidation of the porous medium.

The sixth term represents water flow due to the difference in thermal expansion between the water and the solid material, where β_w and β_s (1/⁰C) are the coefficient of volumetric thermal expansion of the water of the solid material, respectively.

c) Equation of equilibrium: Equation (2.3) is the equation of equilibrium of the porous medium. In this equation, it is assumed that the medium is non-linearly elastic, and G (Pa) and λ (Pa) are Lamé's constants of elasticity and β is the coefficient of volumetric thermal expansion of the solid matrix. G and λ can also be expressed as functions of the more commonly used Young's modulus E (Pa) and Poisson's ratio ν (non-dimensional). Also, α is Biot's coefficient. In this work, the coefficients of elasticity are assumed constant when the material is saturated; when the material is unsaturated, the coefficients of elasticity and Biot's coefficient α are expressed as functions of suction and the void ratio, as outlined in Section 4.

A Galerkin approach was used to approximate the governing equations in the conventional finite element matrix form. Three types of elements are available in the FRACON code: isoparametric 20-noded brick elements, isoparametric 15-noded prismatic elements, and 16-noded special joint elements. In order to avoid numerical oscillation, a mixed formulation is adopted, where displacements u_i are calculated at all the nodes, and pore pressure and temperature are calculated at the corner nodes of the elements only. A modified Newton-Raphson procedure was adopted to account for the nonlinearity of the governing equations induced by variable material properties.

2.4. Equations of nonlinear poro-elasticity for the unsaturated bentonite

We adopted the following form of the state surface equation (ENRESA, 1985) to describe the mechanical/hydraulic behaviour of the bentonite in the unsaturated state:

$$e = A + B \ln(-\sigma''_m) + C \ln(s + p_a) + D \ln(-\sigma''_m) \ln(s + p_a) \quad (2.4)$$

where $\sigma''_m = \frac{\sigma_{kk}}{3} - p_g$ is the mean net stress, p_g the gas pressure, $s = p_g - p$ the suction, p_a the atmospheric pressure, e the void ratio: $e = n/(1-n)$ and A , B , C and D the empirical constants, respectively. The increment of the void ratio can be expressed as:

$$de = \frac{\partial e}{\partial \sigma''_m} d\sigma''_m + \frac{\partial e}{\partial p} ds \quad (2.5)$$

Maintaining Hookean behaviour, the incremental equation of elasticity for isothermal poroelasticity can be written as:

$$d\sigma''_{ij} = 2Gde_{ij} + \delta_{ij} \lambda de_{kk} + \delta_{ij} \alpha S ds \quad (2.6)$$

where G and λ are the Lamé's constants, α Biot's coefficient, S degree of saturation, σ''_{ij} the net stress tensor; e_{ij} the strain tensor and δ_{ij} is the Kroenecker delta, respectively.

Equation (2.6) is based on Biot's (1941) formulation as extended to unsaturated soil, where net stress and suction are used as the state variables instead of total stress and

porewater pressure. This approach was also adopted by Fredlund and Rahardjo (1993) and assumes that the medium is isotropic, linear and elastic, at least from an incremental perspective.

From (2.6), the incremental mean net stress is given by:

$$d\sigma''_m = \left(\frac{2G}{3} + \lambda \right) de_v + \alpha S ds \quad (2.7)$$

$$d\sigma''_m = K_D de_v + \alpha S ds \quad (2.8)$$

with $de_v = de_{kk}$, incremental volumetric deformation, and K_D the bulk modulus is given by:

$$K_D = \lambda + \frac{2G}{3} = \frac{E}{3(1-2\nu)} \quad (2.9)$$

The volume variation is given by:

$$de_v = \frac{de}{1+e} \quad (2.10)$$

Thus, using (2.5):

$$de_v = \frac{1}{1+e} \left[\frac{\partial e}{\partial \sigma''_m} d\sigma''_m + \frac{\partial e}{\partial s} ds \right] \quad (2.11)$$

Comparing (2.8) and (2.11), one obtains:

$$\frac{1}{K_D} = \left(\frac{1}{1+e} \right) \frac{\partial e}{\partial \sigma''_m} \quad (2.12)$$

$$\frac{-\alpha S}{K_D} = (1+e) \frac{\partial e}{\partial s} \quad (2.13)$$

Performing the partial differentiation of (2.4), one obtains:

$$K_D = \frac{(1+e)\sigma''_m}{B + D \ln(s + p_a)} \quad (2.14)$$

and

$$\alpha = -\frac{1}{S} \frac{\sigma''_m}{B + D \ln(s + p_a)} \frac{C + D \ln(-\sigma''_m)}{s + p_a} \quad (2.15)$$

From elementary phase relationships in soil mechanics, one has $S = \frac{G_s w}{e}$, where w is the water content and G_s specific weight of the solids.

As detailed in section 2.5, an empirical equation relating water content and suction was determined for the bentonite, which does not depend on the dry density:

$$w = 29 \exp(-0.012s) \quad (2.16)$$

where log is the decimal logarithmic function (base 10), w is in %, and s is in MPa.

From equation (2.4):

$$\sigma_m'' = -\exp\left(\frac{e - A - C \ln(s + p_a)}{B + D \ln(s + p_a)}\right) \quad (2.17)$$

Substituting (2.17) into equations (2.14) and (2.15), K_D and α are expressed entirely as functions of s and e .

2.5. T-H-M input properties

The THM modelling proposed in the previous section contains a large number of input parameters. Most of the basic properties of the granitic rock and the bentonite were specified by OPG (Appendix A) and were directly input to the model. For the granite, we assumed a Biot's coefficient of 0.6 (see Table 2.1). The permeability of $6.9 \times 10^{-19} \text{ m}^2$ is also specified by OPG for a depth of 650 m; however we only modelled the case of a constant permeability, and do not consider the case of a variable permeability as specified in the task definition (see Chapter 1).

The rock can desaturate due to suction in the bentonite. The water retention characteristics of the rock are modeled using the curves shown in Fig.2.3, as suggested by Thomas et al. (2002). The properties of the bentonite as listed in Table 2.2 were specified by OPG and were directly input into the models, without considering the gap to be filled with bentonite pellets. In Table 2.2, "dry" means with 4% residual water saturation level "as-placed" means with as-placed water saturation level. Gapfill properties are averaged over the gap space. Pellets will be higher density. Properties will change with saturation, and as the interior buffer blocks swell and expand into the more porous gapfill.

Table 2.1. Basic input properties for granite

Thermal conductivity (W/m°C)	3.0
Specific heat (kJ/kg°C)	0.845
Density (kg/m ³)	2650
Porosity (%)	0.3
Young's modulus (GPa)	60
Poisson's ratio	0.25
Coefficient of thermal expansion (10 ⁻⁶ /°C)	10
Biot's coefficient	0.6
Permeability (m ²)	6.9×10^{-19}

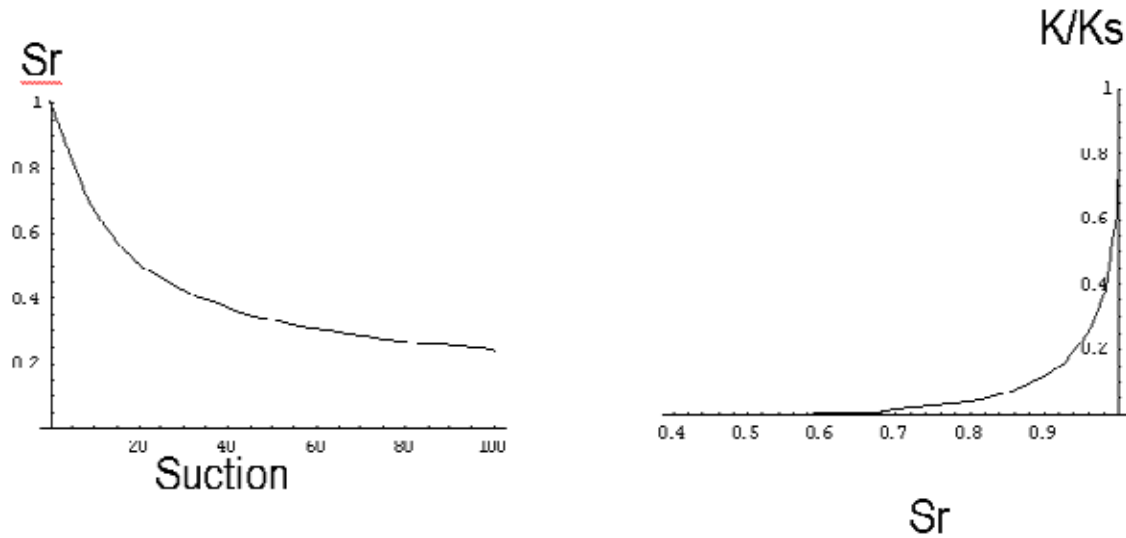


Figure 2.3: Water retention characteristics of granite. S_r is the degree of saturation; K/K_s is the relative permeability

Table 2.2. Bentonite properties specified by OPG

Property	Buffer	Gapfill ⁺
Composition	Bentonite blocks	Bentonite pellets
Density (kg/m^3)	1600 dry; 1850 as-placed	1400 dry; 1400 as-placed
Porosity (%)	41	49
As-placed saturation (%)	60	5
Gravimetric moisture content (%)	16 as-placed; 26 saturated	2 as-placed; 36 saturated
EMDD (kg/m^3)	1400	1180
Thermal conductivity ($\text{W/m}^\circ\text{C}$)	0.4 dry; 1.25 saturated	0.4 dry; 1.25 saturated
Specific heat ($\text{kJ/kg}^\circ\text{C}$)	0.8 dry	0.8 dry

In addition to the above basic properties, the unsaturated hydraulic and mechanical parameters have to be specified. From the data on the MX-80 bentonite described by Borgesson and Hernelind (1999), the water retention characteristics of the bentonite are illustrated in Figure 2.4a. The best-fit equation for the experimental data points is given by equation (2.16). The saturated permeability of the bentonite depends on the degree of compaction; from Borgesson and Hernelind (1999), a relationship between saturated permeability and void ratio as also shown in Figure 2.4b was input to the model. Also, from the same authors, a coefficient of vapour diffusivity $D_T=0.7 \times 10^{-11} \text{ m}^2/\text{s}$ was assumed.

The two important mechanical properties in our model are the bulk modulus and the Biot's coefficient, as detailed in section 2.3. Assuming $p_a = 0.1 \text{ MPa}$, and using the data on swelling tests provided by Borgesson and Hernelind (1999), the A, B, C, D coefficients of the state surface equation (2.4) for the unsaturated bentonite are estimated as $A=0.85$, $B=-0.0552446$, $C=-0.0406413$ and $D=0.00479977$, respectively.

Assuming the Poisson's ratio (ν) = 0.30, the values of the Young's modulus to be input to FRACON are calculated according to equation (2.15) and (2.17). The Biot's coefficient on the other hand is input to FRACON using equations (2.16) and (2.17). The resulting functions for the bulk modulus and Biot's coefficient of the bentonite are shown in Figs. 2.5 and 2.6, respectively.

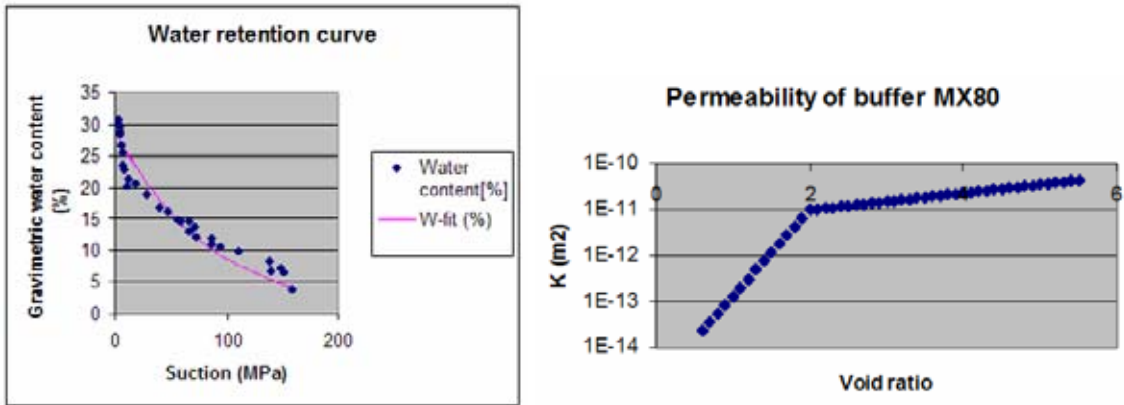


Figure 2.4: a) Water retention characteristics of MX-80 bentonite and b) saturated permeability function for MX-80 bentonite

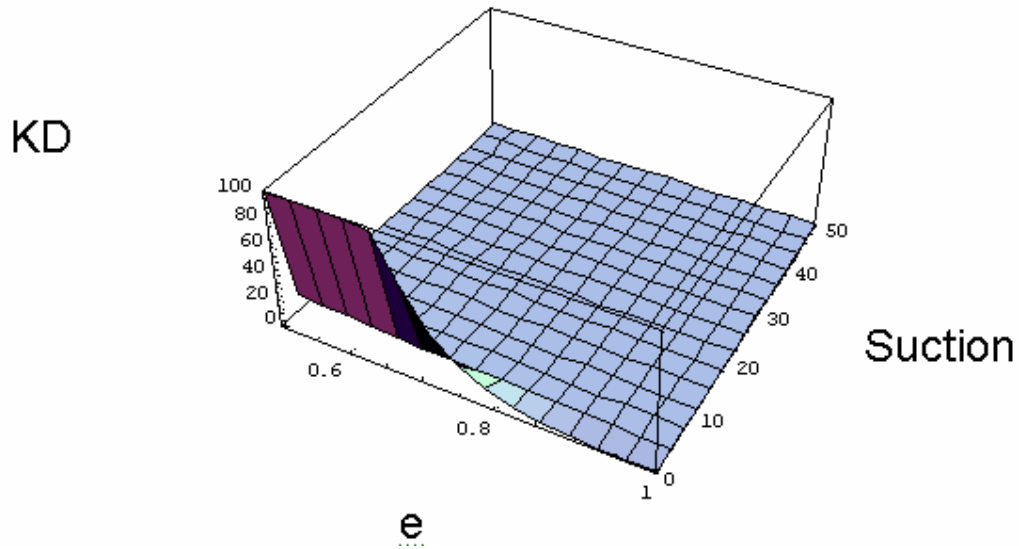


Figure 2.5: Bulk modulus of bentonite as a function of suction and void ratio

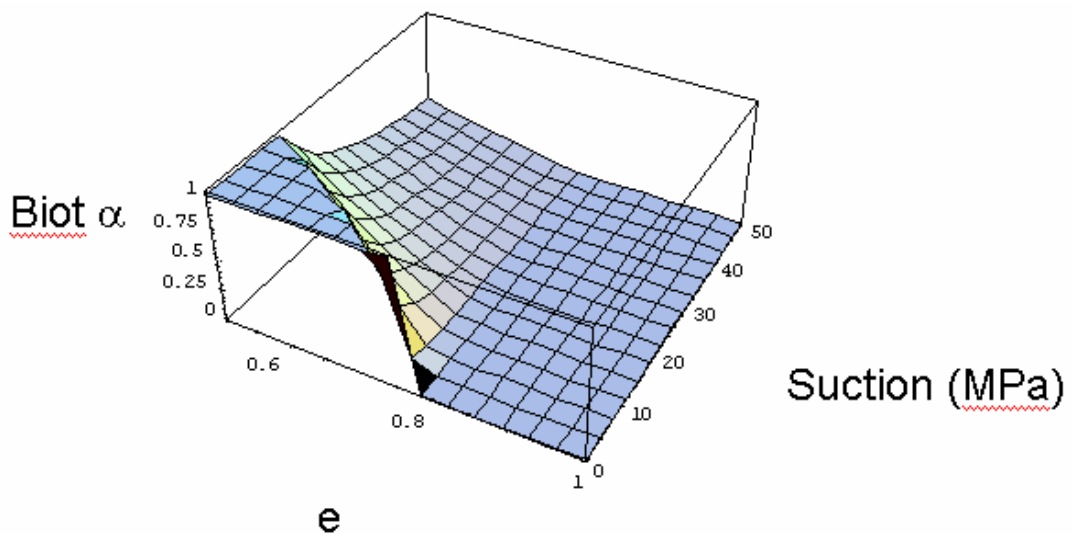


Figure 2.6: Biot's coefficient of bentonite as a function of suction and void ratio

2.6 Modelling results

Figure 2.7 shows the maximum temperature calculated from the uncoupled thermal analyses as a function of half-pillar width (p) and the spacing distance between containers in one single borehole (or pitch, $2c$). The maximum temperature is found at the centre of the container. As the pitch increases, the temperature decreases. As the centreline distance between boreholes ($2p$) increases, the maximum temperature decreases. However beyond a value of $p > 20$ m, the temperature reaches a minimal asymptotic value because the centre plane of the pillar does not act as a thermally reflective boundary anymore: heat dissipates as fast in the vertical as in the lateral directions.

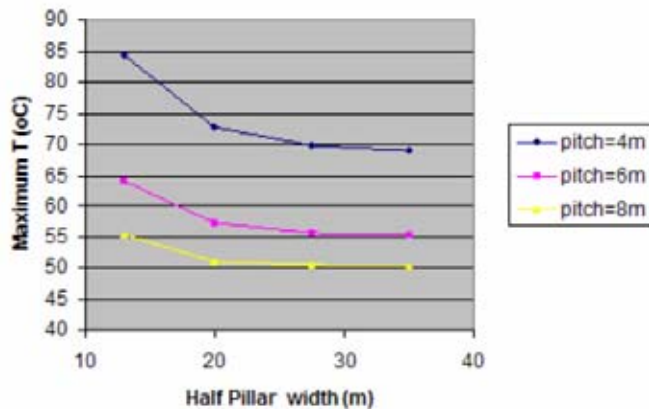


Figure 2.7: Results of uncoupled thermal analyses: Maximum temperature as a function of half-pillar width (p) and pitch ($2p$)

Figure 2.8 shows the pore pressure distribution after 70 years of excavation calculated from the fully coupled analysis. That distribution has probably already reached a quasi-steady state.

Figure 2.9 shows the evolution of temperature in the bentonite. A maximum temperature of 60 OC is reached approximately 10 years after waste emplacement, at the bentonite-container interface,

Figure 2.10a shows the re-saturation of the bentonite. Point B4 at the bentonite-rock interface attains full resaturation within the first year of waste emplacement. Points near the container are first subject to drying, however they fully resaturate at approximately 3-4 years.

Figure 2.10b shows the total horizontal stress evolution in the bentonite. The total stress is the sum of pore pressure, swelling pressure and thermal stresses. Maximum compressive stresses of approximately 15 MPa are attained at 3-4 years.

Figure 2.11 shows the stress paths for two points, one on the side and one on the roof of the borehole. Both points indicate that damage of the rock is possible, using the Hoek and Brown criterion with the two sets of parameters specified by OPG. The point on the side is subject to tensile failure on excavation; this mode of failure seems to worsen after waste emplacement. The point on the roof is subject to failure at excavation, due to a combination of an increase in the major principal stress, and a decrease in the minor principal stress. After waste emplacement, the stability seems to improve due to an increase in the minor principal stress due to the development of swelling pressure in the bentonite.

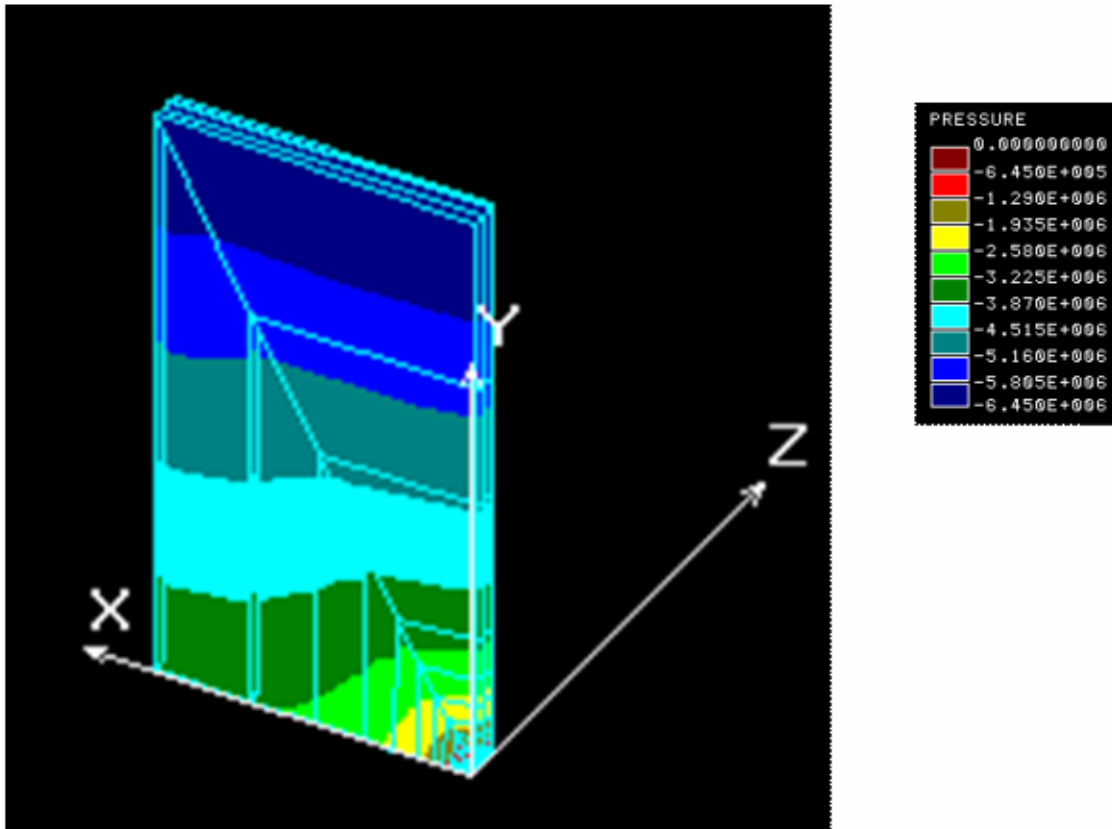


Figure 2.8: Pore pressure distribution seventy years after excavation

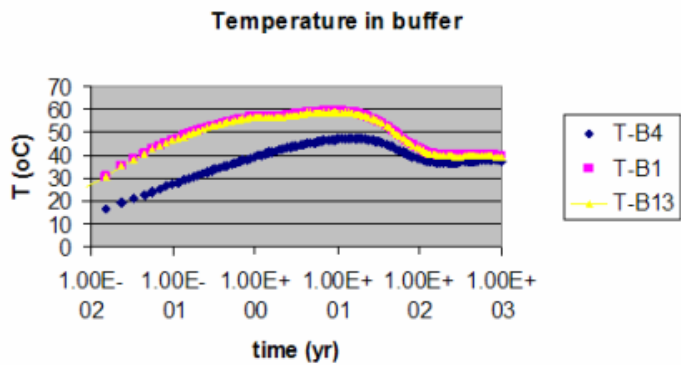


Figure 2.9: Temperature evolution in bentonite after waste emplacement

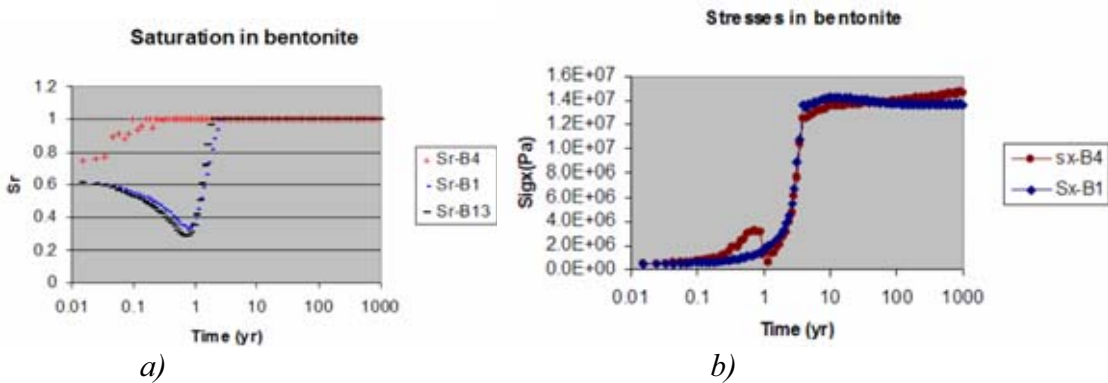


Figure 2.10: a) Resaturation time and b) total horizontal stress in bentonite

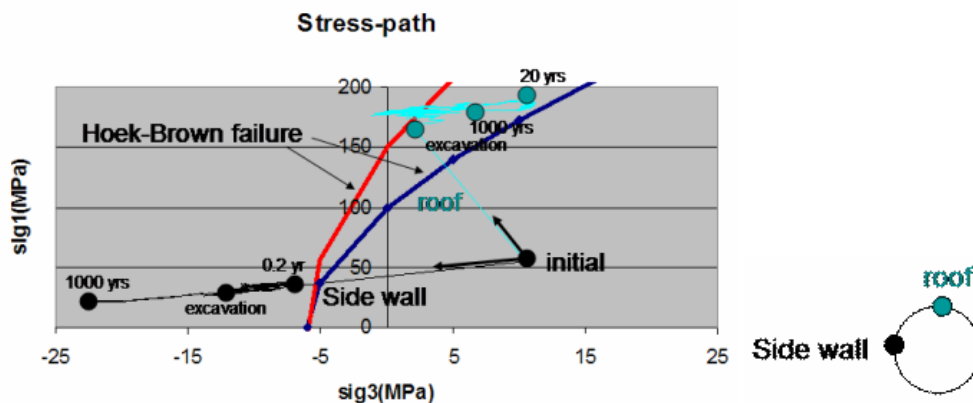


Figure 2.11: Stress evolution and stability in near field rock

2.7 Conclusions

The purpose of the preliminary THM modelling presented here is to have a first-cut appreciation of the problem. Many simplifications and assumptions were introduced and the results should be considered with caution. However, a few points of concern were identified and would guide us in the next phases of task A:

- The MX-80 bentonite exhibits very nonlinear THM behaviour. In particular, the response of the bentonite is particularly sensitive to the parameters of the state surface equations.
- The preliminary results show that an important damage zone could be formed around the waste emplacement roles; the extent of this damage zone should be better predicted, as well as its hydraulic and mechanical properties.
- The variation of rock permeability with stress or strain could have a significant influence on the resaturation time of the bentonite.

In preparation for a final THM model of the test case considered here, our next step would be to refine our constitutive relationships and parameters for both the bentonite and the granite. A series of laboratory and in-situ tests will be used in order to perform that model refinement.

References

- Biot, M.A., *General theory of three dimensional consolidation*. J. Appl. Phys., 1941 (12): 15-164.
- Borgesson, L. and Hernelind, J., *Coupled thermo-hydro-mechanical calculations of the water saturation phase of a KBS-3 deposition hole – Influence of hydraulic rock properties on the water saturation phase*. SKB report TR-99-41, SKB, 102 40 Stockholm, Box 5864. 1991.
- ENRESA. *FEBEX full-scale engineered barriers experiment in crystalline host rock-Bentonite: origin, properties and fabrication of blocks*. Publicacion Tecnica 05/98. ENRESA. Emilio Vargas, 7-28043, Madrid. 1998.
- Fredlund, D. and Rahardjo, H., *Soil mechanics for unsaturated soils*. John Wiley, N.Y. 1933.

- Nguyen, T.S., Selvadurai, A.P.S. and Armand, G., *Modelling the FEBEX THM experiment using a state surface approach*. Int. J. Rock Mech. Min. Sci., 2005; 42(5-6): 639-651.
- Thomas, H.R., Cleall, P.J. and Mitchell, H.P., *Comparison of physical measurements and a finite element numerical simulation of water uptake and distribution in the isothermal test*. OPG report 0818-REP-01300-10042-R00, OPG, NWMD, 700 University Av. Toronto, Canada, M5G 1X6. 2002.

3. DECOVALEX-THMC Task A-1 – modelling report by STUK

Petri Jussila, Helsinki University of Technology / Radiation and Nuclear Safety Authority, Finland

3.1 Introduction

The approach of the present report to model porous media is based on thermomechanics and mixture theory. The model describes the behavior of the mixture via proper choices of free energy and dissipation function. The free energy of the system is chosen to take into account the individual nondissipative behaviors of the constituents and their mutual interactions, in particular, adsorption and moisture swelling. The choices for the interaction terms are based on the equilibrium conditions for the water species in different combinations of the constituents. The resulting thermodynamically consistent macroscopic model can be fitted to coupled experiments and applied to THM-simulation of porous media by finite element method. A rigorous derivation of the general theory is presented elsewhere (Jussila (2006), Jussila and Ruokolainen (2006)).

The current report presents the application of the model to the preliminary simulation of a hypothetical repository involved in Task A-1 of the Decovalex-THMC project.

The numerical calculations are performed with ELMER (CSC, 2006), which is a software package for solving coupled partial differential equations generated by multiphysics problems in continuum mechanics. The program was developed at CSC in collaboration with Finnish universities, research centers and industry. CSC is the Finnish IT center for science, governed by the Ministry of Education. A particular form of the program is being created in cooperation with the experts of CSC to solve the problems presented here.

3.2 The model

3.2.1 Preliminaries

The multiconstituent system consists of solid skeleton (s), liquid water (l), water vapor (v), and air (a). Vapor and air occupy the same gaseous (g) volume fraction. The molar volume fraction

$$\xi_k = \begin{cases} \beta_k, & \text{for } k \in \{s, l\} \\ x_k \beta_g, & \text{for } k \in \{v, a\}, \end{cases} \quad (3.1)$$

of constituent k is defined by means of the volume fraction $\beta_j = v_j / v_{\text{rev}}$ of the phase $j \in \{s, l, g\}$, where $v_{\text{rev}} = \sum_j v_j$ is the representative elementary volume, and the molar

fraction $x_k = n_k / (n_a + n_v)$ for $k \in \{a, v\}$, where n_k is the mole number. Apparently, we have $\sum_k \xi_k = 1$, $\xi_k > 0$, $\forall k$. The intrinsic densities $\tilde{\rho}_k$ are related to the apparent densities $\rho_k = m_k / v_{\text{rev}}$ by the equation $\rho_k = \xi_k \tilde{\rho}_k$. Porosity $\eta = 1 - \xi_s$, liquid saturation $\chi = \xi_l / (1 - \xi_s)$, and vapor fraction $\zeta = \xi_v / (\xi_a + \xi_v)$ are defined as alternative variables.

The absolute velocity of constituent k is denoted by \mathbf{U}_k and a relative velocity by $\mathbf{V}_k = \mathbf{U}_k - \mathbf{U}_*$, where \mathbf{U}_* is a reference velocity. The material time derivative is $d^k/dt = \partial/\partial t + \mathbf{U}_k \cdot \nabla$. Tensors can be divided into deviatoric and spherical parts, e.g., the Cauchy stress tensor of constituent k is $\boldsymbol{\sigma}_k = \boldsymbol{\sigma}_k^D + (\text{tr}(\boldsymbol{\sigma}_k)/3)\mathbf{I} = \boldsymbol{\sigma}_k^D - p_k \mathbf{I}$, where p_k is the pressure. Strain and rate of deformation of constituent k are defined by $\boldsymbol{\varepsilon}_k = (\nabla \mathbf{u}_k + (\nabla \mathbf{u}_k)^T)/2$ and $\mathbf{D}_k = (\nabla \mathbf{U}_k + (\nabla \mathbf{U}_k)^T)/2$, respectively, where \mathbf{u}_k is the displacement of constituent k .

The reversible behavior of the system is described by the constituent free energies. The state variables are chosen to be the molar volume fractions ξ_k , intrinsic densities $\tilde{\rho}_k$, and strains $\boldsymbol{\varepsilon}_k$ of the constituents, and the common temperature T . Dissipative behavior of the system is described by the dissipative variables and the dissipation function. (Jussila, 2006)

3.2.2 Conservation equations

The final primary variables are porosity η , gaseous pressure \hat{B} , saturation χ , solid phase displacement $\mathbf{u} = \mathbf{u}_s$, temperature T , and vapor fraction ζ . The conservation equations for solid mass, air mass, water mass, momentum, and energy are reduced to

$$\frac{\partial \rho_s}{\partial t} + \nabla \cdot \left(\rho_s \frac{\partial \mathbf{u}}{\partial t} \right) = 0, \quad (3.2)$$

$$\frac{\partial \rho_a}{\partial t} + \nabla \cdot \left(\rho_a \mathbf{V}_a + \rho_a \frac{\partial \mathbf{u}}{\partial t} \right) = 0, \quad (3.3)$$

$$\frac{\partial (\rho_l + \rho_v)}{\partial t} + \nabla \cdot \left(\rho_l \mathbf{V}_l + \rho_v \mathbf{V}_v + (\rho_l + \rho_v) \frac{\partial \mathbf{u}}{\partial t} \right) = 0, \quad (3.4)$$

$$\nabla \cdot \boldsymbol{\sigma} + \rho \mathbf{g} = 0, \quad (3.5)$$

$$(\rho c)_{\text{eff}} \frac{\partial T}{\partial t} - (e_v - e_l) \theta_l + \nabla \cdot \mathbf{q} - Q = 0, \quad (3.6)$$

respectively, where $\boldsymbol{\sigma} = \sum_k \boldsymbol{\sigma}_k$, $\rho = \sum_k \rho_k$, $(\rho c)_{\text{eff}} = \sum_k \rho_k c_k^v$, and $\mathbf{q} = \sum_k \mathbf{q}_k$. Here e_k is the specific internal energy, θ_l is the rate of liquid mass production, c_k^v is the specific heat at constant volume, \mathbf{g} is the gravitational vector, and Q is the source of energy.

3.2.3 Constitutive relations

The needed constitutive relations are reduced to the following respective forms of Clausius-Clapeyron equation, stress-strain relation, gaseous phase state equations, Darcy's law for liquid, the results of Darcy's law for gas and Fick's law for vapor and air, Fourier's law for heat conduction, and to the internal energy difference of the water species

$$\ln \frac{\zeta \hat{B}}{(\zeta \hat{B})_0} = \frac{M_v}{RT} \left[L \frac{T - T_0}{T_0} + (c_v^p - c_l^p) T \ln \frac{T}{T_0} + \frac{\hat{B} - \hat{B}_0}{\tilde{\rho}_1} \right] + \frac{\partial(\xi_1 f)}{\partial \xi_1} + \frac{1}{\tilde{\rho}_1} \frac{M_v}{RT} \left[\xi_s \frac{\partial f_{\Pi}}{\partial \xi_1} \hat{B}_0 \text{tr} \boldsymbol{\varepsilon} + \frac{1}{2} \xi_s \frac{\partial K_s}{\partial \xi_1} (\text{tr} \boldsymbol{\varepsilon})^2 \right], \quad (3.7)$$

$$\boldsymbol{\sigma} = 2\xi_s G \boldsymbol{\varepsilon}^D - \left(\hat{B} - \xi_s K \text{tr} \boldsymbol{\varepsilon} - \xi_s f_{\Pi} \hat{B}_0 \right) \mathbf{I}, \quad (3.8)$$

$$\hat{B} = \tilde{\rho}_k \frac{RT}{M_k}, \quad k \in \{a, v\}, \quad (3.9)$$

$$\rho_1 \mathbf{V}_1 = -\tilde{\rho} \frac{k_1}{\mu_1} \left[\nabla \hat{B} - \tilde{\rho}_1 \mathbf{g} + \tilde{\rho}_1 \frac{RT}{M_v} \nabla \left(\frac{\partial(\xi_1 f)}{\partial \xi_1} \right) + \tilde{\rho}_1 \frac{R}{M_v} \xi_1 \frac{\partial f}{\partial \xi_1} \nabla T + \xi_s \frac{\partial f_{\Pi}}{\partial \xi_1} \hat{B}_0 \nabla (\text{tr} \boldsymbol{\varepsilon}) + \hat{B}_0 \text{tr} \boldsymbol{\varepsilon} \nabla \left(\xi_s \frac{\partial f_{\Pi}}{\partial \xi_1} \right) \right], \quad (3.10)$$

$$\rho_v \mathbf{V}_v = -\zeta \tilde{\rho}_v \frac{k_g}{\mu_g} \nabla \hat{B} - \tilde{\rho}_v \beta_g D \nabla \zeta, \quad (3.11)$$

$$\rho_a \mathbf{V}_a = -(1 - \zeta) \tilde{\rho}_a \frac{k_g}{\mu_g} \nabla \hat{B} + \tilde{\rho}_a \beta_g D \nabla \zeta, \quad (3.12)$$

$$\mathbf{q} = \sum_k \mathbf{q}_k = -\sum_k \xi_k \lambda_k \nabla T = -\lambda \nabla T, \quad (3.13)$$

$$e_v - e_l = l_0 + (c_v^p - c_l^p) (T - T_0) - \frac{RT}{M_v}, \quad (3.14)$$

where M_k is the molar mass, R is the universal gas constant, c_k^p is the specific heat at constant pressure, l_0 is the latent heat of vaporization at the reference state,

$L = l_0 - (c_v^p - c_l^p) T_0$, $\boldsymbol{\varepsilon} \equiv \boldsymbol{\varepsilon}_s$ is the solid deformation, G is the shear modulus, K is the bulk modulus, k_k is the permeability, μ_k is the dynamic viscosity, D is the vapor-air

diffusivity, and λ_k is the heat conductivity. The subscript $(\)_0$ refers to a value at the reference state.

The choice of the respective adsorption and swelling functions f and f_Π is based on the equilibrium of the water species. In constant gaseous pressure experiments the suction and swelling pressures get the respective forms

$$p_c = -\tilde{\rho}_1 \frac{RT}{M_v} \frac{\partial(\xi_1 f)}{\partial \xi_1} - \xi_s \frac{\partial f_\Pi}{\partial \xi_1} \hat{B}_0 \text{tr}\boldsymbol{\epsilon} - \frac{1}{2} \xi_s \frac{\partial K_s}{\partial \xi_1} (\text{tr}\boldsymbol{\epsilon})^2, \quad (3.15)$$

$$\Pi = -\xi_s K \text{tr}\boldsymbol{\epsilon} - \left[\xi_s f_\Pi - (\xi_s f_\Pi)_{\text{init}} \right] \hat{B}_0. \quad (3.16)$$

which for confined experiments with zero deformation are reduced to

$$p_c^v = -\tilde{\rho}_1 \frac{RT}{M_v} \frac{\partial(\xi_1 f)}{\partial \xi_1}, \quad (3.17)$$

$$\Pi^v = -\xi_{s,\text{init}} (f_\Pi - f_{\Pi,\text{init}}) \hat{B}_0. \quad (3.18)$$

3.2.4 Parameters

The respective choices for the adsorption and swelling functions are

$$f(\xi_s/\xi_1) = \begin{cases} a_1 \left(\xi_s/\xi_1 - (\xi_s/\xi_1)_0 \right)^{a_2}, & \text{for } \xi_s/\xi_1 \geq (\xi_s/\xi_1)_0, \\ 0, & \text{for } \xi_s/\xi_1 < (\xi_s/\xi_1)_0, \end{cases} \quad (3.19)$$

$$f_\Pi(\xi_s/\xi_1) = a_3 \left(\xi_s/\xi_1 \right)^2 + a_4 \left(\xi_s/\xi_1 \right) + a_5, \quad (3.20)$$

where $a_{1\dots5}$ are non-dimensional parameters that determine how the interactions depend on the proportions of the solid and liquid volume fractions. They depend e.g. on the inner structure of the material, its permanent electrical charge, and specific surface. The swelling function parameters $a_{3,4,5}$ can be analytically determined by means of the experimental maximum confined swelling pressure Π_{max}^v and the fully swollen state $(\xi_s/\xi_1)_{\text{min}}$ (Jussila and Ruokolainen, 2006).

The swelling and suction parameters are fitted to the confined experiments for rock and MX-80 bentonite by means of the equations (3.17) and (3.18) as illustrated in Figure 3.1. The bulk modulus of bentonite is sought for in the following form

$$K = K_{\text{init}} \left[(\xi_s/\xi_1) / (\xi_s/\xi_1)_{\text{init}} \right]^b, \quad (3.21)$$

with the conventional relations between elasticity parameters $E = 3(1 - 2\nu)K$, $G = E/2(1 + \nu)$, where E is Young's modulus and ν is Poisson's ratio. The elasticity parameters of rock are assumed to be constants.

The permeability of porous medium is divided into medium dependent and fluid dependent parts as $k_k = k_{\text{sat}} k_{k,\text{rel}}$. The saturated permeability of rock was given as a function of the porosity

$$k_{\text{sat}} = a_{\text{sat}} \eta^3 + b_{\text{sat}}, \quad (3.22)$$

and the relative permeabilities of liquid and gas in rock are

$$k_{l,\text{rel}} = \sqrt{\chi} \left(1 - \left(1 - \chi^{1/\beta} \right)^\beta \right)^2, \quad k_{g,\text{rel}} = 1 - k_{l,\text{rel}}. \quad (3.23)$$

For bentonite the saturated permeability is assumed to be constant, relative permeability of liquid to be saturation dependent as $k_{l,\text{rel}} = \chi^3$, and the relative permeability of gas to be high $k_{g,\text{rel}} = 10^7$ to avoid gas pressure build-up in the buffer.

The heat conductivity of rock is taken as a constant while in bentonite saturation dependency is assumed by means of a specific sixth order polynomial introduced by the JAEA team of the current project.

For diffusivity of vapor-air mixture the experimental relation $D = D_{\text{ref}} (T/T_{\text{ref}})^\alpha$ is used. The effective specific heat of rock is $(\rho c)_{\text{eff}} = \eta \chi \tilde{\rho}_l c_l^p + (1 - \eta) \tilde{\rho}_s c_s^p$. The used parameter values are presented in Tables 3.1-3.5.

3.3 The analyses

3.3.1 T-analysis of rock, bentonite, and containers

The coupled energy equation (3.6) can be reduced to the traditional uncoupled temperature equation

$$\rho c \frac{\partial T}{\partial t} + \nabla \cdot \mathbf{q} - Q = 0, \quad (3.24)$$

which was solved with 2 year time steps in a 3D geometry for which $y \in (-657, 657)$ m and the container-to-container distance and tunnel-to-tunnel distance were sought for in the respective ranges of [5.6, 7.0] m and [25, 55] m. The 3D element mesh the close-ups of which are illustrated in Figure 3.2 involves 7271 nodes and 44 827 elements. The geometry consists of 3 separate materials (container, bentonite, and rock). The used constant material parameter values are presented in Table 3.4. The specific heat of bentonite is calculated by the equation $c = 800/(1+w) + 4200 w/(1+w)$ (Börgesson and Hernelind, 1999), where the as-placed water ratio is $w = 0.16$. The heat source density is calculated by dividing the given time dependent heat source by the total weight of the container 23 500 kg (Nguyen, 2004).

As a result the combination of the tunnel-to-tunnel and container-to-container distances that minimizes the repository area is (25.0, 6.44) m, see Figure 3.3. The maximum temperatures occurred between 18 and 26 years after the emplacement.

3.3.1 THM-analysis of rock

The coupled THM-system (3.2)-(3.14) is applied to the modelling of rock by neglecting the swelling interaction. Some intermediate calculations were performed with 2D and 3D geometries reaching from the ground surface $y = 657$ m to the symmetrical depth of $y = -657$ m. All the final results presented in the following, however, were calculated with a cut geometry for which $y \in (-300, 300)$ m.

a) Initial state

The in-situ THM state of rock is determined by the initial conditions of the problem. The initial condition was chosen in such a way that the system does not theoretically evolve from the initial state. This was also verified by performing calculations with a 2D geometry of rock without the tunnel.

The chosen initial conditions are

$$\eta = \eta_0 = 0.0031, \quad (3.25)$$

$$\hat{B} = \hat{B}_0 + \tilde{\rho}_1 (657 - y) g, \quad (3.26)$$

$$\chi = \chi_{\max} = 0.99, \quad (3.27)$$

$$\mathbf{u} = \mathbf{0}, \quad (3.28)$$

$$\sigma_{xx} = 56.3 \cdot 10^6 + (657 - y) 0.00866 \cdot 10^6 - \hat{B}, \quad (3.29)$$

$$\sigma_{yy} = ((1 - \eta) \tilde{\rho}_s + \eta \chi \tilde{\rho}_1) (657 - y) g - \hat{B}, \quad (3.30)$$

$$\sigma_{zz} = 40.7 \cdot 10^6 + (657 - y) 0.00866 \cdot 10^6 - \hat{B}, \quad (3.31)$$

$$T = 5 + 0.012(657 - y) + 273.15, \quad (3.32)$$

where \hat{B}_0 is the atmospheric pressure.

b) Code testing

The rock mass is modelled as an elastic continuum. To verify the mechanical part of the numerical Elmer program a case comparable to the available analytical solution (Jussila and Eloranta, 1997) for 2D steady state plane stress around a circular cavity in

an infinite continuum was formed. The respective analytical solutions for the radial and tangential stresses and the radial displacement by means of polar coordinates (r, φ) are

$$\sigma_r = -\frac{1}{2}(p_x + p_y) \left[1 - \left(\frac{R}{r} \right)^2 \right] - \frac{1}{2}(p_x - p_y) \left[1 - 4 \left(\frac{R}{r} \right)^2 + 3 \left(\frac{R}{r} \right)^4 \right] \cos 2\varphi, \quad (3.33)$$

$$\sigma_\varphi = -\frac{1}{2}(p_x + p_y) \left[1 + \left(\frac{R}{r} \right)^2 \right] + \frac{1}{2}(p_x - p_y) \left[1 + 3 \left(\frac{R}{r} \right)^4 \right] \cos 2\varphi, \quad (3.34)$$

$$u_r = -\frac{1}{2G} \left\{ \frac{1}{2}(p_x + p_y) \frac{R^2}{r} + \frac{1}{2}(p_x - p_y) \left[4(1-\nu) \frac{R^2}{r} - \frac{R^4}{r^3} \right] \cos 2\varphi \right\}, \quad (3.35)$$

where p_x and p_y are the known in-situ stresses in horizontal and vertical directions, respectively. The used parameter values in the code testing were $p_x = 56.3 \cdot 10^6 + 657 \cdot 0.00866 \cdot 10^6$ Pa, $p_y = ((1-\eta) \tilde{\rho}_s + \eta \chi \tilde{\rho}_1) (657 - y) g$ Pa, $G = 60$ GPa, $\nu = 0.202$, and the geometrical dimensions were $R = 0.96$ m, $x \in (0, 27.5)$ m, $y \in (-657, 657)$ m.

From Figure 3.4 it can be observed that the numerical solutions for the stresses coincide with the analytical ones. The numerical radial displacements illustrated in Figure 3.5 deviate slightly from the analytical solutions. The reason for the discrepancy can be attributed to the fixed boundary conditions. A larger calculation geometry would give a better coincidence. The main differences between the analytical and numerical set-ups are that in the numerical one we have $\sigma_{yy} = \sigma_{yy}(y)$ and the boundaries are fixed at finite distances from the tunnel.

c) The THM results of rock at 0 to 30 years

The post-excavational analysis was done in 3D domain of $x \in (0, 27.5)$ m, $y \in (-300, 300)$ m, and $z \in (0, 2.8)$ m with the circular tunnel perpendicular to the major principal stress. The calculations $t \in (0, 30)$ a involved 3 time steps of 10 years.

The boundary conditions were fixed values of the primary variables at the top and the bottom and symmetrical conditions at the vertical sides of the geometry. The mechanical boundary condition at the top was the atmospheric pressure and the weight of 357 m of fully saturated rock. The conditions at the tunnel boundary were zero radial stress, atmospheric pressure, and 50 % of relative humidity of the tunnel air. The latter two conditions yield a constant value of vapor fraction assuming fixed temperature at the tunnel depth. This is not strictly true because the coupled calculations affect the temperature slightly. The saturation at the tunnel surface is iterated at every time step to be compatible with the porosity, temperature, and vapor fraction according to the Clausius-Clapeyron equation (3.7).

The numerical results for the horizontal and vertical displacements, principal stresses, porosity, pore pressure, and saturation degree along the x - and y -axes at 10 and 30 years are illustrated in Figures 3.6-3.12.

3.3.2 THM-analysis of container, bentonite, and rock at 30 to 1000 years

The post-emplacment analysis involved three materials, time dependent heat production by the waste, and a time range of $t \in (30, 1000)$ years.

Originally, the fully coupled post-excavation results were planned to be used as an initial condition for the post-emplacment problem. Unfortunately, this was not successful. Furthermore, with the swelling interaction included convergence was achieved only for a couple of relatively small time steps. Consequently, to achieve numerical post-emplacment results up to 1000 years all three materials were assumed to appear at the same time at 30 years and the swelling of the buffer had to be discarded. The time evolution of temperature and saturation degree in selected points of the buffer is illustrated in Figure 3.13. The contour plots of temperature, pore pressure, and permeability at 30, 38, 100, and 1000 years are given in Figures 3.14-3.16. The time 38 years (8 years after emplacment) corresponds to the maximum temperature. The rock permeability is calculated by means of porosity by equation (3.22).

3.4 Discussion

The post-excavation problem is essentially 2-dimensional. The rock material is assumed elastic and the stresses get their final values at the first time step. The vertical displacement, however, does evolve during the whole post-excavation calculation period of 30 years because of the evolving pore pressure. The resulting downward movement of the whole rock mass is due to the decrease of the pore pressure around the tunnel. The maximum vertical displacement is of the order of 1 cm that should be observable in real situation. At 30 years the pressure field and the vertical displacement are still evolving and a steady state has not been reached.

The results suggest that the ventilation of the tunnel yields a small decrease in the rock temperature in the vicinity of the tunnel. More important is the reduction in saturation degree up to dozens of meters from the tunnel. The resulting initial condition for the post-emplacment THM-analysis would slow down the starting of the bentonite resaturation.

The given porosity-permeability-relation can not be very accurate. In particular, the results for the porosity near the tunnel floor and ceiling are below the given region. For that reason, the lower limit for the permeability was set to 10^{-19} m^2 in the numerical code. The cut-off value suggested by the coordinator was 10^{-21} m^2 . However, the use of such a small value resulted in numerical convergence problems and was thus discarded. Major numerical problems were encountered in the post-emplacment analysis. Because of this the post-excavation and post-emplacment problem had to be solved as separate cases. Furthermore, the swelling of the buffer had to be neglected in order to achieve results up to 1000 years. These assumptions led to partially unexpected and unusual results.

Temperature results are realistic. The maximum temperature of 63 °C is obtained at 8 years after emplacement and the temperature gradients decrease along with time as the temperature of the surrounding rock mass increases.

The results for saturation degree are partially unexpected. Points along the vertical axis seem to exhibit a traditional behaviour. The container surface (B2 and B3) is first dried followed by full resaturation in 50 years. This is slow but compatible with the previous experience with the current model. On the other hand, the results along the horizontal axis are unusual. The full resaturation of the container surface (point B1) takes more than 1000 years while the point at the rock surface (B4) keeps unsaturated and even dries further along with time. While the possibility of numerical errors can not be discarded there are many explanations for this behaviour based on the modelling approach and the computational set-up: i) The temperature gradient prevents the resaturation, which is not a sufficient explanation alone, though. ii) The used initial condition assuming all the materials appearing at the same time is not realistic. The in-situ stresses deform the tunnel and the buffer in such a way that the volume of the material along the x-axis increases. This results in opening of the pores and apparent drying of the rock and the buffer which seems to prevail. iii) A major driving force in the model for the liquid transport is the suction that depends on the porosity. The initial deformation of the tunnel surroundings leads to increased porosity along the x-axis and decreased porosity along the y-axis. As a consequence the suction ability of the material along the x-axis is relatively decreased, which prevents the resaturation of the same area. iv) The saturation degree as a state variable was assumed to be a continuous variable at the rock-buffer-interface which by definition is an error. If a full saturation prevailed at this interface this would not be a problem. For the current unsaturated situation the correct boundary condition should be a continuous suction. As a conclusion, the simulated unusual moisture field behavior in certain places of the domain is a combined result of various invalid assumptions in the modelling approach and in the computational set-up. These have to be corrected in the future work.

References

- Börgesson, H. and Hernelind, J., *Coupled thermo-hydro-mechanical calculations of the water saturation phase of a KBS-3 deposition hole*, SKB report TR-99-41, 1999.
- CSC - The Finnish IT Center for Science: 2006, ELMER [WWW document]
<http://www.csc.fi/Elmer/>
- Jussila, P. and Eloranta, E., *Analytical solutions of the mechanical behaviour of rock with applications to a repository for spent nuclear fuel*, STUK-YMO-TR 136, Helsinki 1997.
- Jussila, P., *Thermomechanics of Porous Media I: Thermohydraulic Model for Compacted Bentonite*, Transport Porous Med, 62, 81-107, 2006.
- Jussila, P., and Ruokolainen, J., *Thermomechanics of Porous Media II: THM Model for Compacted Bentonite*, Transport Porous Med, accepted for publication, 2006.
- Nguyen, T.S., *Influence of near field coupled thm phenomena on the performance of a spent fuel repository, Task A-1 -- Preliminary scoping calculations*, Rev. 1, April 2004.

Table 3.1: Reference values and common literature parameters.

\hat{B}_0	$1.01 \cdot 10^5$ Pa	M_v	0.018 kg/mol	D_{ref}	$0.216 \cdot 10^{-4}$ m ² /s
T_0	20 + 273.15 Pa	M_a	0.029 kg/mol	T_{ref}	273 K
ζ_0	0.023	μ_l	$1.0 \cdot 10^{-3}$ kg/(sm)	α	1.8
l_0	$2.45 \cdot 10^6$ J/kg	μ_g	$16.7 \cdot 10^{-6}$ kg/(sm)	c_v^p	$1.87 \cdot 10^3$ J/(kgK)
$\tilde{\rho}_l$	998 kg/m ³	R	8.314 J/(molK)	c_l^p	$4.18 \cdot 10^3$ J/(kgK)

Table 3.2: Rock parameters.

η_0	$0.31 \cdot 10^{-2}$	λ_s	3.0 W/(Km)	$\tilde{\rho}_s$	2650 kg/m ³
χ_{max}	0.99	c_s^p	845 J/(kgK)	E	60 GPa
ν	0.202	a_{sat}	$2.186 \cdot 10^{-10}$	b_{sat}	$-5.8155 \cdot 10^{-18}$
β	0.33	a_1	$0.6 \cdot 10^{-6}$	a_2	1.8

Table 3.3: Hydro-mechanical parameters for MX-80 bentonite.

a_1	a_2	Π_{max}^v	χ_{max}	e_{max}	K_{init}	b	ν
0.1	1.6	8.0 MPa	0.99	1.2	0.53 GPa	2.0	0.35

Table 3.4: Constant parameter values in the uncoupled thermal analysis.

	Rock	Bentonite	Container
ρ [kg/m ³]	2650	1850	8930
λ [W/(Km)]	3.0	0.95	380
c [J/(kgK)]	845	1269	390

Table 3.5: Initial values of MX-80 bentonite.

ρ_{dry} [kg/m ³]	w [-]	η [-]	χ [-]
1570	0.17	0.44	0.61

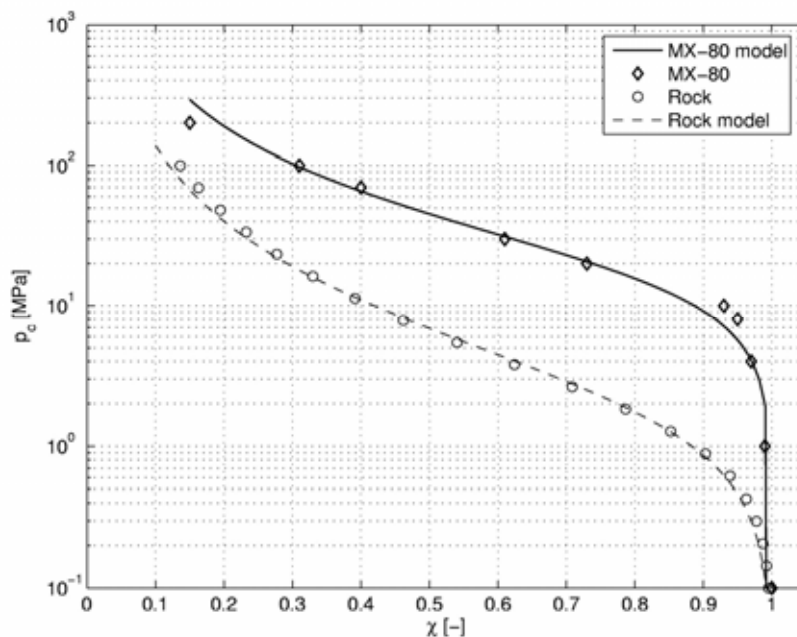


Figure 3.1a: Confined suction curves of rock and MX-80 bentonite.

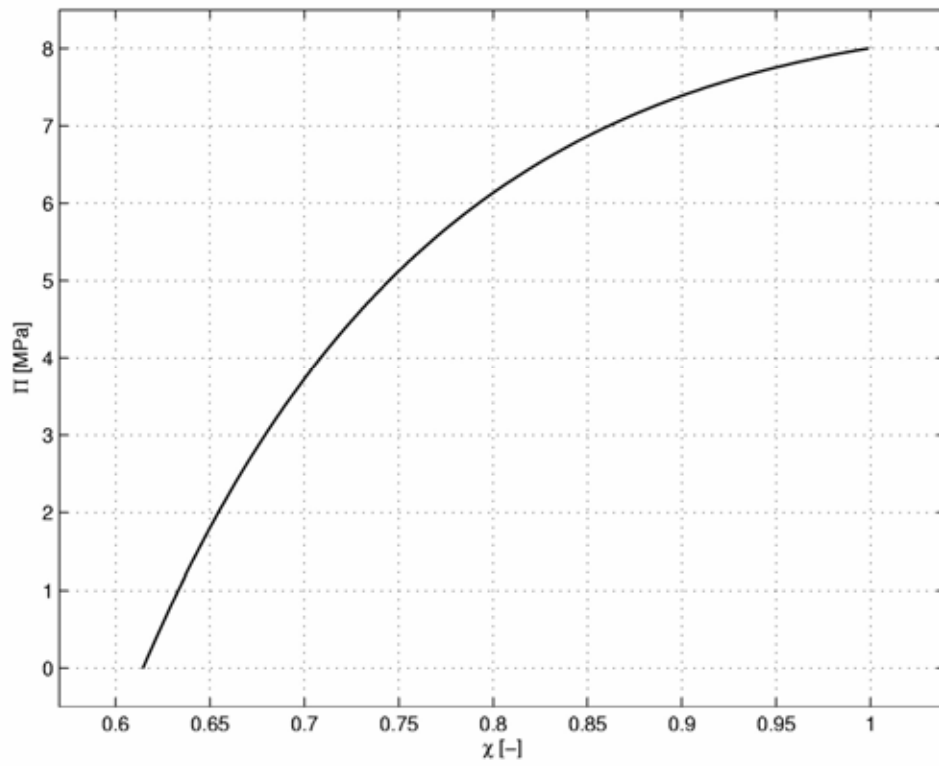


Figure 3.1b: Confined swelling pressure of MX-80.

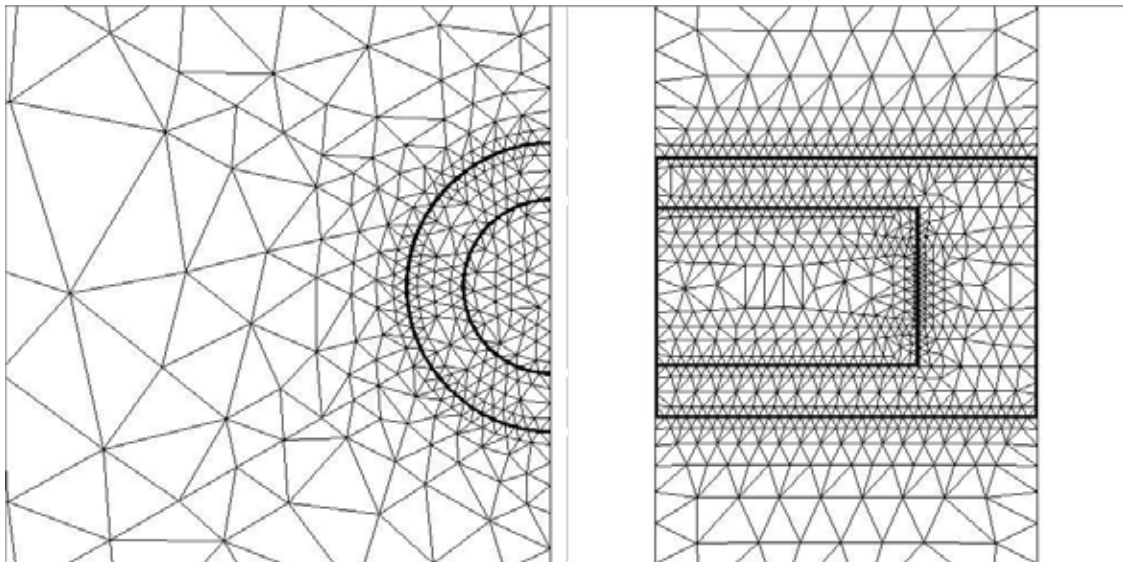


Figure 3.2: Close-ups of the 3D element mesh at xy-plane (left) and at zy-plane (right).

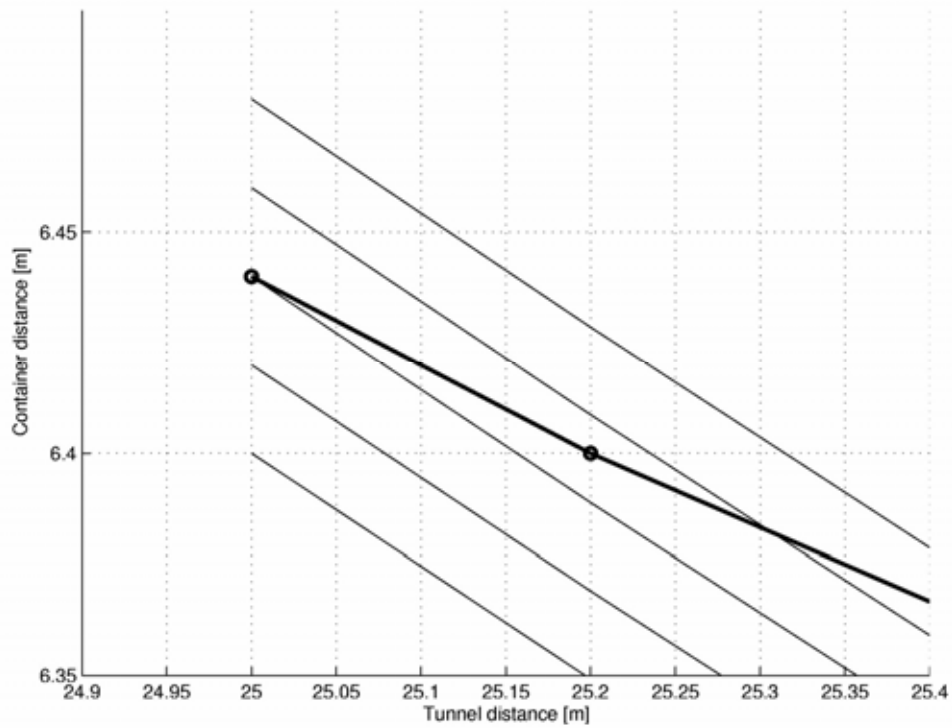
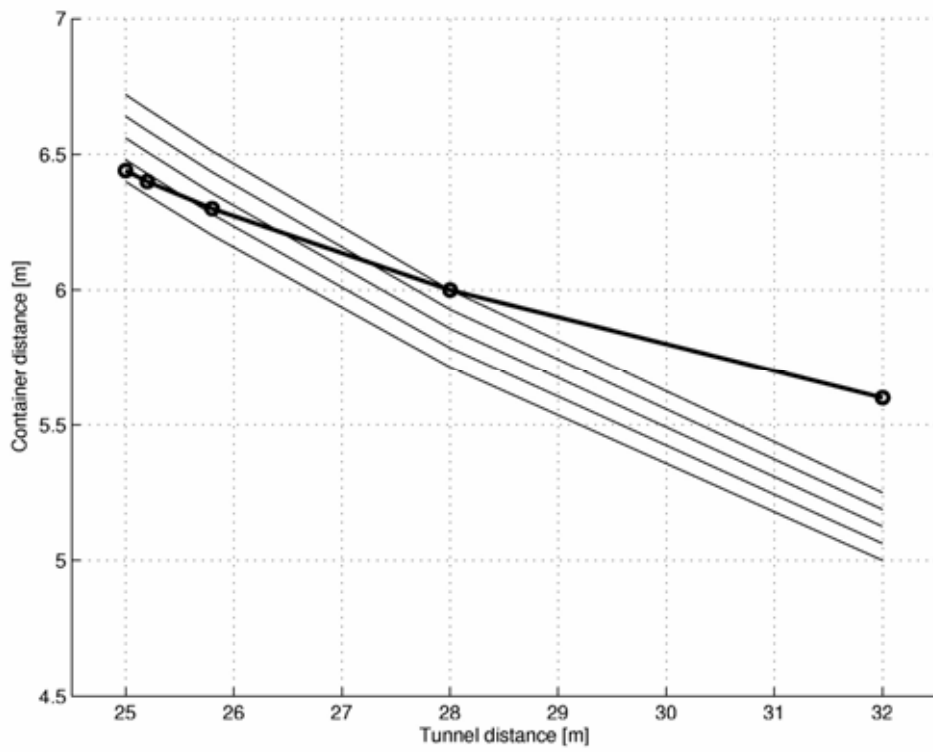


Figure 3.3: The combinations of tunnel (top) and container (bottom) distances that meet the criterion of 100 °C along with curves of constant area.

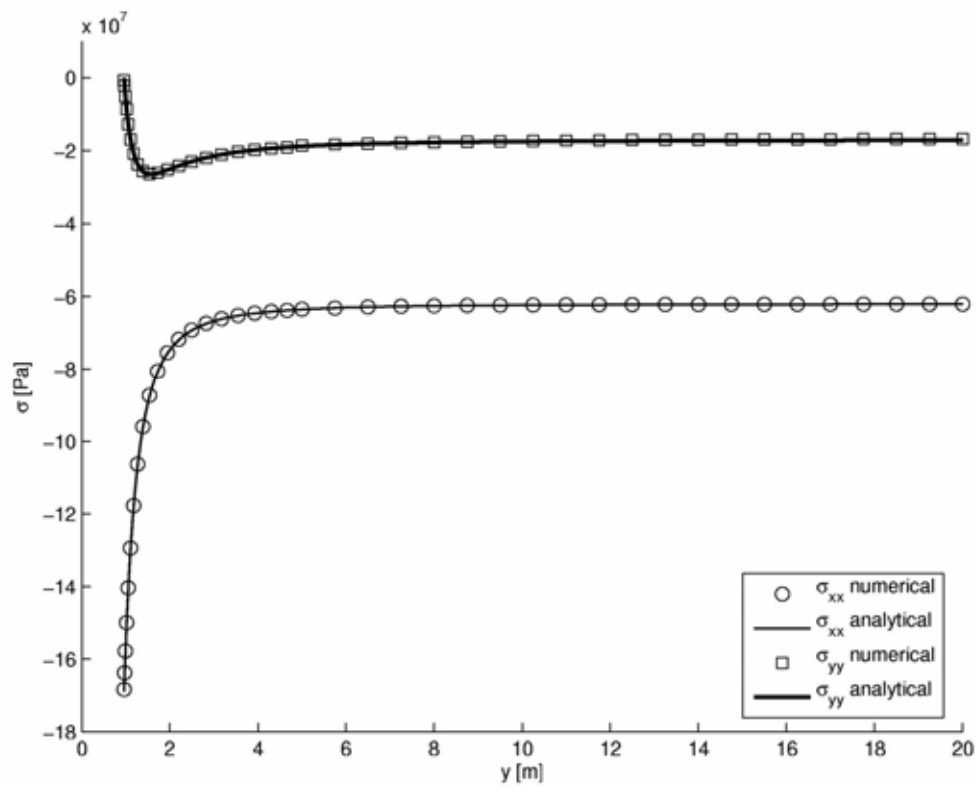
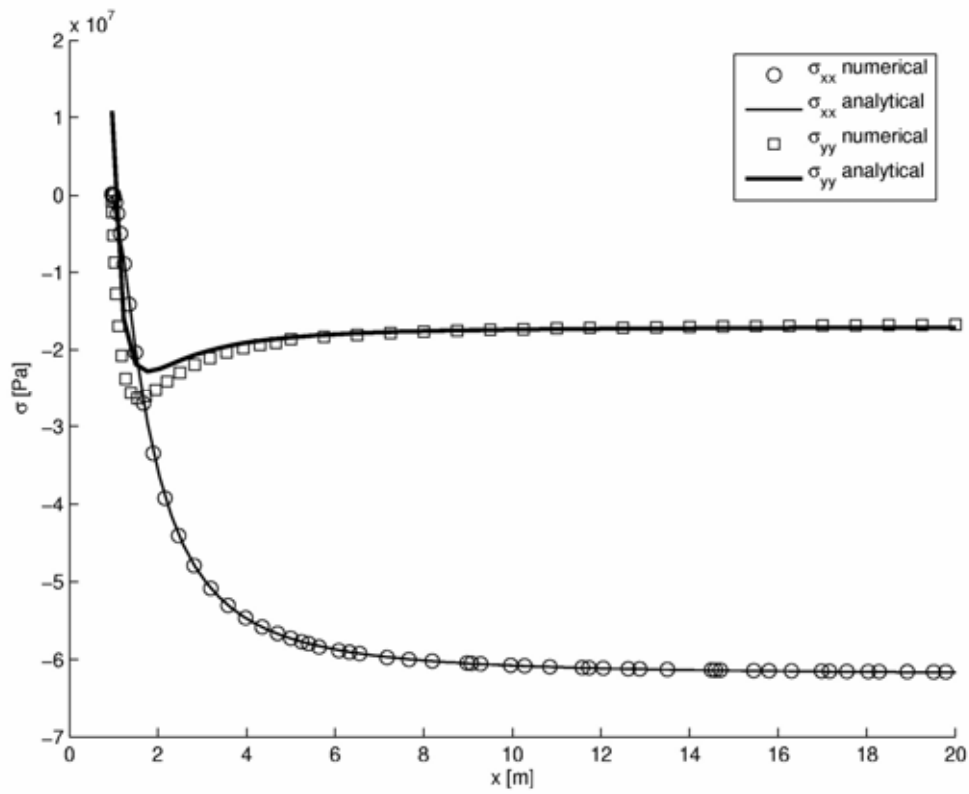


Figure 3.4: Comparison of the numerical and analytical solutions for 2D stresses along x-axis (top) and along y-axis (bottom).

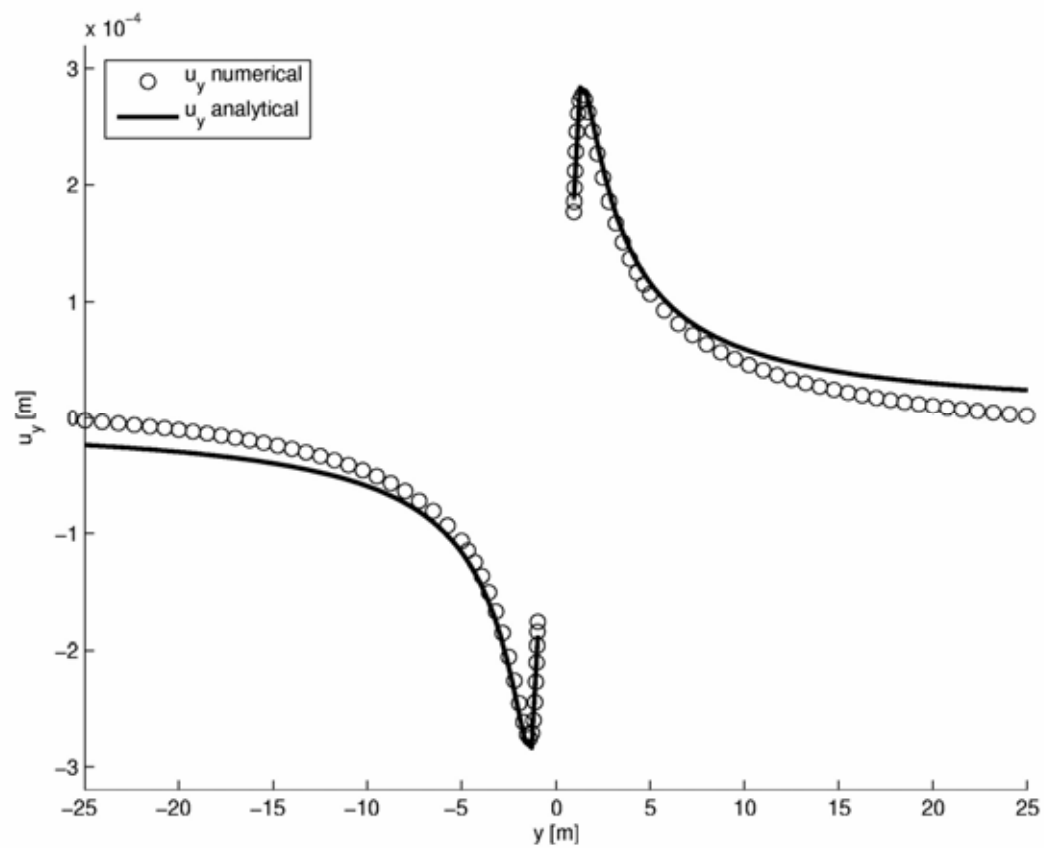
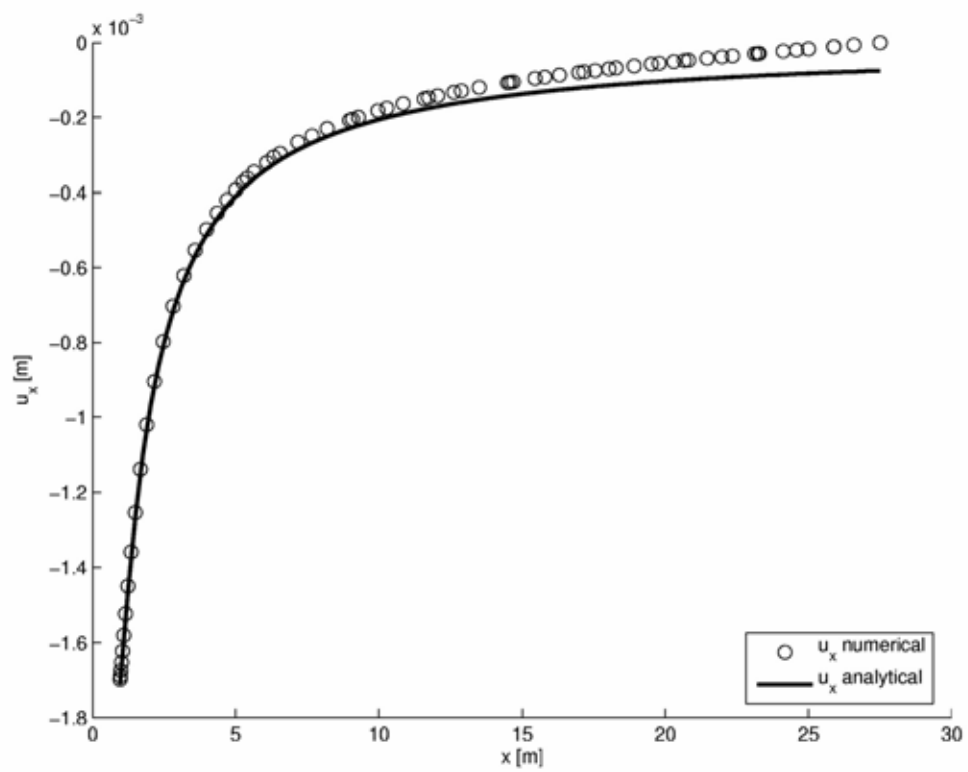


Figure 3.5: Comparison of the numerical and analytical solutions for 2D radial displacements along x -axis (top) and along y -axis (bottom).

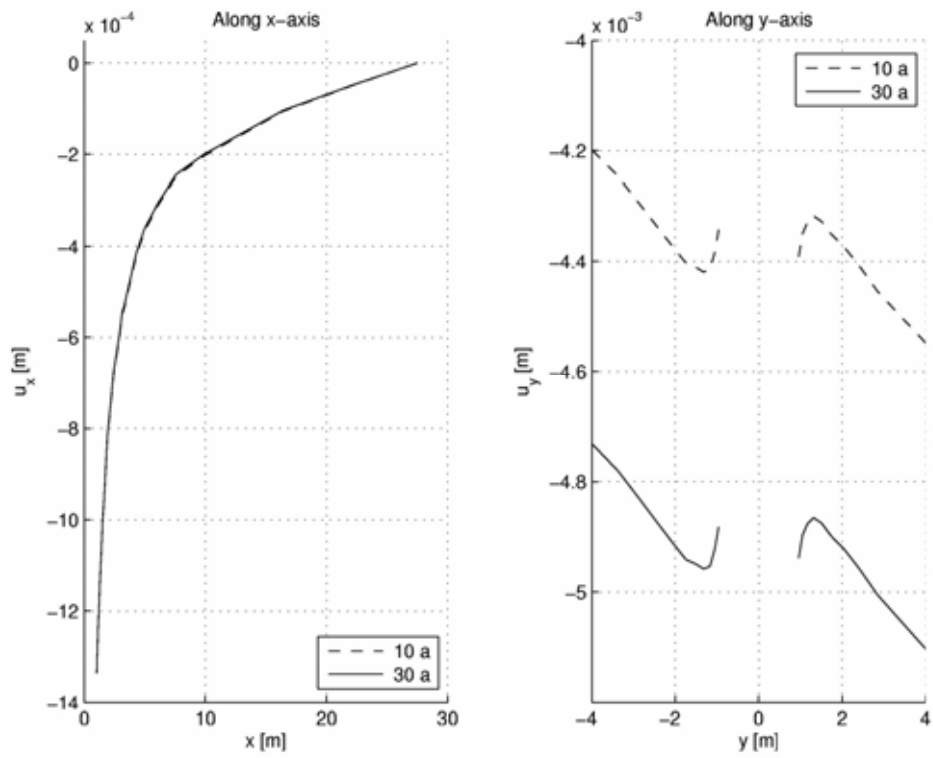


Figure 3.6: Horizontal displacement along x-axis and vertical displacement along y-axis in rock at 10 and 30 years.

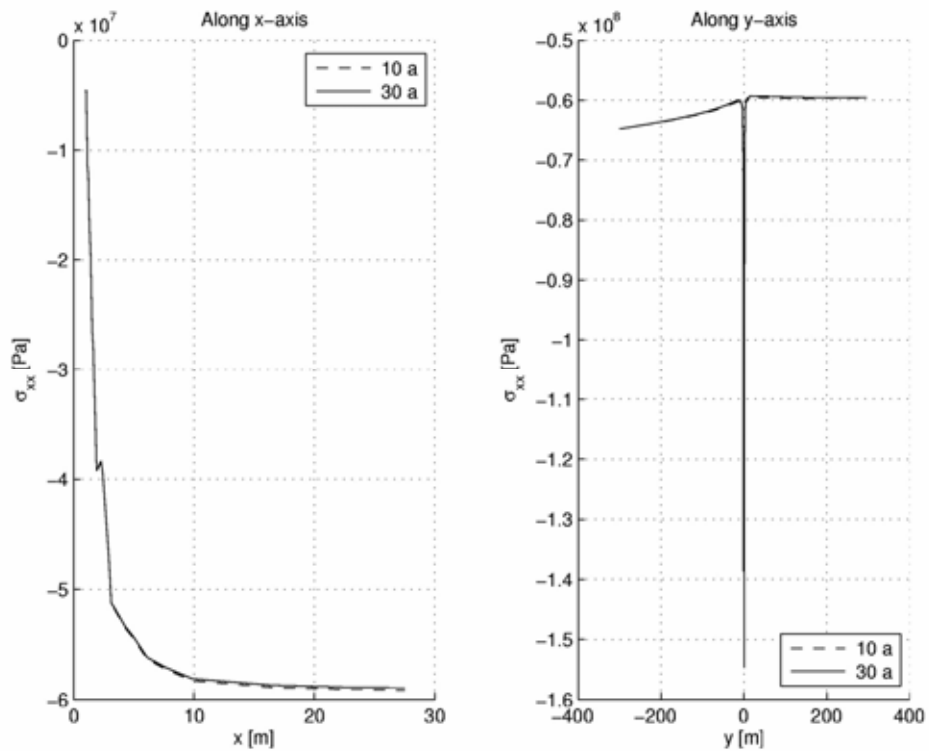


Figure 3.7: Major principal stress profiles in rock at 10 and 30 years.

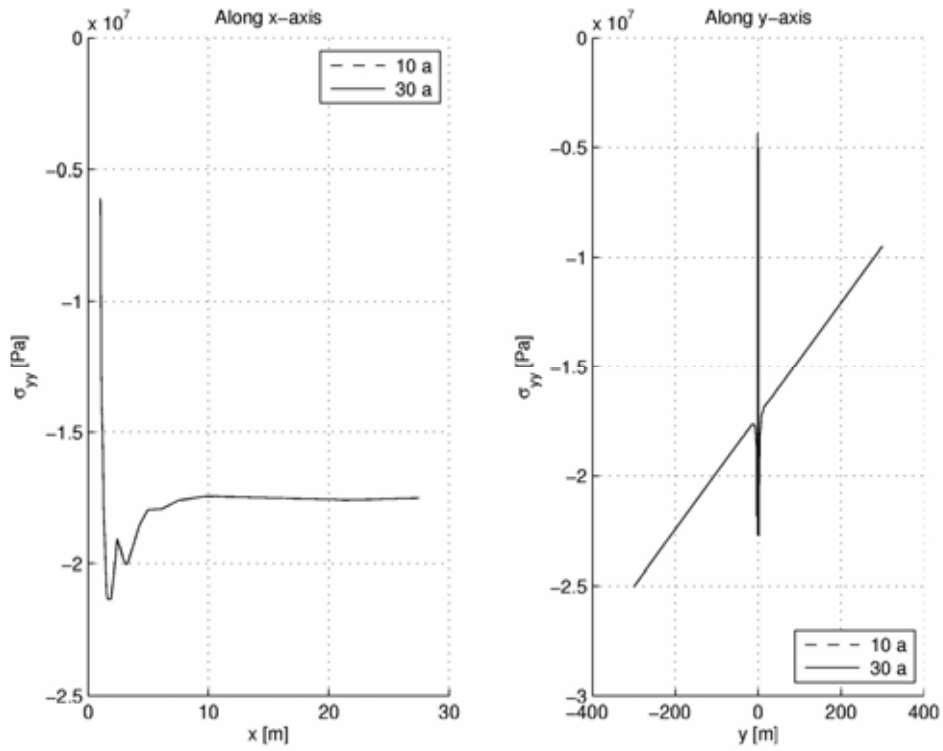


Figure 3.8: Minor principal stress profiles in rock at 10 and 30 years.

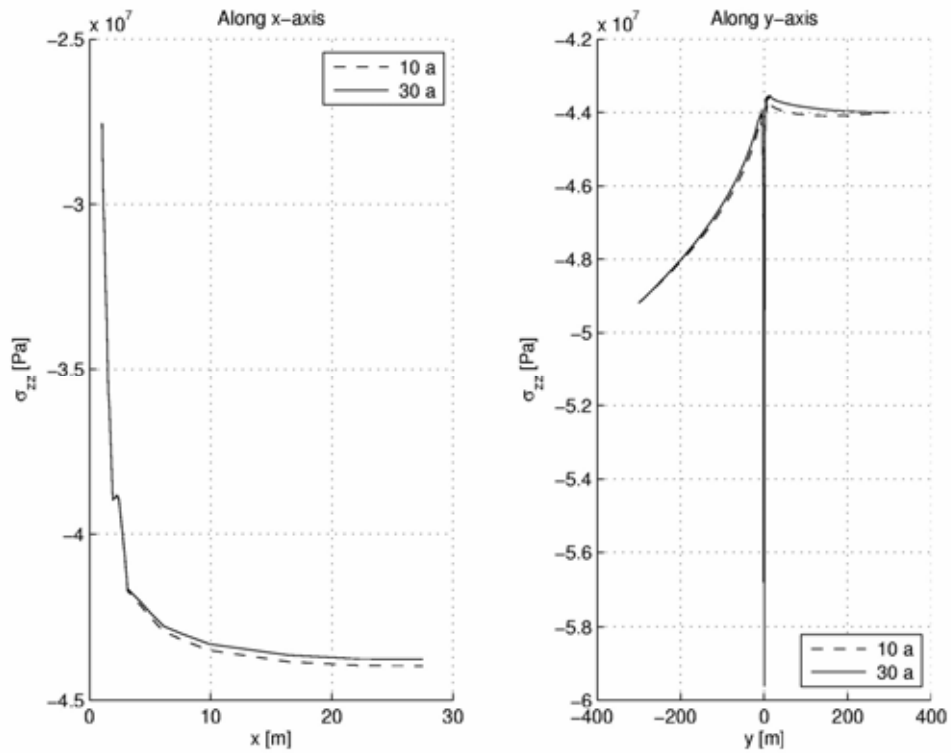


Figure 3.9: Intermediate principal stress profiles in rock at 10 and 30 years.

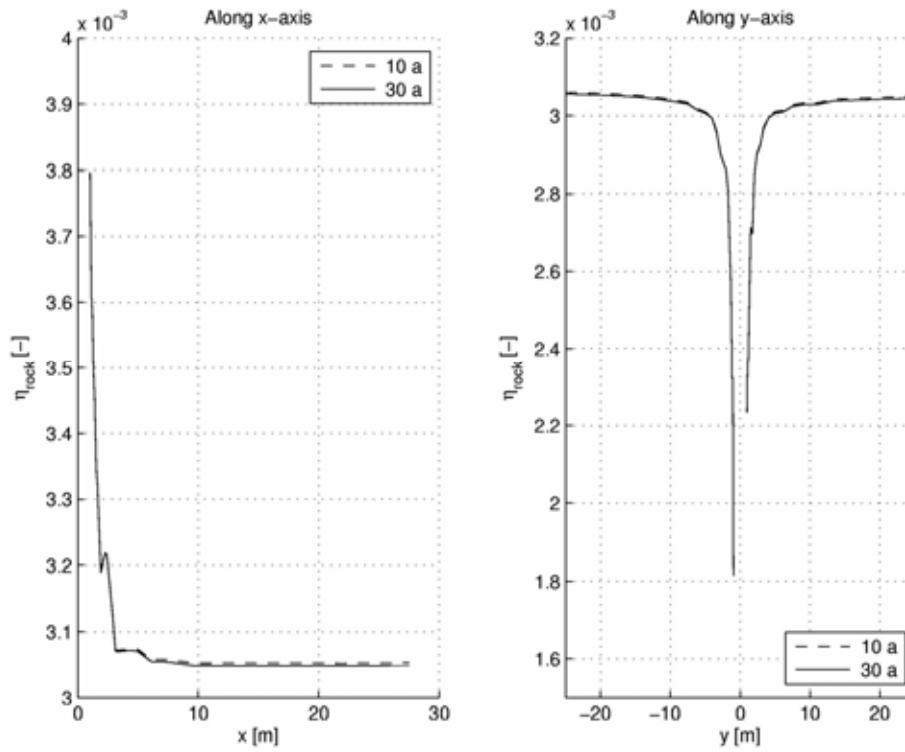


Figure 3.10: Porosity profiles in rock at 10 and 30 years.

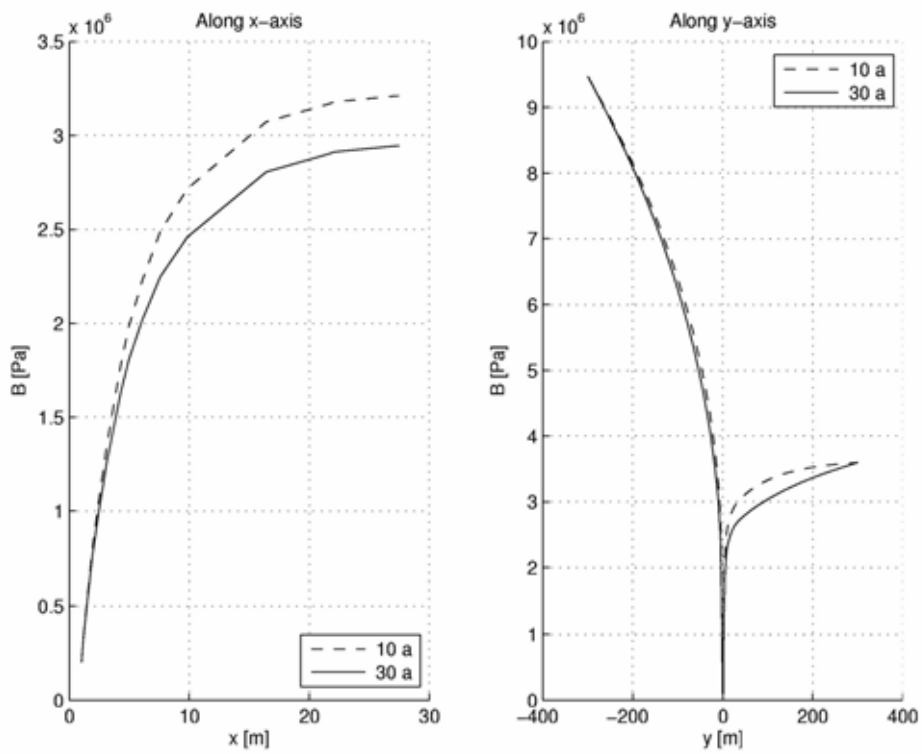


Figure 3.11: Pore pressure profiles in rock at 10 and 30 years.

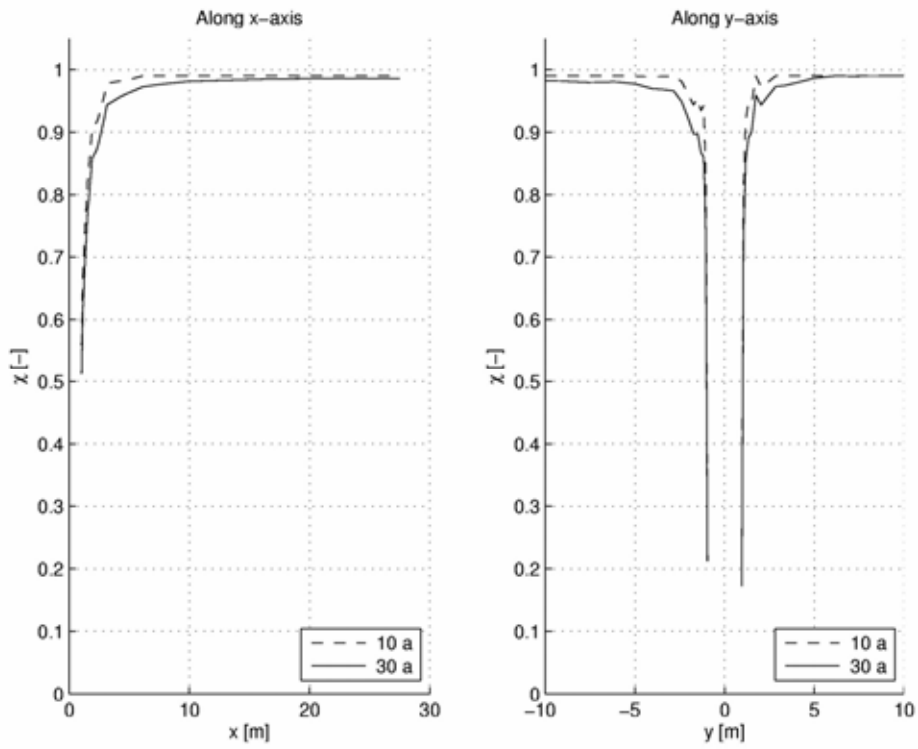


Figure 3.12: Saturation degree profiles in rock at 10 and 30 years.

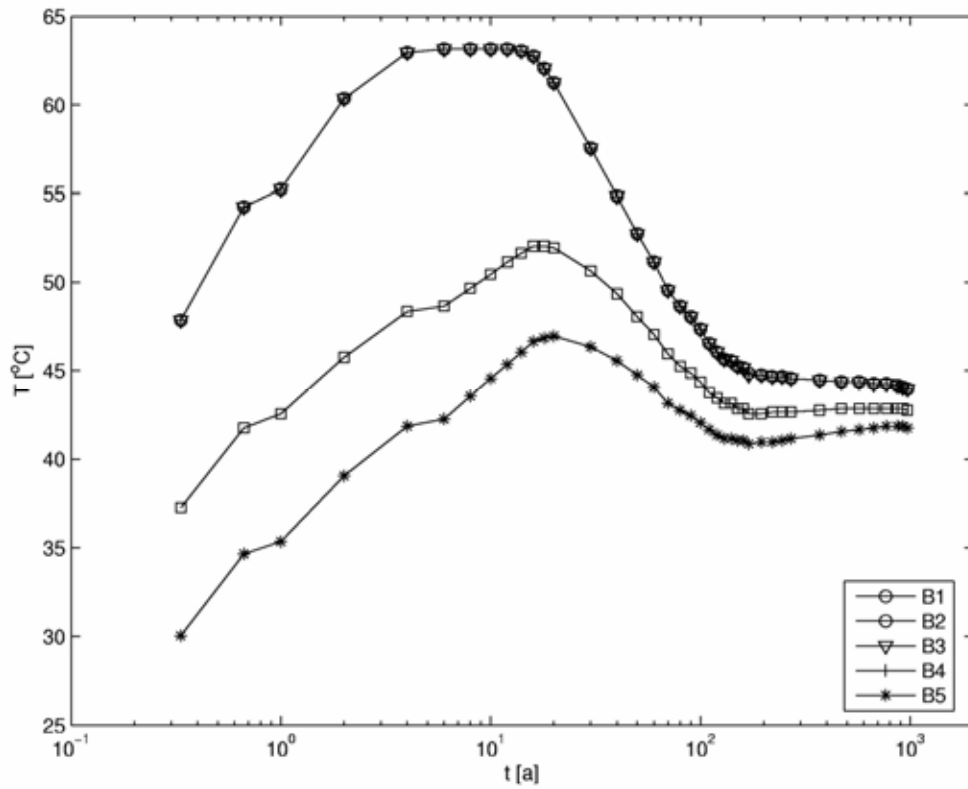


Figure 3.13a: Evolution of temperature in selected points in the buffer after emplacement.

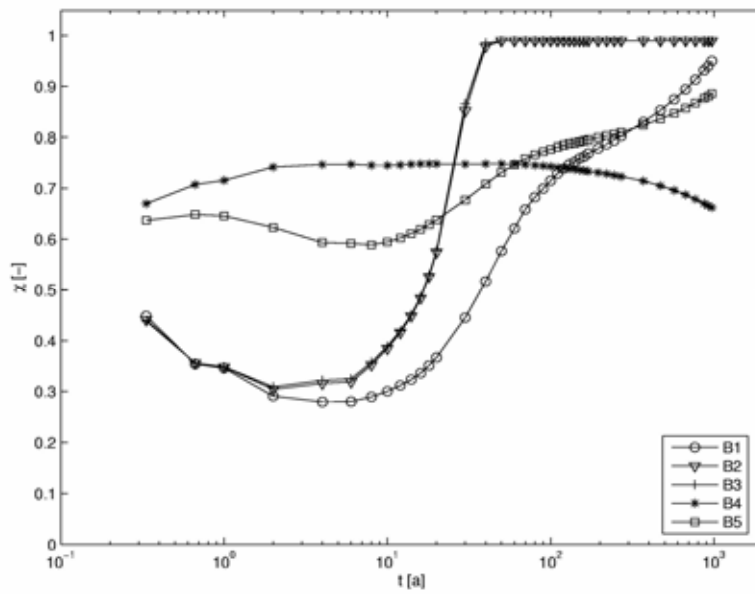


Figure 3.13b: Evolution of saturation degree in selected points in the buffer after emplacement.

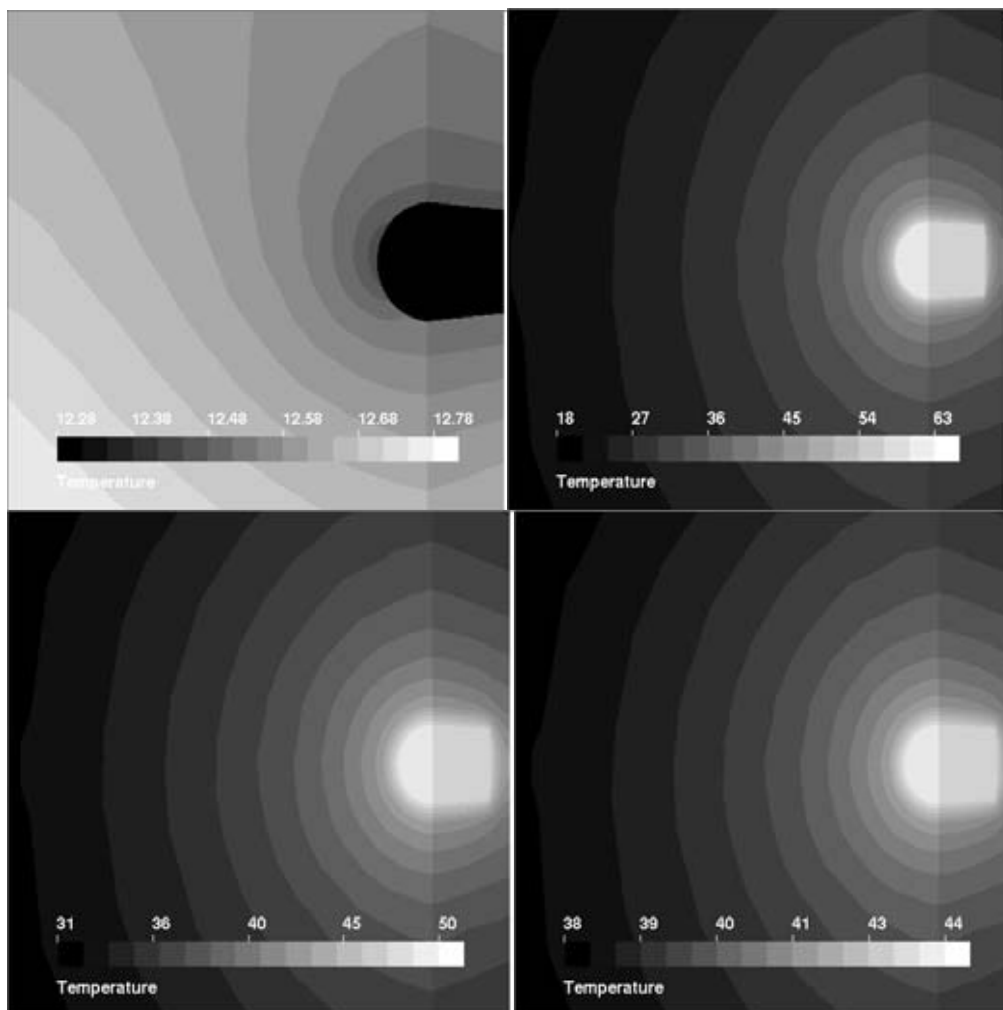


Figure 3.14: Temperature [$^{\circ}\text{C}$] in rock at 30, 38, 100, and 1000 years. 38 years is the time at which the temperature is the maximum.

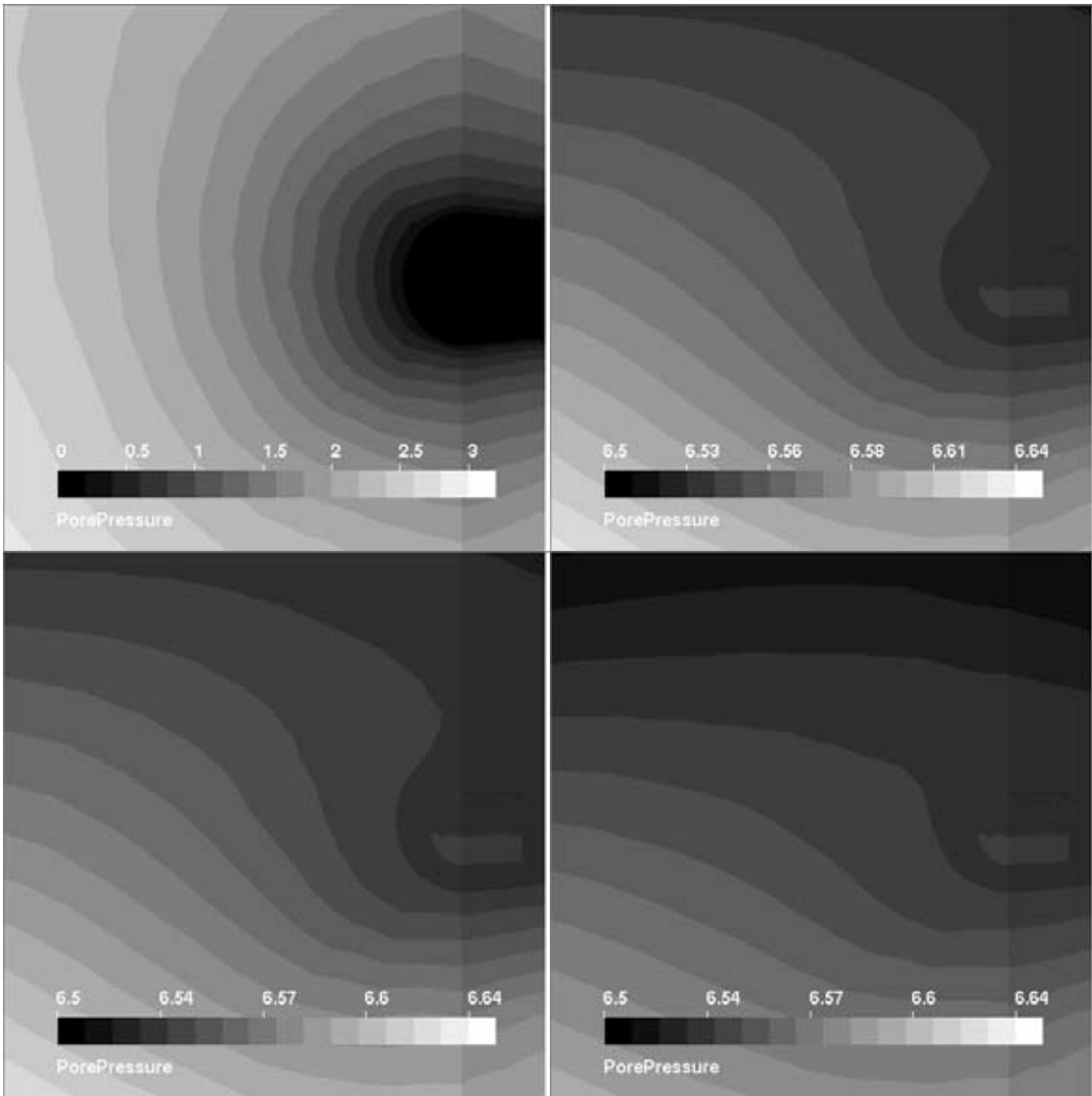


Figure 3.15: Pore pressure [MPa] in rock at 30, 38, 100, and 1000 years. 38 years is the time at which the temperature is the maximum.

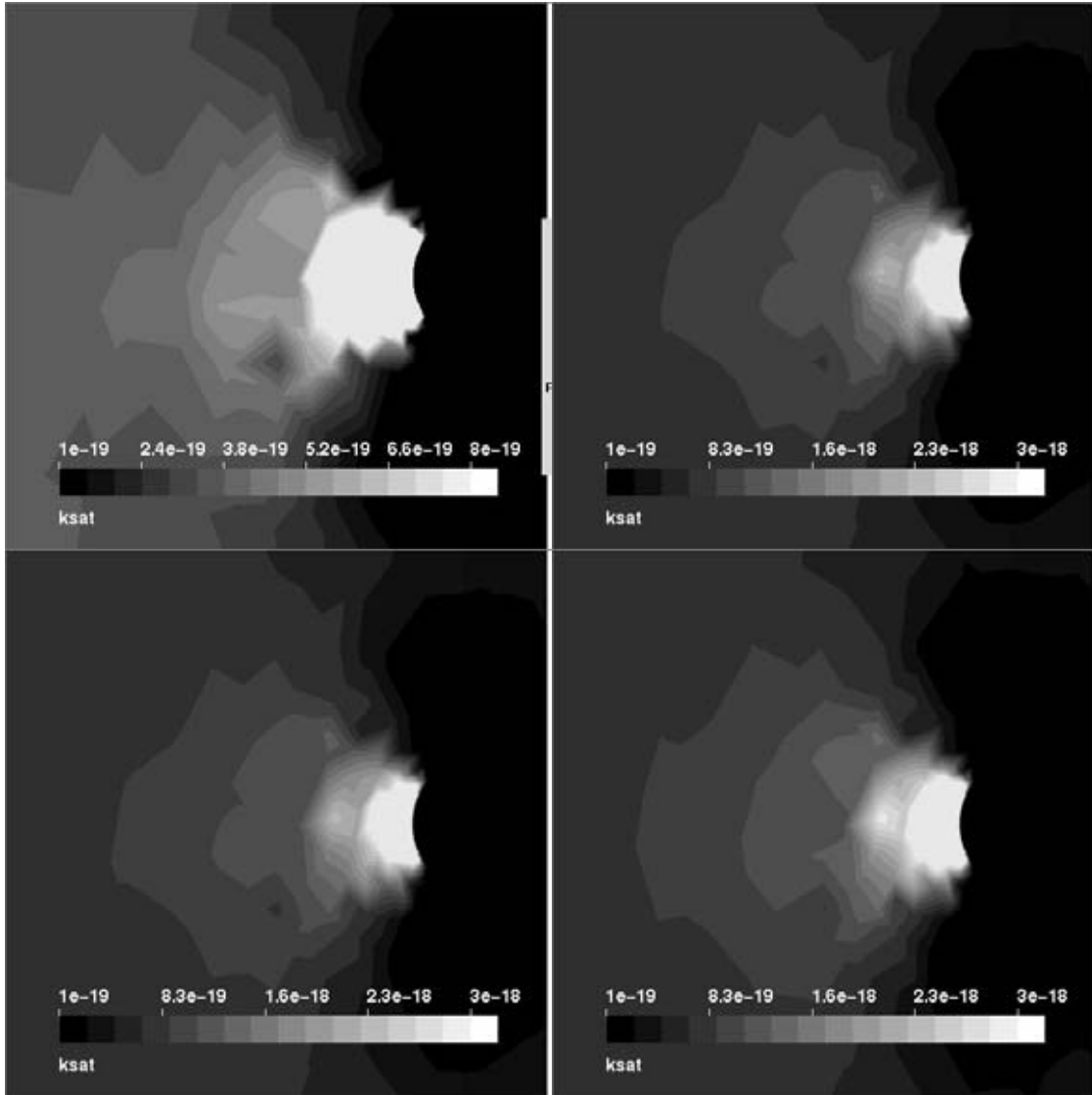


Figure 3.16: Rock permeability [m^2] at 30, 38, 100, and 1000 years. 38 years is the time at which the temperature is the maximum.

4. SKI/LBNL's modeling of Task A-1 using ROCMAS

Jonny Rutqvist, Lawrence Berkeley National Laboratory, USA

4.1 Introduction

The objective of Task A of DECOVALEX-THMC is to assess the implications of coupled THM processes in the near field of a typical repository on long-term repository performance. This is intended replicate an actual working example where the engineering experts would work in collaboration and interact with performance/safety analysts and experimentalists on a realistic case study of a repository. The proposed work is an example of integration of model development/calibration and interpretation of laboratory and in-situ data towards the final goal of building confidence to the PA process. Several Research Teams within the DECOVALEX-THMC will analyze the problem using various conceptual and numerical approaches. The repository we consider is a hypothetical repository in crystalline rocks. The geological setting, the physical characteristics of the spent fuel, engineered barriers and host rock, as well as the geometrical configuration of the repository are given detailed in Chapter 1.

This chapter presents the modeling results by the SKI/LBNL Research Team for subtask A1, which consists of preliminary simplified modeling of the THM behavior in the near field of the repository. In subtask A1, a linear elastic medium is considered without influences of mechanically induced changes in permeability (e.g. induced by rock damage). Rock damage in the excavation disturbed zone (EDZ) and its effect on permeability and THM evolution will be considered in later stages of Task A.

In this chapter, we first provide a description of the numerical model, including the code, finite element discretization and material properties, modeling sequence and boundary conditions. Thereafter we present the results of the numerical analysis followed by conclusions for SKI/LBNL's work on Task A1.

4.2 Description of the ROCMAS code

The SKI/KTH team is using a continuum approach with the finite element program ROCMAS (Noorishad and Tsang, 1999; Rutqvist et al., 2001a). It is continuum based, capable of modeling porous soil and ubiquitously fractured rock, and with the option for representing discrete fractures. The code was used in DECOVALEX II and III for the prediction of the THM behavior in bentonite and fractured rock during a heater tests conducted at Kamaishi Mine in Japan (Rutqvist et al, 2001b), and at Grimsel test site (Rutqvist and Tsang 2004). The code was also used in DECOVALEX III for modeling of BMT1, which was a scoping calculation to investigate the implication of coupled THM processes on the near-field performance of a typical multiple barriers nuclear waste repository (Rutqvist and Tsang 2005).

The following subsections described the code in terms of basic approach and assumptions, balance equations, constitutive equations and constraints, and field equations and solution approach.

4.2.1 Basic approach and assumptions

In ROCMAS, the formulation of coupled thermohydroelasticity in terms of Biot's theory of consolidation (Biot, 1941) is extended to partially saturated media through Philip and de Vries' (1957) theory for heat and moisture flow in soil. In this theory, three phases, solid, liquid, and gas, are present. However, it is assumed that the gas pressure P_g is constant and equal to atmospheric pressure throughout the porous medium. As a consequence, vapor transport occurs only through molecular diffusion driven by a gradient in vapor concentration (density), while advection of vapor with bulk gas flow is neglected. The vapor density in the medium is governed by Kelvin's relation, assuming thermodynamic equilibrium for pore liquid in contact with its vapor, and phase transition occur as evaporation-condensation processes. During heat transfer, coexisting fluid and solid components are assumed to be in local thermal equilibrium (i.e. locally they are at the same temperature).

The mechanical behavior of the porous media consists of the gas, liquid and solid-matter responses to local pressure and the overall material (skeleton) response to effective stresses. Fractures are treated as a "porous medium" separate from the rock matrix and would be discretely defined by special fracture elements in a finite-element mesh. Therefore, the basic balance equations are the same for rock matrix and fracture materials, while some of the constitutive relations differ. With this approach and these assumptions, three balance equations—water mass balance, energy conservation and linear momentum balance—and a number of constitutive relations are required for a full description of the THM state. These equations are derived and presented in details below.

4.2.2 General Balance Equations

The water mass balance equation for the coupled hydraulic and mechanical system is obtained by combining water mass balance equations (for water vapor and liquid water) with the solid mass balance equation. Considering the grain compressibility, but neglecting a few small terms related to the grain density changes caused by internal fluid pressure and temperature, the following coupled water mass balance equation is derived (Rutqvist *et al.*, 2001a):

$$\phi \frac{\partial}{\partial t} (S_l \rho_l + S_g \rho_v) + (S_l \rho_l + S_g \rho_v) \alpha \frac{\partial \varepsilon_v}{\partial t} = -\nabla \cdot (\mathbf{q}_{rl} + \mathbf{q}_{rv}) \quad (4.1)$$

where ϕ is porosity, S_l and S_g are liquid and gas saturation, ρ_l and ρ_v are liquid water and vapor densities, α is Biot's effective stress parameter, ε_v is volumetric strain, and \mathbf{q}_{rl} and \mathbf{q}_{rv} are flux densities for liquid and vapor flow.

Assembling the contributions to energy storage and heat flow over all phases results in the following form of the energy conservation equation (Rutqvist *et al.*, 2001a)

$$\frac{\partial}{\partial t} [(1-\phi) \rho_s h_s + \phi (h_l S_l \rho_l + h_v S_g \rho_v)] = -\nabla \cdot (\mathbf{i}_m^h + h_l \mathbf{q}_{rl} + h_v \mathbf{q}_{rv}) \quad (4.2)$$

where the storage content in the gas phase is dominated by the vapor, and mechanical energy conversion is neglected. In Eq. (4.2) h_s , h_l , and h_v are specific enthalpies (per unit mass of the phase), and \mathbf{i}_m^h is the apparent heat conduction over all phases.

The final balance equation is the law of conservation of linear momentum, which in the absence of an inertia term reduces to the static stress equilibrium for macroscopic total stresses:

$$\nabla \cdot \boldsymbol{\sigma} + \rho_m \mathbf{g} = 0 \quad (4.3)$$

where $\boldsymbol{\sigma}$ is the total stress tensor, \mathbf{g} is a vector for the acceleration resulting from gravity, and ρ_m is the average density of the mixture:

$$\rho_m = (1 - \phi)\rho_s + \phi S_l \rho_l + \phi S_g \rho_g \quad (4.4)$$

Hence, neglecting the air mass balance, Eqs (4.1) to (4.3) are the basic balance equations in ROCMAS.

4.2.3 Constitutive equations and constraints

Neglecting the effects of osmotic suction and adsorbed liquid water, the liquid saturation S_l is assumed to be a function of capillary pressure P_c and temperature, and following relations apply

$$S_l = S_l(P_c, T) \quad (4.5)$$

$$P_c = P_g - P_l \quad (4.6)$$

$$S_g = 1 - S_l \quad (4.7)$$

where P_l is liquid water pressure, P_g is total gas pressure, and S_g is gas saturation. With the assumption of atmospheric gas pressure (and thus $P_l \approx -P_c$), the liquid water and vapor flux is obtained as:

$$\mathbf{q}_{rl} = -\rho_l \frac{\mathbf{k}k_{rl}}{\mu_l} (\nabla P_l - \rho_l g \nabla z) \quad (4.8)$$

and

$$\mathbf{q}_{rv} = -D_v \mathbf{I} \nabla \rho_v \quad (4.9)$$

which has been derived assuming that ρ_g is constant. Assuming a local thermodynamic equilibrium between liquid water and its vapor, the vapor density can be obtained through Kelvin's relationship for relative humidity, r_H , of the moist air in a porous media (Bear and Bachmat, 1991) as

$$\rho_v = \rho_{vs}(T) RH = \rho_{vs} \exp\left(\frac{P_l}{\rho_l R_v T}\right) \quad (4.10)$$

where ρ_{vS} is the temperature-dependent saturated vapor density and R_v is the specific gas constant for water vapor. The vapor gradient in Eq. (4.9) is further expanded using Eq. (4.10), leading to the following expression for the vapor flux:

$$\mathbf{q}_{rv} = -\rho_l (D_{Pv} \mathbf{I} \nabla P_l + D_{Tv} \mathbf{I} \nabla T) \quad (4.11)$$

where

$$D_{Pv} = \frac{D_v \rho_v}{\rho_l^2 R_v T} \quad (4.12)$$

is the isothermal vapor diffusivity, and

$$D_{Tv} = f_{Tv} D_v \left(\frac{RH}{\rho_l} \frac{\partial \rho_{vS}}{\partial t} - \frac{\rho_v P_l}{\rho_l^2 R_v T^2} \right) \quad (4.13)$$

is the thermal vapor diffusivity.

All the parameters in Eqs (4.12) and (4.13) are known from other constitutive relations except for f_{Tv} , a thermal diffusion enhancement factor (Philip and de Vries, 1957), and the effective molecular diffusion coefficient, D_v , which should be experimentally determined. The effective molecular diffusion coefficient is calculated using an empirical relation for molecular diffusion of water vapor and reduction factors taking into account the porous media properties, using the following expression:

$$D_v = \tau S_g \phi 2.16 \times 10^{-5} (T_{abs}/273.15)^{1.8} \quad (4.14)$$

where τ is a tortuosity factor.

The permeability of a porous soil depends on its porosity and an empirical relative permeability function as

$$\mathbf{k} = \mathbf{k}(\phi) \cdot k_r(S_l) \quad (4.15)$$

where $\mathbf{k}(\phi)$ is the hydraulic permeability tensor of the porous media (in soil literature denoted as *intrinsic permeability*) and k_r is the relative permeability function for liquid and flow. For a fractured rock, the hydraulic permeability may be dominated flow in the fracture system and related to stress or strain, rather than porosity, thus

$$\mathbf{k}(\phi) = \mathbf{k}(\boldsymbol{\sigma}', \boldsymbol{\varepsilon})$$

Heat conduction is governed by Fourier's law, which is written as

$$\mathbf{i}_m^h = -\lambda_m \mathbf{I} \nabla T \quad (4.16)$$

where λ_m is the apparent macroscopic thermal conductivity over all phases, which in a porous material may be strongly dependent on liquid water content.

The thermal properties of the porous media in the formulation of ROCMAS are derived based on the work by de Vries (1958). The specific enthalpies in Eq. (4.2) is expressed in terms of specific heat and temperature as:

$$h_s + h_l = C_s(T - T_0) + C_l(T - T_0) \quad (4.17)$$

$$h_v = h_{pv} + h_{L0} = C_{pv}(T - T_0) + L_0(T_0) = C_{pl}(T - T_0) + L(T) \quad (4.18)$$

where L_0 is the latent heat of vaporization of liquid water at T_0 .

The total energy flux in Eq. (4.2) is then written as:

$$\mathbf{q}_h = -\lambda \mathbf{I} \nabla T + C_{pl}(T - T_0) \mathbf{q}_{rl} + [C_{pl}(T - T_0) + L(T)] \mathbf{q}_{rv} \quad (4.19)$$

where the first term represents pure conduction, and second and third terms are enthalpy transport by liquid and vapor flow, respectively. Following de Vries (1958, 1987), we substitute Eq. (4.11) into Eq. (4.19) to derive the following expression:

$$\mathbf{q}_h = -(\lambda + \rho_l LD_{Tv}) \mathbf{I} \nabla T - \rho_l LD_{pv} \mathbf{I} \nabla P + C_{pl}(\mathbf{q}_{rl} + \mathbf{q}_{rv})(T - T_0) \quad (4.20)$$

In practice, the conductivity of the porous media may be experimentally determined as a function of saturation, including the effects of pure conduction and latent heat transport under thermal gradient:

$$\lambda + \rho_l LD_{Tv} = \lambda_m(S_l) \quad (4.21)$$

With the basic assumption of small strain, the total strain tensor, $\boldsymbol{\varepsilon}$, and volumetric strain, ε_v , is defined as usual:

$$\boldsymbol{\varepsilon} = \frac{1}{2}(\nabla \mathbf{u} + (\nabla \mathbf{u})^{\text{tr}}) \quad \text{and} \quad \varepsilon_v = \nabla \cdot \mathbf{u} \quad (4.22)$$

where \mathbf{u} is the displacement vector and tr denotes the transpose of the tensor.

A modified effective stress law effective stress law can be derived in terms of Biot's parameters as:

$$d\boldsymbol{\sigma} = d\boldsymbol{\sigma}' - \alpha \mathbf{I} S_l dP \quad (4.23)$$

where the average pore pressure is calculated using the volume average of each phase and assuming a negligible gas pressure. The mechanical constitutive behavior of expressed as

$$d\boldsymbol{\sigma} = \mathbf{D} : (d\boldsymbol{\varepsilon} - d\boldsymbol{\varepsilon}_T - d\boldsymbol{\varepsilon}_{sw}) = \mathbf{D} : (d\boldsymbol{\varepsilon} - \mathbf{I} \beta_T dT - \mathbf{I} \beta_{sw} dS_l) \quad (4.24)$$

where \mathbf{D} is the tangential stiffness matrix, $\boldsymbol{\varepsilon}$, $\boldsymbol{\varepsilon}_T$, $\boldsymbol{\varepsilon}_{sw}$ are tensor of total, thermal and swelling strains, respectively.

An alternative state surface model were implemented for analysis of the mechanical behavior of the unsaturated bentonite were implement in conjunction with the analysis

of the FEBEX in situ test during DECOVALEX-III (Rutqvist and Tsang, 2004). However, for the analysis of Task A we resort to a simplified linear moisture swelling model, since the emphasis of the Task A is on THM effects in the near field rock, with potential evolution of rock damage.

4.2.4 Field equations and solution approach

The final field equations are derived by substituting the flux terms and stress terms in Eqs (4.8), (4.11), (4.20), and (4.23), and the basic balance equations [Eqs (4.1), (4.2) and (4.3)], and expanding the storage terms in terms of primary variables. The three following governing equations—expressed in terms of strain, ϵ , fluid pressure, P , and temperature, T —are obtained:

$$C_{Pe} \frac{\partial \epsilon_V}{\partial t} + C_{PP} \frac{\partial P}{\partial t} + C_{PT} \frac{\partial T}{\partial t} + \nabla \cdot (\mathbf{K}_{PP} \nabla P) + \nabla \cdot (\mathbf{K}_{PT} \nabla T) = J_p \quad (4.25)$$

$$C_{TP} \frac{\partial P}{\partial t} + C_{TT} \frac{\partial T}{\partial t} + \nabla \cdot (\mathbf{K}_{TP} \nabla P) + \nabla \cdot (\mathbf{K}_{TT} \nabla T) + \mathbf{V}_{TT} \cdot \nabla T + J_T \quad (4.26)$$

$$\nabla \cdot \left(\mathbf{C}_{ee} \frac{\partial \epsilon}{\partial t} \right) + \nabla \cdot \left(\mathbf{C}_{eP} \frac{\partial P}{\partial t} \right) + \nabla \cdot \left(\mathbf{C}_{eT} \frac{\partial T}{\partial t} \right) = J_e \quad (4.27)$$

which are the fluid flow, heat transfer, and force balance equations, respectively.

The final governing equations [Eqs (4.25) to (4.27)] are discretized using a standard Galerkin finite element solution approach to obtain a set of matrix equations as

$$\begin{bmatrix} \mathbf{0} & \mathbf{0} & \mathbf{0} \\ \mathbf{0} & \overline{\mathbf{K}}_{PP} & \overline{\mathbf{K}}_{PT} \\ \mathbf{0} & \overline{\mathbf{K}}_{TP} & \overline{\mathbf{K}}_{TT} \end{bmatrix} \begin{Bmatrix} \overline{\mathbf{u}} \\ \overline{\mathbf{P}} \\ \overline{\mathbf{T}} \end{Bmatrix} + \begin{bmatrix} \overline{\mathbf{C}}_{uu} & \overline{\mathbf{C}}_{uP} & \overline{\mathbf{C}}_{uT} \\ \overline{\mathbf{C}}_{Pu} & \overline{\mathbf{C}}_{PP} & \overline{\mathbf{C}}_{PT} \\ \mathbf{0} & \overline{\mathbf{C}}_{TP} & \overline{\mathbf{C}}_{TT} \end{bmatrix} \frac{\partial}{\partial t} \begin{Bmatrix} \overline{\mathbf{u}} \\ \overline{\mathbf{P}} \\ \overline{\mathbf{T}} \end{Bmatrix} = \begin{Bmatrix} \overline{\mathbf{J}}_u \\ \overline{\mathbf{J}}_P \\ \overline{\mathbf{J}}_T \end{Bmatrix} \quad (4.28)$$

where coefficient matrices, $\overline{\mathbf{K}}_{PP}$ etc, contains appropriate finite-element shape functions and transformation matrices (see Noorishad and Tsang (1996)), and $\overline{\mathbf{u}}$, $\overline{\mathbf{P}}$ and $\overline{\mathbf{T}}$ are nodal parameters.

The discrete equations are integrated in time from t to $t + \Delta t$ using a finite difference scheme. However, because many practical problems have a large time-constant difference between the fluid-flow equation and the heat equation, we use an interlaced solution approach. In this method, the hydromechanical equations are solved directly first, and thereafter, the heat equation is solved for an appropriate time step. After time integration, the Jacobian is derived in a Newton-Raphson or modified Newton-Raphson formulation, and the linearized equations are solved with a direct solver.

4.3 FEM mesh and material properties

Because of repetitive symmetry the simulation can be conducted on a one-quarter symmetric model containing one deposition hole (Figure 4.1 and 4.2). The quarter symmetric geometry represents a condition that neighboring deposition holes are simultaneously excavated and heated. The upper and lower boundaries are placed at vertical distances of 675 meters from the drift floor, with the upper boundary coinciding with the ground surface.

The material properties of buffer, rock mass, waste container and groundwater are presented in Tables 4.1 to 4.4. The material properties for the bentonite buffer were extracted from Börgesson and Hernelind (1999) and represents MX-80 bentonite.

The water retention curve of the bentonite follows modified van-Genuchten function that was fitted to data of MX-80 bentonite by Börgesson and Hernelind (1999) (see Figure 4.3). The following equation provided a reasonable to be a good match to the experimental data of the bentonite:

$$S_l = 0.01 + (0.99) \left[1 + \left(s / 18 \cdot 10^6 \right)^{1.5} \right]^{-0.333} \left[1 - s / 400 \cdot 10^6 \right]^{1.5} \quad (4.29)$$

where s is suction ($= -P_c$ in this model).

A simplified linear swelling model is used to represent swelling and development of swelling stress in the bentonite buffer. In this model, the swelling stress is calculated as:

$$\Delta \sigma' = 3K\beta_{sw} \Delta S_l \quad (4.30)$$

To determine the change in stress for a given change in saturation we need to know the bulk modulus, K , and moisture swelling coefficient β_{sw} . In this study, we estimate these two parameter from experimental data for MX-80, presented in Borgesson and Hernelind (1990). First a moisture swelling coefficient of $\beta_{sw} \approx 0.4$ were determined by fitting to data from unconfined drying shrinkage test. Moreover, experimental data in Borgesson and Hernelind (1999) indicates a swelling stress of 6 to 8 MPa when a sample is wetted to full saturation from an initial saturation of 61%. With a target swelling stress of 8 MPa, a representative “average” bulk modulus for this linear model is calculated using Equation (4.30) as:

$$K = \frac{1}{3} \frac{\Delta \sigma'_m}{\Delta S_l} \frac{1}{\beta_{sw}} = \frac{1}{3} \frac{8 \cdot 10^6}{0.39} \frac{1}{0.4} \approx 17 \text{ MPa} \quad (4.31)$$

The approach of modeling swelling can be considered a rational engineering approach to simulate the evolution of swelling stress and strain during the resaturation of the buffer. It is sufficient in this case, because the DECOVALEX THMC Task A is focused on the THM induced damage evolution in the rock surrounding the bentonite. The thermal conductivity of the bentonite is saturation dependent and the following function was fitted to experimental data in Börgesson and Hernelind (1999):

$$\lambda = 0.3 \quad \text{for } S_l < 0.25 \quad (4.32a)$$

$$\lambda = 0.3 + (S_l - 0.25) * 1.8 \quad \text{for } S_l > 0.25 \text{ and } S_l < 0.8 \quad (4.32b)$$

$$\lambda = 1.3 \quad \text{for } S_l > 0.8 \quad (4.32c)$$

The following function due to Borgesson and Hernelind (1999) are used for the thermal vapor diffusion coefficient of the bentonite:

$$D_{Tv} = 0.7 \cdot 10^{-11} \quad \text{for } 0.3 < S_1 < 0.7 \quad (4.33a)$$

$$D_{Tv} = 0.7 \cdot 10^{-11} \cos^6 \left(\frac{S_1 - 0.7}{0.3} \frac{\pi}{2} \right) \quad \text{for } S_1 < 0.7 \quad (4.33b)$$

$$D_{Tv} = 0.7 \cdot 10^{-11} \sin^6 \left(\frac{S_1 - 0.3}{0.3} \frac{\pi}{2} \right) \quad \text{for } S_1 > 0.3 \quad (4.33c)$$

This function was developed and back-calculated by Borgesson and Hernelind (1999) by model simulations of vapor flow experiments under thermal gradient.

The permeability of the rock is about two orders of magnitude higher than that of the bentonite. Therefore, the resaturation of the bentonite would appear to be controlled by the hydraulic properties of the bentonite itself. However, significant desaturation of the rock may occur during the 30 year time period when the drift will be open at a relative humidity that might be less than 1.0. A water retention curve and relative permeability of the rock suggested by Thomas et al. (2002) is adopted in this simulation (See Figure 4.3). It is a Van-Genuchten model (van-Genuchten, 1980) with the parameters given in Table 4.2.

Figure 4.4 presents the water retention curves and the absolute permeability of buffer and rock. Because the relative permeability function assumed for the rock is more sensitive to changes in saturation, the absolute permeability of the rock may approach that of the bentonite if the rock is desaturated. Figure 4.4 shows that a 61% initial saturation in the buffers corresponds to a suction pressure of 33 MPa within the bentonite. If this suction pressure is applied to the rock wall the absolute permeability for liquid flow in the rock wall approaches the absolute permeability of the bentonite. Therefore, a desaturation of the rock may also occur immediately after the emplacement of the bentonite buffer.

4.4 Modeling sequences and boundary conditions

Figure 4.5 presents modeling sequence, boundary and initial conditions for a coupled THM simulation. The initial conditions for the rock mass is defined at the pre-excavation stage (Figure 4.5a). The temperature and in situ stress gradients were given in the Task definition (see Chapter 1). The excavation sequence is simulated for 30 years with the elements in the drift removed and with fixed relative humidity (Figure 4.5b). In the base case a relative humidity of 100% were used, whereas a case of a 50% relative humidity was simulated for comparison. After the 30 years excavation simulation is completed, the waste canister, bentonite buffer and back-fill are installed instantaneously and the post-closure simulation can start (Figure 4.5c and d). The post-closure simulation is conducted for 1 million years until the temperature and fluid pressure have been restored to ambient conditions. The condition of a relative humidity of 50% is simulated by applying a fluid pressure of -91 MPa at the drift wall (calculated from Kelvin's equation).

4.5 Analysis of mechanical rock mass failure

The mechanical integrity of the rock mass is estimated using Hoek and Brown's failure criterion, which can be written as (Hoek and Brown, 1997):

$$\sigma'_1 = \sigma'_3 + \sigma_{ci} \left(m_b \frac{\sigma'_3}{\sigma_{ci}} + s \right)^a \quad (4.34)$$

where σ'_1 and σ'_3 are the maximum and minimum effective stresses at failure respectively, m_b is the values of Hoek-Brown constant m for the rock mass, s and a are constants which depends upon the characteristics of rock mass, and σ_{ci} is the uniaxial compressive strength of the intact rock pieces. In the task description (Chapter 1) two sets of parameter are given:

Excavated drifts: $\sigma_{ci} = 100$ MPa, $m_b = 16.6$, $s = 1$ and $a = 0.5$

Post-emplacment drifts: $\sigma_{ci} = 150$ MPa, $m_b = 25.0$, $s = 1$ and $a = 0.5$

It was also decided that the failure criteria in Eq. (4.34) should be checked for Terzaghi effective stress ($\sigma' = \sigma + P$), rather than a Biot's effective stress.

4.6 Results of coupled THM analysis

This section present detailed results of the coupled THM modeling for both 100 and 50% in-drift relative humidity in the drift during the 30-year pre-closure period. The results are presented for the case of 100% in-drift relative humidity as a base case, whereas the case for 50% in-drift relative humidity is presented for comparison. The dependent results are presented for points usually located within the buffer or in the drift wall, close to the buffer. The location of points B1 and B4 can be found in Chapter 1.

4.6.1 Temperature evolution and maximum temperature

Figure 4.6 presents the decay function of heat power in the simulated waste canister and temperature evolution at two points in the buffer. Temperature contours at 1 and 10 years are presented in Figure 4.7. A maximum temperature of 60 °C is attained at the canister surface at about 2 years after waste emplacement. At the buffer/rock interface a maximum temperature of 49 °C is attained after 15 years. At 10,000 years, the heat power is down to a few percent of its initial values and the temperature has declined to about 32 °C, which is still substantially higher than the ambient temperature.

4.6.2 Evolution of buffer saturation and fluid pressure

Figure 4.8 and 4.9 presents the evolution and distribution of liquid saturation in the buffer. At the canister/buffer interface (Point B1), the liquid saturation first decreases to a minimum of about 46 % at about 1 year, and then starts to increase and finally reaches full saturation at about 12 years. However, in point B4, the full saturation is achieved after about 18 years. Thus, the time to full resaturation is about 18 years.

Figure 4.10 presents the evolution of fluid pressure at various points within the buffer and in the rock outside the buffer. Figure 4.10 a shows that fluid pressure near in the rock wall (“rock at the interface with bentonite”) becomes negative after emplacement indicating a desaturation of the rock around the drift. Figure 4.10b shows that this desaturation may extend as far a 10 meters from the drift. However, by the time for full saturation (about 18 years) the fluid pressure within the buffer and rock is almost equivalent. The fluid pressure then slowly increases with time and is not fully restored until after 2,000 years.

Figure 4.11 and 4.12 shows the effect of drift ventilation with 50% in-drift relative humidity on the evolution of liquid saturation and fluid pressure. The figures indicate that there is only a minor impact of the drift ventilation on the evolution of the saturation and fluid pressure during resaturation of the buffer. The numerical analysis shows that the drift ventilation would tend to dry-out the rock immediately around the tunnel, but the permeability in this dry-out zone would decrease by several orders of magnitude effectively preventing high inflow into the tunnel (See Figure 4.13). Thus, the desaturation of the does not extend very far from the drift during ventilation, and therefore the rock can be resaturated quickly after emplacement of the bentonite.

4.6.3 Evolution of stress in the buffer

Figure 4.14 presents the evolution of total stress within the buffer. A final total stress of about 15 MPa within the buffer depends on several components. First the bentonite swells as a result of the resaturation of the buffer. This swelling can give rise to a swelling stress of about 8 MPa (this was the calibrate target swelling stress used in Section 4.2). After the bentonite is fully saturated the fluid pressure increases from 0 to 6.6 MPa, which is the hydrostatic fluid pressure at 657 meters depth. Assuming Biot’s $\alpha = 1.0$ for the bentonite, a 6.6 MPa pressure increase could give rise to an increase in total stress of about 6.6 MPa. Thus the total stress developed from the swelling stress (which is an effective stress) and the fluid pressure is $8 + 6.6 = 14.6$ MPa. In addition to the stress created by resaturation and fluid pressure restoration, thermal expansion may give rise to additional small component of compressive stresses during elevated temperature.

4.6.4 Evolution of stress in the rock and possible failure

Figure 4.15 presents vertical profiles of horizontal stress in the rock. Thermal stress develops where temperature increases and peaks around 1,000 to 10,000 years. However, the thermal stresses are generally much smaller than the initial stresses in this case.

Figure 4.16 presents contours of minimum and maximum principal stresses at 1,000 years. Figure 4.16a shows that a zone of tensile stresses develops at the side wall of the drift. The direction of the tensile stresses is parallel to the drift wall and hence if the rock fails in tension, radial fractures could develop in this case. Figure 4.16b shows that there is high concentration of compressive stresses on the top and bottom of the drift with a maximum magnitude of -190 MPa (compressive stress).

Figure 4.17 presents the principal stress path in relation to the Hoek-Brown Failure envelopes defined in the problem definition. The initial effective principal stress (before excavation) is $\sigma'_1 = 56$ and $\sigma'_3 = 12$ MPa (where compressive stress is positive in this

case). After excavation, the maximum compressive stresses at the top of the drift increases to about 150 MPa, due to stress concentration near the drift wall. At the same time, a slight tensile stress is developed at the side wall. After emplacement, the both the minimum and maximum principal compressive stresses first increases because of the action of thermal stress, bentonite swelling stress, and restoration of fluid pressure. At the final stress stage after 10,000 years, a high tensile stress develops in the side wall. It is shown that the highest potential for rock failure occurs in the side wall, and that would likely create tensile fracturing. Such tensile fracturing could occur within 100 years after the emplacement.

4.7 Summary and conclusion

This coupled THM analysis was conducted using elastic rock properties and without any effects of stress on hydraulic properties. The following remarks and conclusions can be made based on this analysis:

- In this case the initial stresses are relatively high at the repository depth (657 m) compared with the induced thermal stresses.
- The analysis indicate only minor impact of drift ventilation (50% or 100% in-drift relative humidity during 30 years) on the resaturation process.
- Temperature peaks at about 60 °C at about 5 to 10 years after emplacement.
- The buffer becomes fully saturated in 10 to 20 years.
- Fluid pressure is restored to ambient after several thousand years.
- Maximum compressive stress is 190 MPa at about 1,000 years.
- Tensile failure develops at the side wall of the drift within 100 years after emplacement.

References

- Bear, J. and Bachmat, Y., *Introduction to Modeling of Transport Phenomena in Porous Media*. p. 553. Kluwer Academic Publisher, Netherlands. 1999.
- Biot, M.A., *General theory of three dimensional consolidation*. J. Applied Physics, 1941 (12), 155–164.
- Börgesson L. and Hernelind J. *Coupled thermo-hydro-mechanical calculations of the water saturation phase of a KBS-3 deposition hole*. Swedish Nuclear Fuel and Waste Management Co. Technical Report TR-99-41. 1999.
- de Vries, D.A, Simultaneous transfer of heat and moisture in porous media. *Trans. Am. Geophys. Un.* 39, 909–916 (1958).
- de Vries, D.A., *The theory of heat and moisture transfer in porous media revisited*. Int. J. Heat. Mass. Transfer., 1987(30), 1343–1350.
- Hoek E and Brown E. T. *Practical estimates of rock mass strength*. Int. J. Rock Mech. Min. Sci., 1997(34), 1165-1186.
- Noorishad, J., and Tsang, C.-F., *ROCMAS-simulator: A Thermohydromechanical Computer Code*. In Stephansson, O., Jing, L., and Tsang, C.-F. editors. Coupled

- Thermo-hydro-mechanical Processes of Fractured Media. Developments in Geotechnical Engineering, Elsevier. 79, pp. 551–558. 1996.
- Philip J.R. and de Vries D.A. *Moisture movement in porous material under temperature gradients*. EOS Trans., AGU, 1957;38(2): 222-232.
- Rutqvist J., Börgesson L., Chijimatsu M., Kobayashi A., Nguyen T. S., Jing L., Noorishad J., and Tsang C.-F. *Thermohydromechanics of Partially Saturated Geological Media – Governing Equations and Formulation of Four Finite Element Models*. Int. J. Rock mech. Min. Sci. 2001a(38),105-127.
- Rutqvist J., Börgesson L., Chijimatsu M., Nguyen T. S., Jing L., Noorishad J., and Tsang C.-F. *Coupled Thermo-hydro-mechanical Analysis of a Heater Test in Fractured Rock and Bentonite at Kamaishi Mine – Comparison of Field Results to Predictions of Four Finite Element Codes*. Int. J. Rock mech. Min. Sci., 2001b(38), 129-142.
- Rutqvist J. and Tsang C.-F. *A fully coupled three-dimensional THM analysis of the FEBEX in situ test with the ROCMAS code: prediction of THM behaviour in a bentonite barrier*. In: Stephansson O, Hudson JA, Jing L, editors. Coupled T-H-M-C Processes in Geo-Systems: Fundamentals, Modelling, Experiments and Applications. Elsevier Geo-Engineering Book Series, Oxford, p. 143–148. 2004.
- Rutqvist J., Chijimatsu M., Jing L., De Jonge J., Kohlmeier M., Millard A., Nguyen T.S., Rejeb A., Souley M., Sugita Y. and Tsang C.F. *Numerical study of the THM effects on the near-field safety of a hypothetical nuclear waste repository – BMT1 of the DECOVALEX III project. Part 3: Effects of THM coupling in fractured rock* Int. J. Rock mech. & Min. Sci., 2005(42), 745-755.
- Thomas, H.R., Cleall, P.J. and Mitchell, H.P. *Comparison of physical measurements and a finite element numerical simulation of water uptake and distribution in the isothermal test*. OPG report 0818-REP-01300-10042-R00, OPG, NWMD, 700 University Av. Toronto, Canada, M5G 1X6. 2002.

Table 4.1. Material Properties of Bentonite Buffer (MX-80 bentonite)

Parameter	Value	Source
Saturated permeability, k_{ws} [m^2]	$6.5 \cdot 10^{-21}$	Börgesson and Hernelind (1999)
Capillary pressure, P_c [Pa]	Equation (4.29)	Fitted to experimental data from Börgesson and Hernelind (1999)
Relative permeability, k_r [-]	$k_r = S^3$	Börgesson and Hernelind (1999)
Porosity, ϕ [-]	0.435	Börgesson and Hernelind (1999)
Bulk Modulus Modulus, K [MPa]	17	Back-calculated to fit swelling stress in Börgesson and Hernelind (1999)
Poisson ratio, ν [-]	0.3	Assumed
Biot's effective stress parameter, α [-]	0.0 ($P_1 < 0.0$) 1.0 ($P_1 \geq 0.0$)	Assumed
Moisture swelling coefficient, β_{sw} [-]	0.4	Fitted to drying test data in Börgesson and Hernelind (1999)
Thermal expansion, β_T [$1/^\circ C$]	$1.0 \cdot 10^{-5}$	Assumed
Dry specific heat, C_{vs} [$J/kg \cdot ^\circ C$]	800	Börgesson and Hernelind (1999)
Thermal conductivity, [$W/m \cdot ^\circ C$]	Eq. (4.32)	Fitted to experimental data in Börgesson and Hernelind (1999)
Thermal diffusion coefficient D_{Tv} [-]	Eq. (4.33)	Börgesson and Hernelind (1999)

Table 4.2. Rock Mass Properties

Parameter	Value	Source
Density, ρ_s [kg/m^3]	2650	Task A1 Description (Chapter 1).
Porosity, ϕ [-]	0.003	Task A1 Description (Chapter 1).
Young's Modulus, E [GPa]	60 GPa	Task A1 Description (Chapter 1).
Poisson's Ratio, ν [-]	0.25	Task A1 Description (Chapter 1).
Biot's effective stress parameter, α [-]	0.6	Task A1 Description (Chapter 1).
Wet specific heat, C_v [$J/kg \cdot ^\circ C$]	845	Task A1 Description (Chapter 1).
Thermal conductivity, K_m [$W/m \cdot ^\circ C$]	3.0	Task A1 Description (Chapter 1).
Thermal expansion, β [$1/^\circ C$]	$1.0 \cdot 10^{-5}$	Task A1 Description (Chapter 1).
Hydraulic permeability, k [m^2]	$7.0 \cdot 10^{-19}$	Task A1 Description (Chapter 1).
Van-Genuchten's retention parameter, P_0 [MPa]	5.5 MPa	Thomas et al. (2002)
Van-Genuchten's retention parameter, β_{VG}	1.493	Thomas et al. (2002)

Table 4.3. Properties of the emplacement container (inner shell)

Parameter	Value	Source
Density, ρ_s [kg/m ³]	7800	Task A1 Description (Chapter 1).
Hydraulic permeability, k_w [m ²]	$1.0 \cdot 10^{-27}$	Assumed low value
Porosity, ϕ [-]	$1.0 \cdot 10^{-5}$	Assumed low value
Young's modulus, E [GPa]	200	Task A1 Description (Chapter 1).
Poisson's ratio, ν [-]	0.3	Task A1 Description (Chapter 1).
Specific heat, C_v [J/kg°C]	4600	Task A1 Description (Chapter 1).
Thermal conductivity, K_m [W/m°C]	59	Task A1 Description (Chapter 1).
Thermal expansion coefficient, β [1/°C]	$1.2 \cdot 10^{-6}$	Task A1 Description (Chapter 1).

Table 4.4 Properties of the groundwater

Parameter	Value	Source
Thermal expansion coefficient, β_T [1/°C]	$4.0 \cdot 10^{-4}$	Standard thermo-physical table
Specific heat, C_{vw} [J/kg°C]	4180	Standard thermo-physical table
Viscosity, η_w [Ns/m ²] (at 25 °C)	$1.070 \cdot 10^3$	Standard thermo-physical table
Compressibility, β_p [1/Pa]	$4.4 \cdot 10^{-10}$	Standard thermo-physical table
Density, ρ_{w0} [kg/m ³] (at 25 °C)	997.0	Standard thermo-physical table
Vapor specific heat of water vapor, C_{vs} [J/kg°C]	1900	Standard thermo-physical table
Latent heat of vaporization, L_0 [J/kg]	$2.4 \cdot 10^6$	Standard thermo-physical table
Specific gas constant of water vapor, R [J/kg°C]	461.5	Standard thermo-physical table

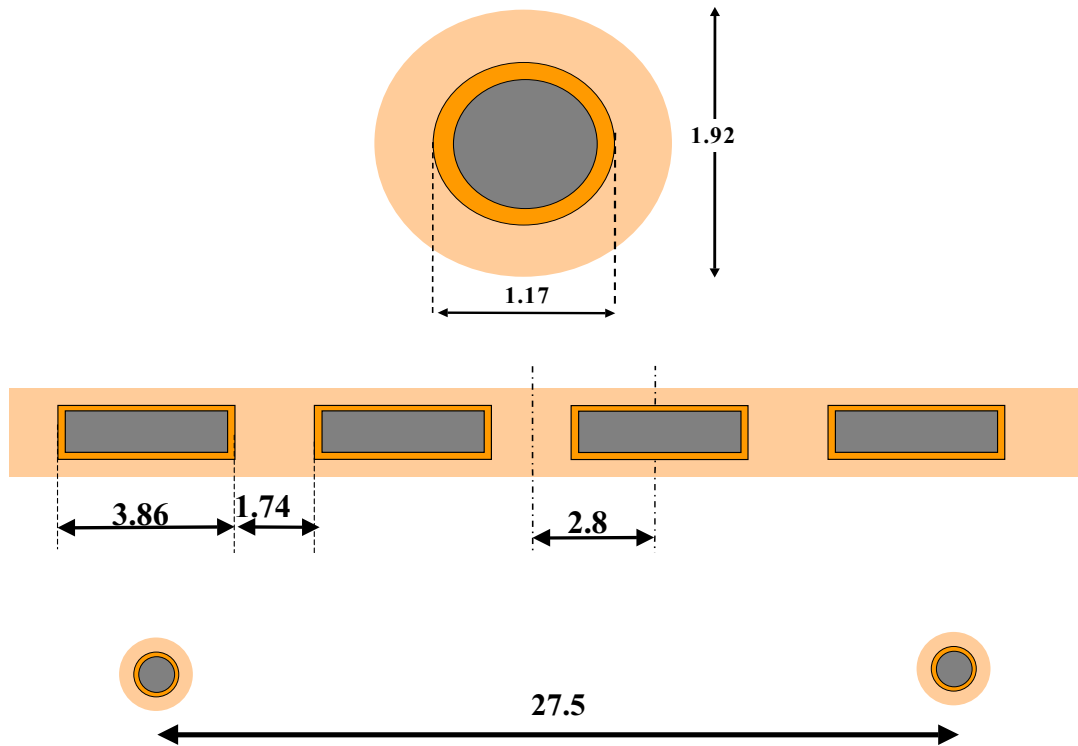


Figure 4.1. Geometry of the Engineered Barrier system for the hypothetical repository with horizontal deposition tunnels. (Top) Waste and waste over-pack (canister) in a horizontal deposition tunnel. (Middle) Distances between deposition between canisters within a deposition tunnel. (Bottom) Axial distance between adjacent deposition tunnels.

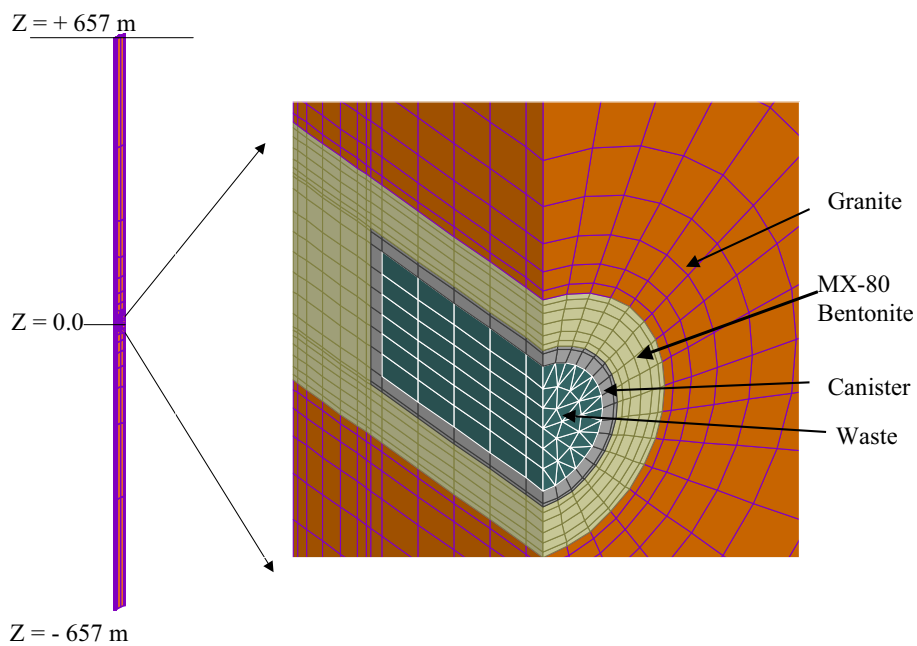


Figure 4.2 One quarter symmetric finite element model for a coupled THM simulation with ROCMAS.

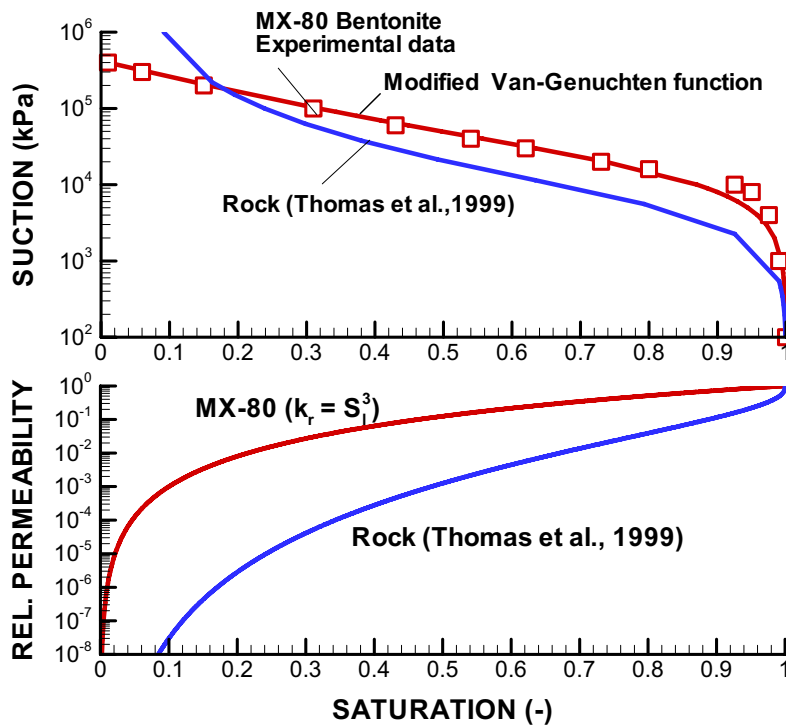


Figure 4.3. Water retention and relative permeability functions assigned to the bentonite buffer and the surrounding rock. The red squares are experimental values measured on a small sample of MX-80 bentonite whereas the lines indicated the functions used in the modeling.

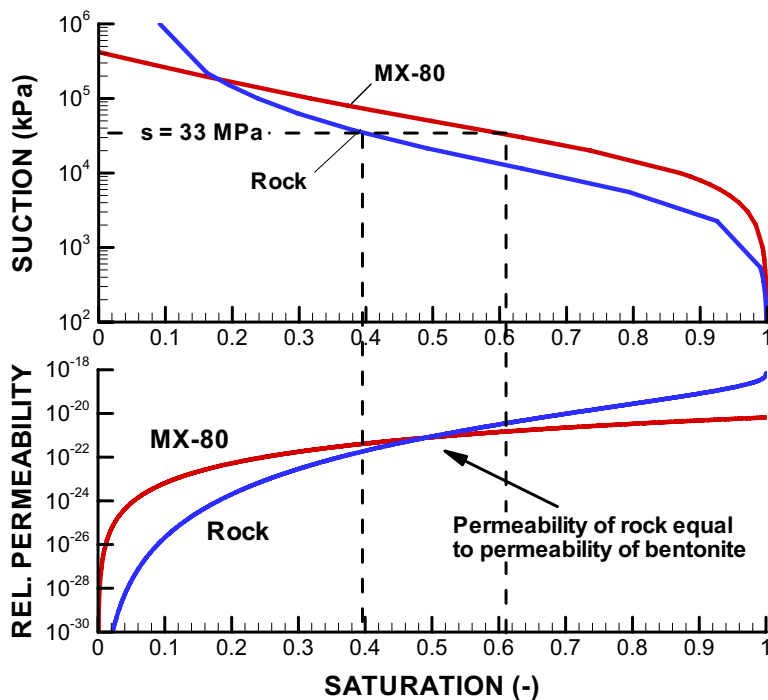


Figure 4.4. Water retention curves and absolute permeability of buffer and rock. The absolute permeability of rock may be as low as that of the bentonite if the initial suction pressure within the bentonite is transferred to the rock wall.

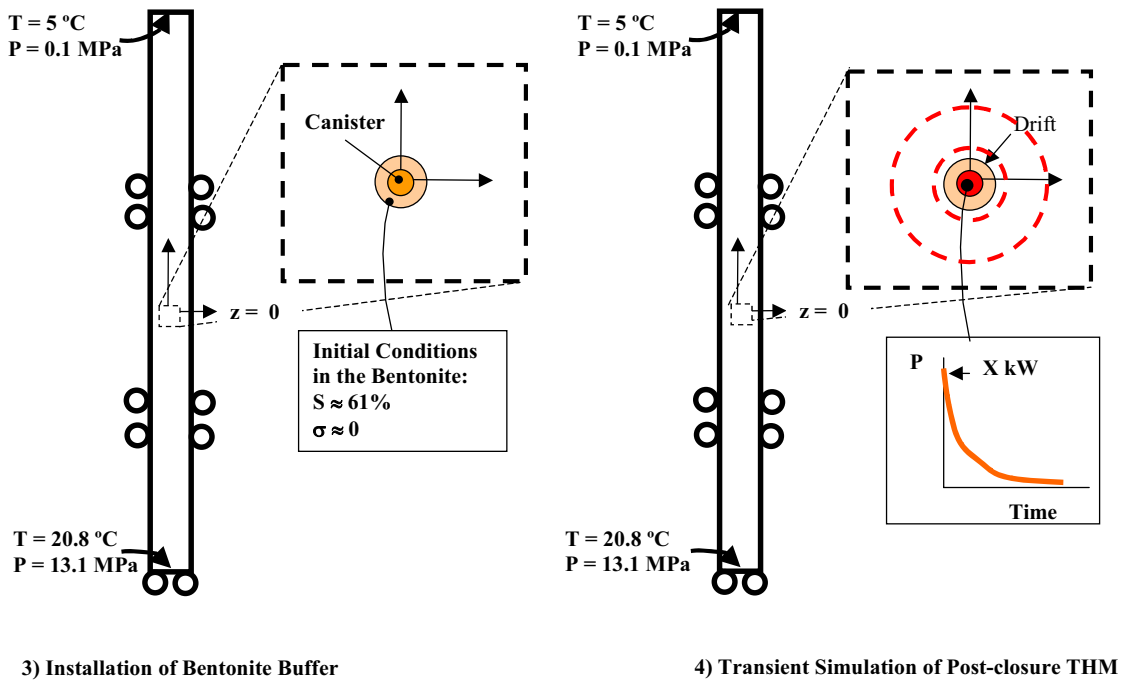
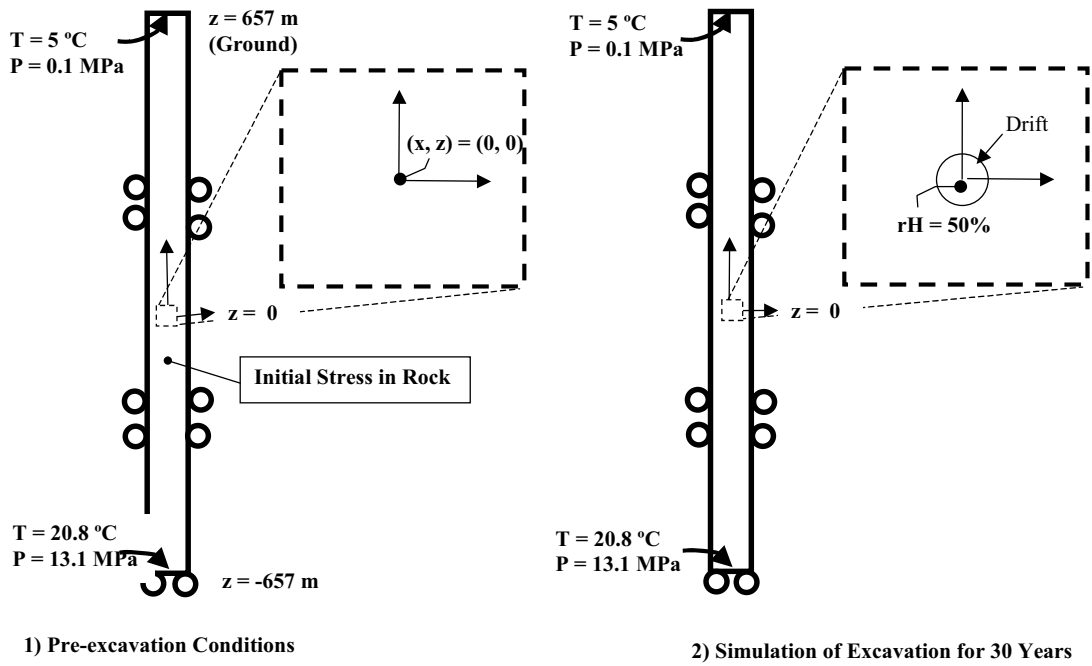


Figure 4.5. Specific modeling sequence, boundary and initial conditions for Task A1 with ROCMAS.

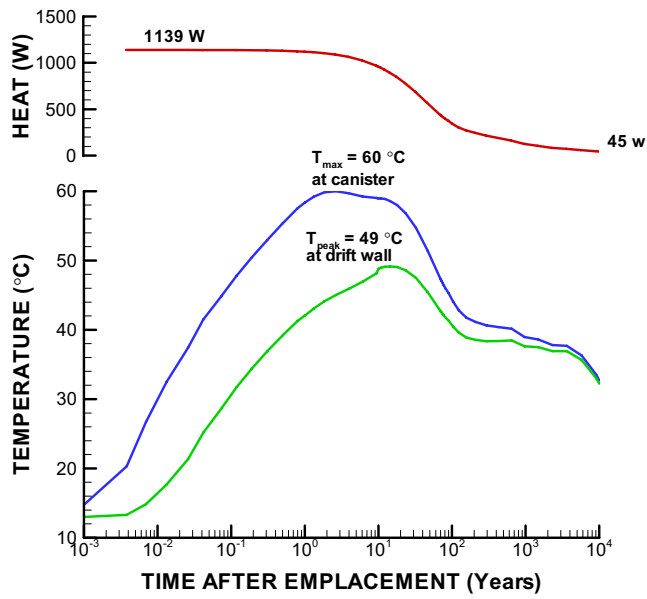


Figure 4.6. Decay of heat power released from the waste canister and evolution temperature at two points in the buffer.

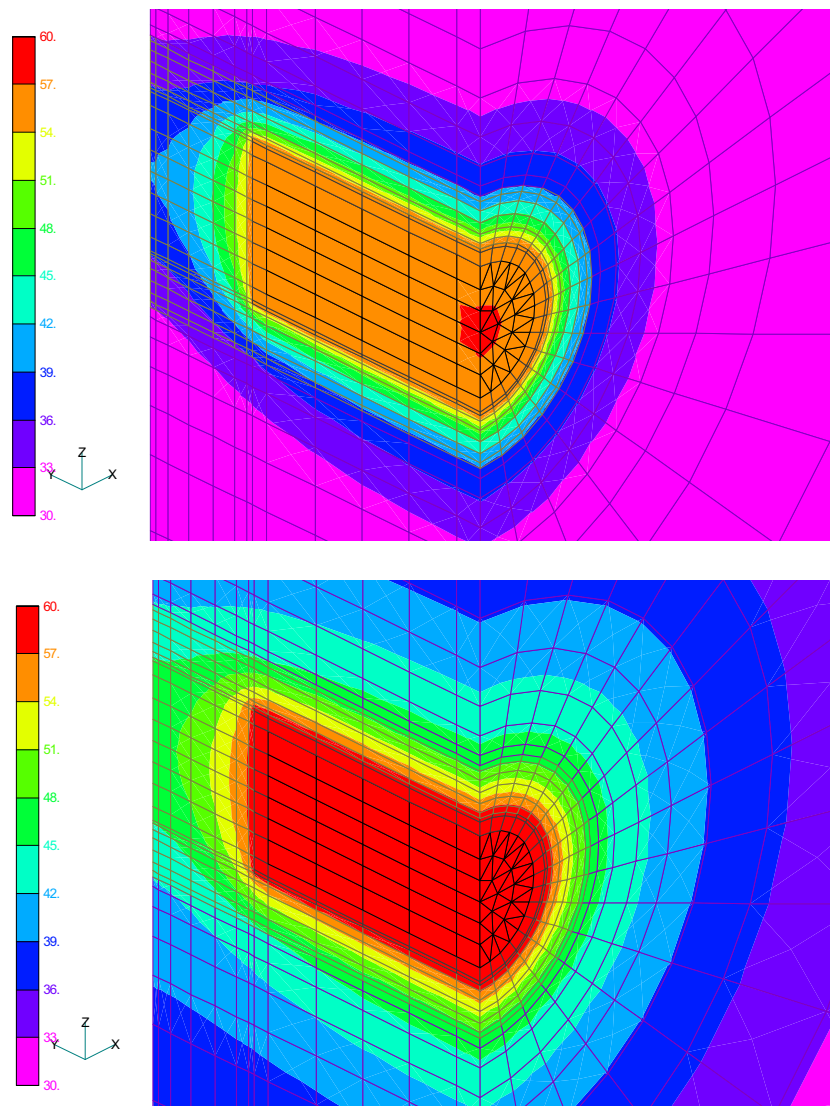


Figure 4.7. Temperature contours in degree Celsius at (top) 1 year and (bottom) 10 years.

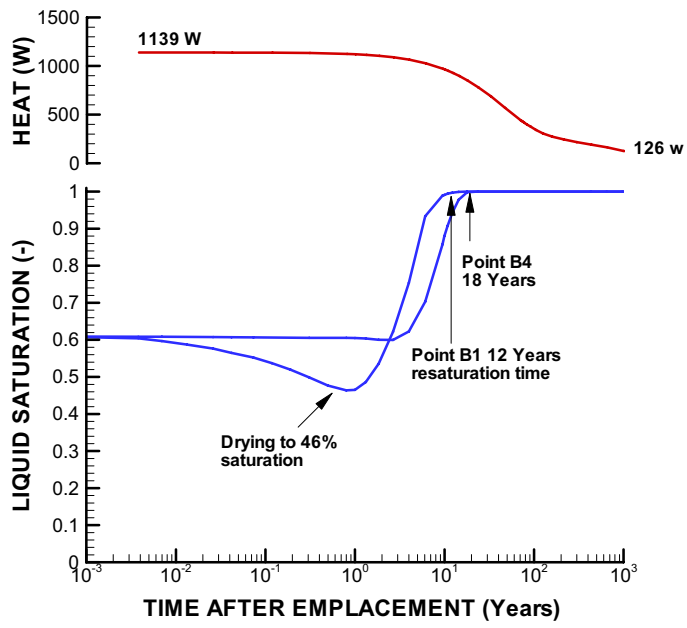


Figure 4.8. Evolution of liquid saturation at two points located in the buffer at the canister surface.

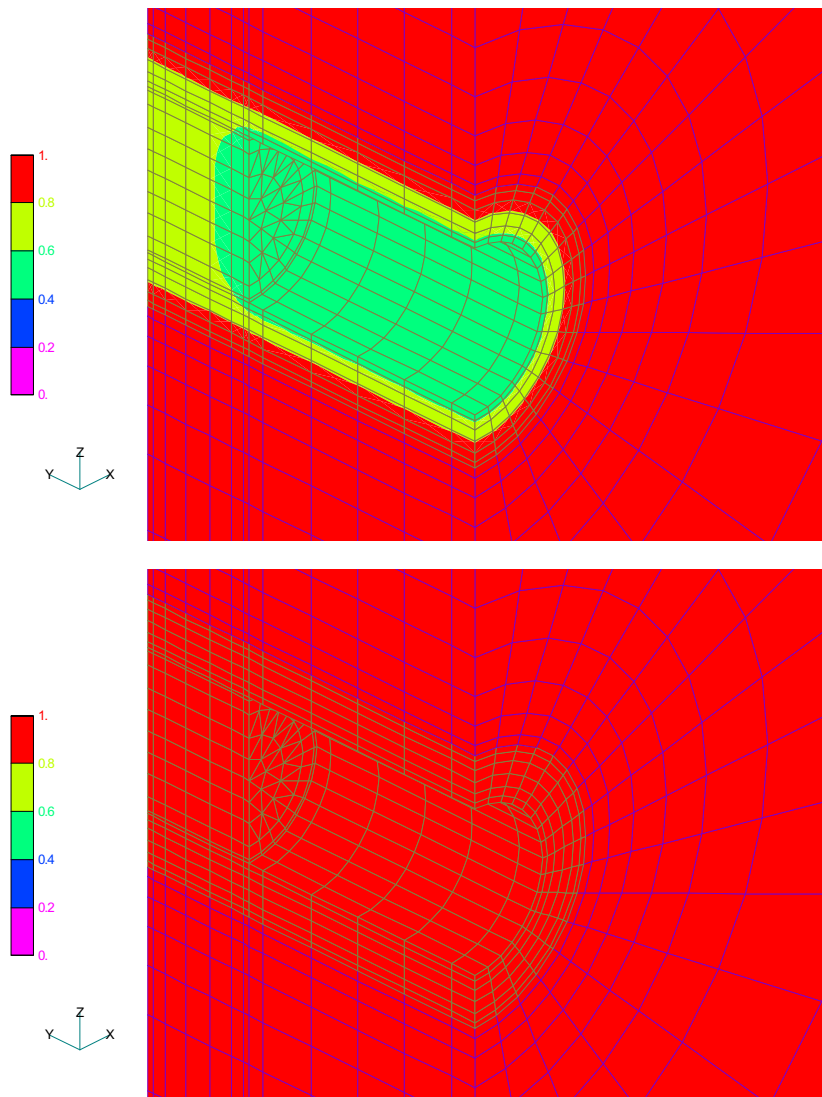


Figure 4.9. Distribution of liquid saturation in the buffer at (top) 1 and (bottom) 10 years.

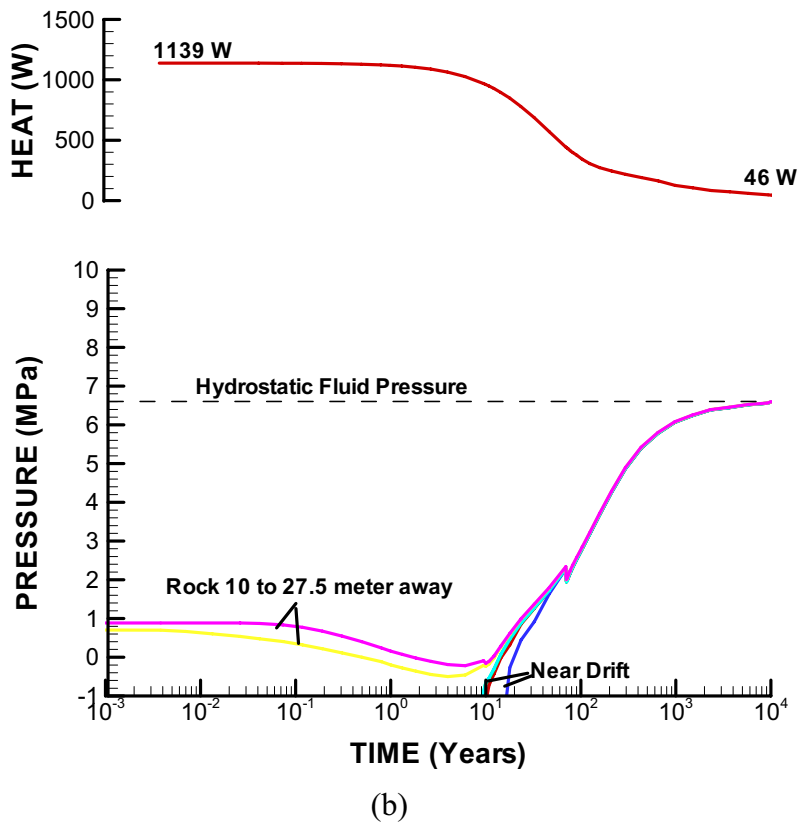
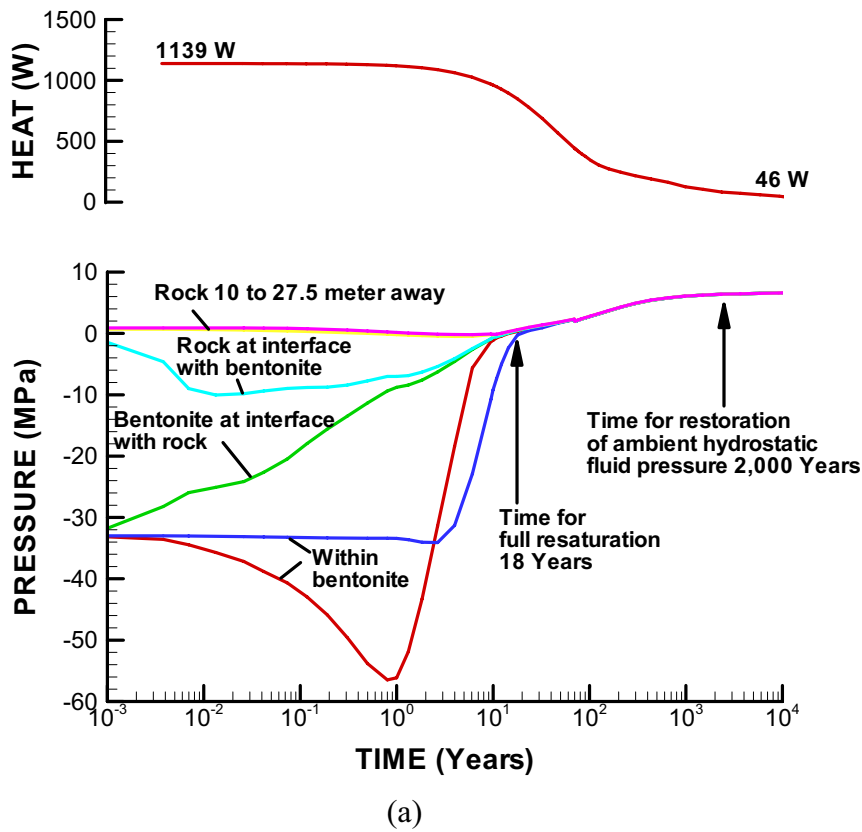


Figure 4.10. Evolution of fluid pressure at different locations within and outside the buffer.

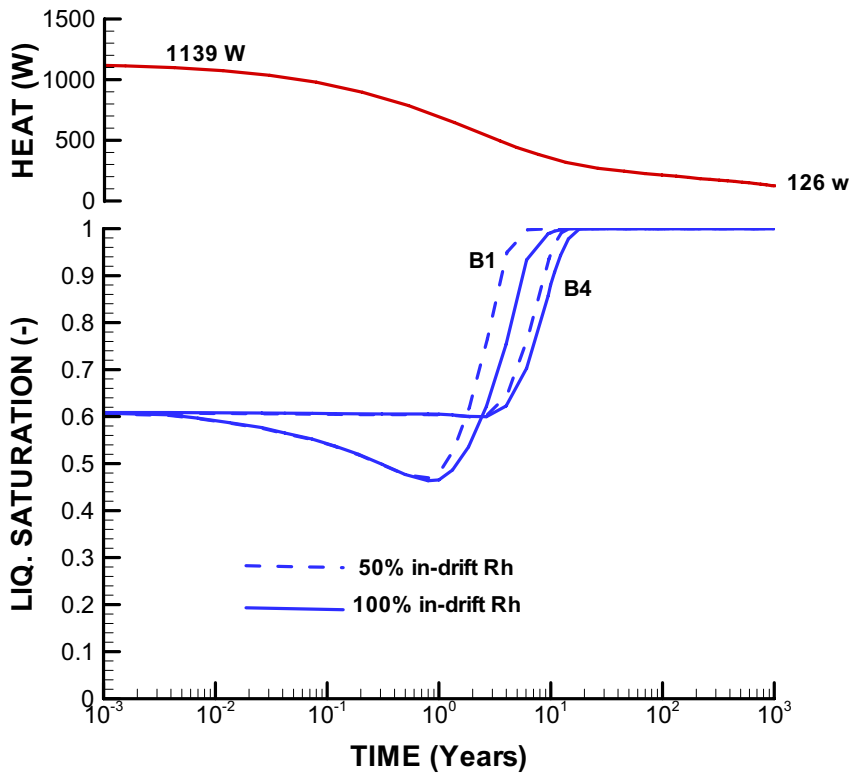


Figure 4.11. Effect of drift ventilation with 50% in-drift relative humidity on the evolution of liquid saturation at two points located in the buffer at the canister surface.

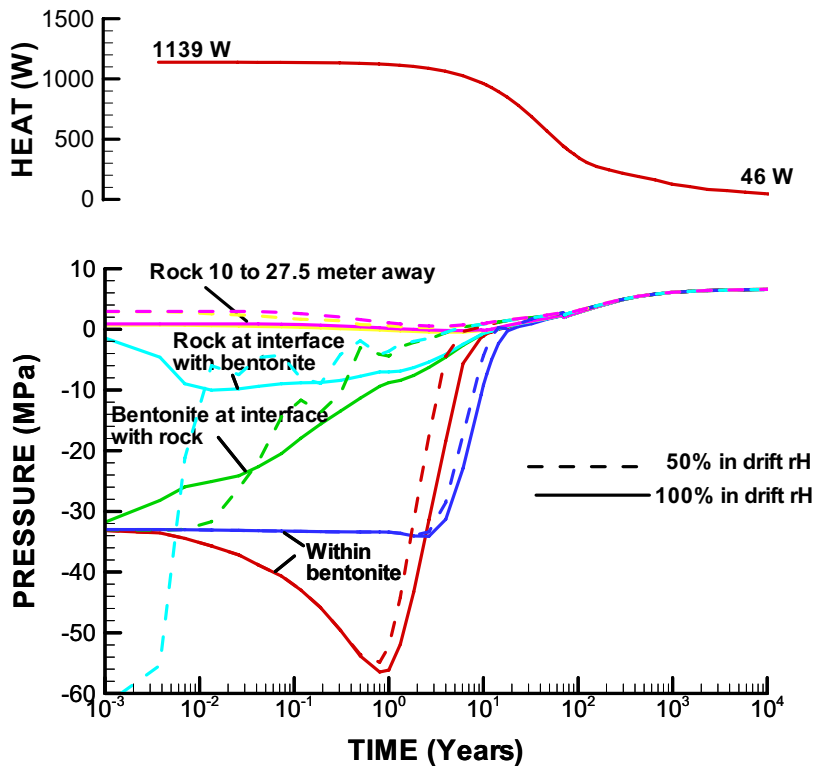


Figure 4.12. Effect of drift ventilation with 50% in-drift relative humidity on the evolution of liquid saturation at two points located in the buffer at the canister surface.

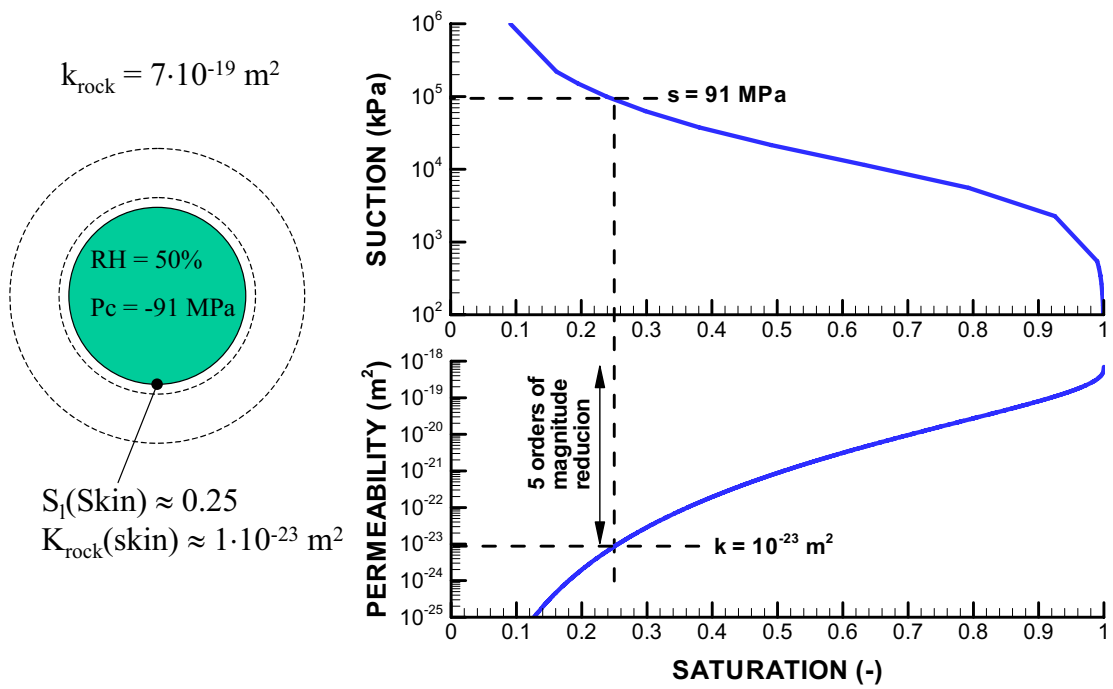


Figure 4.13. Illustration of the formation of a skin zone of very low permeability that can effectively prevent inflow into the drift.

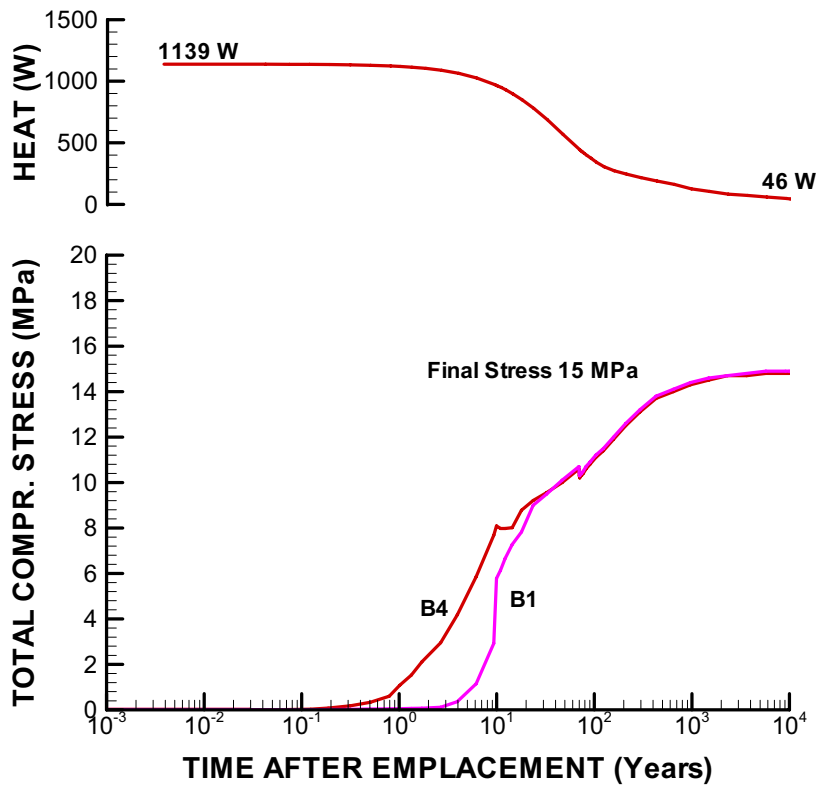


Figure 4.14. Evolution of total stress in the radial direction at two points in the buffer.

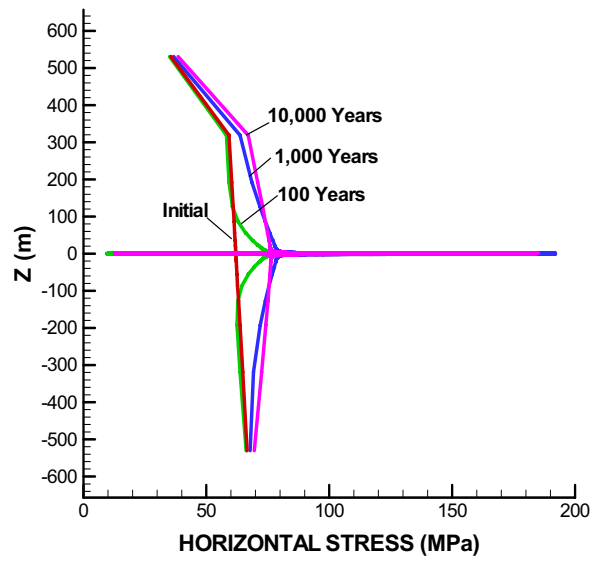


Figure 4.15. Vertical profiles of horizontal stress.

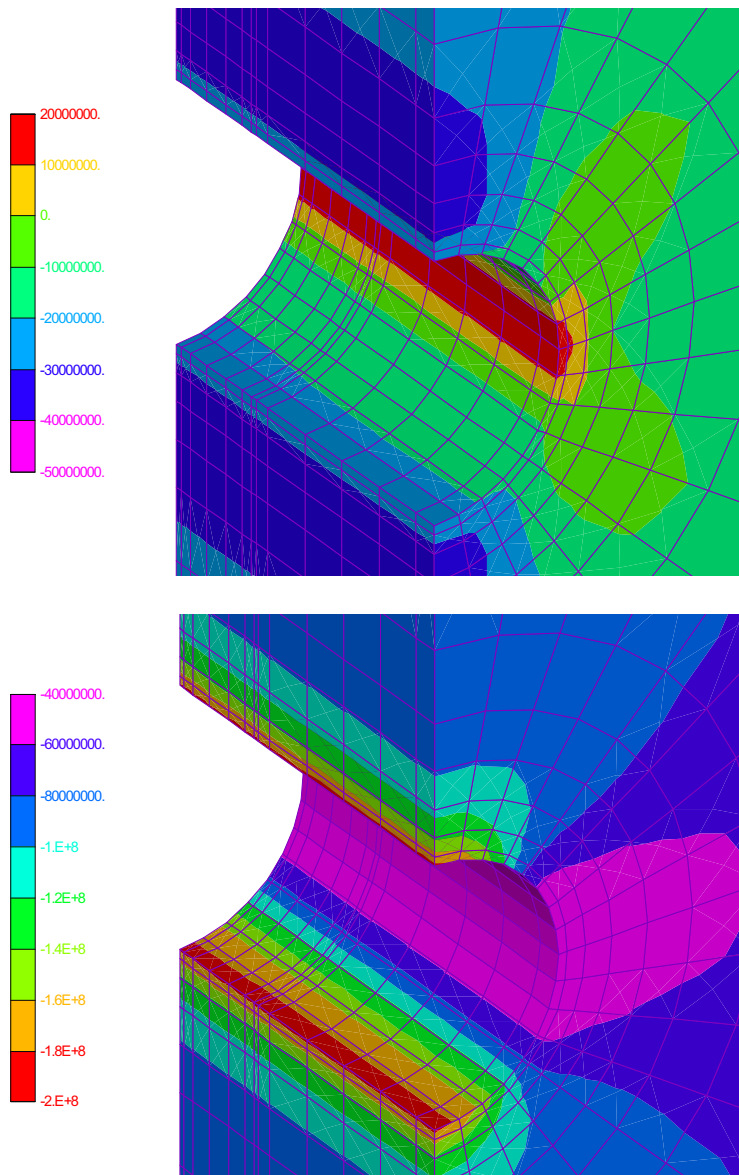
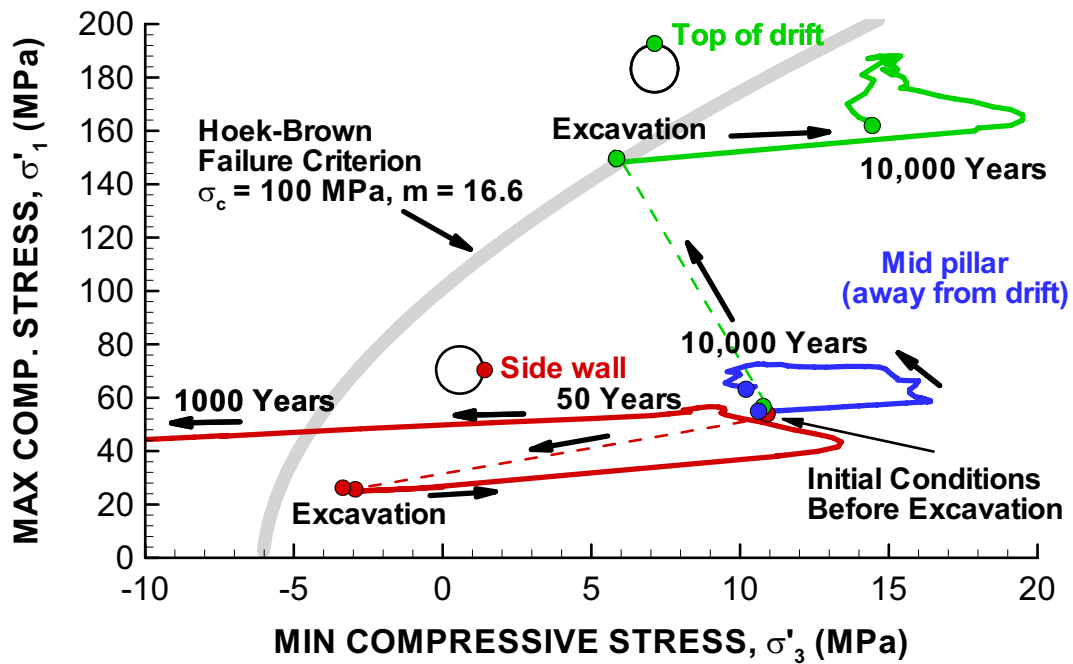
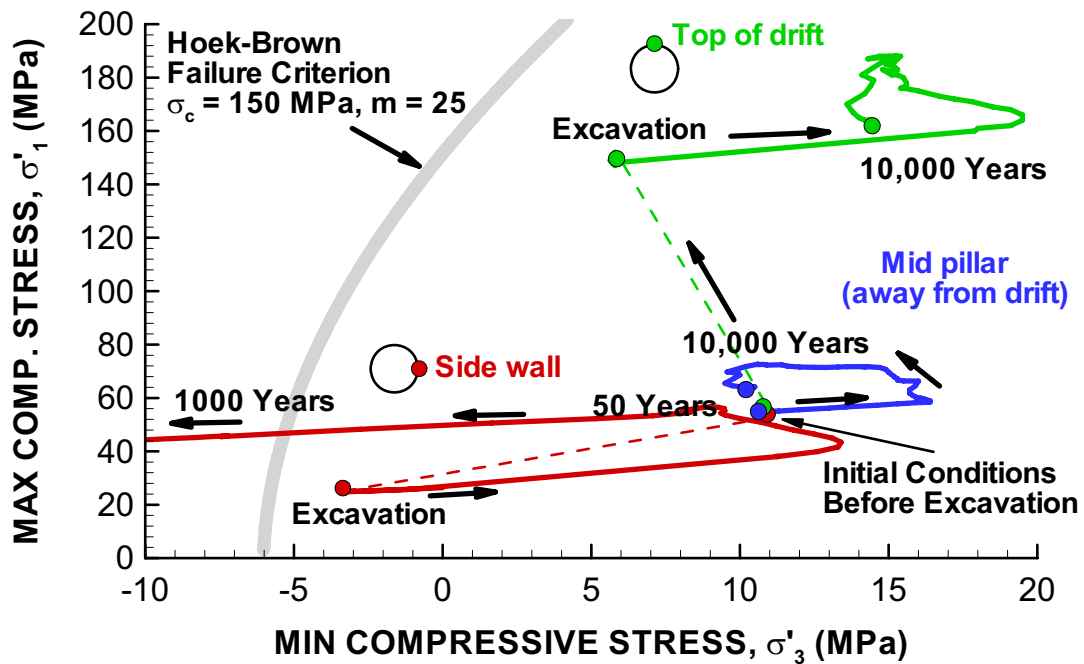


Figure 4.16. Contours of (top) minimum and (bottom) maximum compressive stress at 1,000 years. Negative values indicate compression (negative values indicate compressive stress).



(a)



(b)

Figure 4.17. Path of effective principal stresses relative to Hoek-Brown failure criterion with strength parameters corresponding to (a) excavated drift and (b) heated drift (positive values indicate compressive stress in this figure).

5. SKB/Clay team's preliminary THM modelling of Task A-1

L. Börgesson, Clay Technology AB
J. Hernelind, FEM-Tech AB

5.1 Introduction

The DECOVALEX-THMC project is an international co-operative project, initiated by SKI, the Swedish Nuclear Power Inspectorate, to support the development of mathematical models of coupled **T** (Thermal) **H** (Hydrological) **M** (Mechanical) and **C** (chemical) processes in the host rock of potential sites for nuclear fuel waste repositories. The objective of Task A of DECOVALEX-THMC is to assess the implications of coupled THM processes in the near field of a typical repository on its long term performance. The proposed work is an actual working example where the engineering experts would work in collaboration and interact with performance/safety analysts and experimentalists on a realistic case study of a repository. The proposed work is an example of integration of model development/calibration and interpretation of laboratory and in-situ data towards the final goal of building confidence to the PA process. The repository we consider is a hypothetical repository in the Canadian Shield. The geological setting, the physical characteristics of the spent fuel, engineered barriers and host rock, as well as the geometrical configuration of the repository are given detailed in Chapter 1.

This chapter presents SKB's results for sub-task A-1 which consists of preliminary, simplified modelling of the THM behaviour in the near field of the repository. The presentation is arranged in the following way:

- Finite element code
- Element mesh
- Material models and properties
- Modelling approach and boundary conditions
- Primary results

5.2 Finite element code

5.2.1 General

The finite element code ABAQUS was used for the calculations. ABAQUS contains a capability of modelling a large range of processes in many different materials as well as complicated three-dimensional geometry.

The code includes special material models for rock and soil and ability to model geological formations with infinite boundaries and in situ stresses, by e.g. the own weight of the medium. It also includes capability to make substructures with completely different finite element meshes and mesh density without connecting all nodes. Detailed information

of the available models, application of the code and the theoretical background is given in the ABAQUS code Manuals (ABAQUS, 2005).

5.2.2 Hydro-mechanical analyses in ABAQUS

The hydro-mechanical model consists of porous medium and wetting fluid and is based on equilibrium, constitutive equations, energy balance and mass conservation using the effective stress theory.

a) Equilibrium:

Equilibrium is expressed by writing the principle of virtual work for the volume under consideration in its current configuration at time t :

$$\int_V \boldsymbol{\sigma} : \delta \boldsymbol{\varepsilon} dV = \int_S \mathbf{t} \cdot \delta \mathbf{v} dS + \int_V \hat{\mathbf{f}} \cdot \delta \mathbf{v} dV, \quad (5-1)$$

where \mathbf{v} is a virtual velocity field, $\delta \boldsymbol{\varepsilon} = \text{sym}(\partial \delta \mathbf{v} / \partial \mathbf{x})$ is the virtual rate of deformation, $\boldsymbol{\sigma}$ is the true (Cauchy) stress, \mathbf{t} are the surface tractions per unit area, and $\hat{\mathbf{f}}$ are body forces per unit volume. For our system, $\hat{\mathbf{f}}$ will often include the weight of the wetting liquid,

$$\mathbf{f}_w = S_r n \rho_w \mathbf{g}, \quad (5-2)$$

where S_r is the degree of saturation, n the porosity, ρ_w the density of the wetting liquid and \mathbf{g} is the gravitational acceleration, which we assume to be constant and in a constant direction (so that, for example, the formulation cannot be applied directly to a centrifuge experiment unless the model in the machine is small enough that \mathbf{g} can be treated as constant). For simplicity we consider this loading explicitly so that any other gravitational term in $\hat{\mathbf{f}}$ is only associated with the weight of the dry porous medium. Thus, we write the virtual work equation as

$$\int_V \boldsymbol{\sigma} : \delta \boldsymbol{\varepsilon} dV = \int_S \mathbf{t} \cdot \delta \mathbf{v} dS + \int_V \mathbf{f} \cdot \delta \mathbf{v} dV + \int_V S_r n \rho_w \mathbf{g} \cdot \delta \mathbf{v} dV, \quad (5-3)$$

where \mathbf{f} are all body forces except the weight of the wetting liquid.

The simplified equation used in ABAQUS for the effective stress is:

$$\bar{\boldsymbol{\sigma}}^* = \boldsymbol{\sigma} + \chi u_w \mathbf{I}. \quad (5-4)$$

where $\boldsymbol{\sigma}$ is the total stress, u_w is the pore water pressure, χ is a function of the degree of saturation (usual assumption $\chi = S_r$), and \mathbf{I} the unitary matrix.

b) Energy balance

The conservation of energy implied by the first law of thermodynamics states that the time rate of change of kinetic energy and internal energy for a fixed body of material is equal to the sum of the rate of work done by the surface and body forces. This can be expressed as (not considering the thermal part, which is solved as uncoupled heat transfer; cf. Equation 5-15):

$$\frac{d}{dt} \int_V \left(\frac{1}{2} \rho \mathbf{v} \cdot \mathbf{v} + \rho U \right) dV = \int_S \mathbf{v} \cdot \mathbf{t} dS + \int_V \mathbf{f} \cdot \mathbf{v} dV \quad (5-5)$$

where

ρ is the current density,
 \mathbf{v} is the velocity field vector,
 U is the internal energy per unit mass,
 \mathbf{t} is the surface traction vector,
 \mathbf{f} is the body force vector, and

c) Constitutive equations

The constitutive equation for the solid is expressed as:

$$d\boldsymbol{\tau}^c = \mathbf{H} : d\boldsymbol{\varepsilon} + \mathbf{g} \quad (5-6)$$

where $d\boldsymbol{\tau}^c$ is the stress increment, \mathbf{H} the material stiffness, $d\boldsymbol{\varepsilon}$ the strain increment and \mathbf{g} is any strain independent contribution (e.g. thermal expansion). \mathbf{H} and \mathbf{g} are defined in terms of the current state, direction for straining, etc., and of the kinematic assumptions used to form the generalised strains.

The constitutive equation for the liquid (static) in the porous medium is expressed as:

$$\frac{\rho_w}{\rho_w^0} \approx 1 + \frac{u_w}{K_w} - \varepsilon_w^{th}, \quad (5-7)$$

where ρ_w is the density of the liquid, ρ_w^0 is its density in the reference configuration, $K_w(T)$ is the liquid's bulk modulus, and

$$\varepsilon_w^{th} = 3\alpha_w(T - T_w^0) - 3\alpha_w|_{T^I}(T^I - T_w^0) \quad (5-8)$$

is the volumetric expansion of the liquid caused by temperature change. Here $\alpha_w(T)$ is the liquid's thermal expansion coefficient, T is the current temperature, T^I is the initial temperature at this point in the medium, and T_w^0 is the reference temperature for the thermal expansion. Both u_w/K_w and ε_w^{th} are assumed to be small.

d) Mass conservation

The mass continuity equation for the fluid combined with the divergence theorem implies the point wise equation:

$$\frac{1}{J} \frac{d}{dt} (J \rho_w S_r n) + \frac{\partial}{\partial \mathbf{x}} \cdot (\rho_w S_r n \mathbf{v}_w) = 0. \quad (5-9)$$

where J is the determinant of the Jacobian matrix of the skeleton motion and \mathbf{x} is position. The constitutive behaviour for pore fluid is governed by Darcy's law, which is generally applicable to low fluid velocities. Darcy's law states that, under uniform conditions, the volumetric flow rate of the wetting liquid through a unit area of the medium, $S_r n \mathbf{v}_w$, is proportional to the negative of the gradient of the piezometric head:

$$S_r n \mathbf{v}_w = -\hat{\mathbf{k}} \frac{\partial \phi}{\partial \mathbf{x}}, \quad (5-10)$$

where $\hat{\mathbf{k}}$ is the permeability of the medium and ϕ is the piezometric head, defined as:

$$\phi \stackrel{def}{=} z + \frac{\mathbf{u}_w}{g \rho_w} \quad (5-11)$$

where z is the elevation above some datum and g is the magnitude of the gravitational acceleration, which acts in the direction opposite to z . $\hat{\mathbf{k}}$ can be anisotropic and is a function of the saturation and void ratio of the material. $\hat{\mathbf{k}}$ has a unit of velocity (length/time). [Some authors refer to $\hat{\mathbf{k}}$ as the hydraulic conductivity and define the permeability as

$$\hat{\mathbf{K}} = \frac{\nu}{g} \hat{\mathbf{k}} \quad (5-12)$$

where ν is the kinematic viscosity of the fluid.]

We assume that g is constant in magnitude and direction, so

$$\frac{\partial \phi}{\partial \mathbf{x}} = \frac{1}{g \rho_w} \left(\frac{\partial \mathbf{u}_w}{\partial \mathbf{x}} - \rho_w \mathbf{g} \right) \quad (5-13)$$

e) Vapour flow

Vapour flow is modelled as a diffusion process driven by a temperature gradient (coded as UEL user supplied routine with stiffness and flow).

$$\mathbf{q}_v = -D_{Tv} \frac{\partial T}{\partial \mathbf{x}} \quad (5-14)$$

where \mathbf{q}_v is the vapour flux and D_{Tv} the thermal vapour diffusivity.

5.2.3 Uncoupled heat transfer analysis

a) Energy balance

The basic energy balance is (neglecting mechanical contribution; cf Equation 5-5)

$$\int_V \rho \dot{U} dV = \int_S q dS + \int_V r dV \quad (5-15)$$

where V is a volume of solid material, with surface area S ; ρ is the density of the material; \dot{U} is the material time rate of the internal energy; q is the heat flux per unit area of the body, flowing into the body; and r is the heat supplied externally into the body per unit volume.

It is assumed that the thermal and mechanical problems are uncoupled in the sense that $U = U(T)$ only, where T is the temperature of the material, and q and r do not depend on the strains or displacements of the body. For simplicity a Lagrangian description is assumed, so "volume" and "surface" mean the volume and surface in the reference configuration.

b) Constitutive definition

The relationship is usually written in terms of a specific heat, neglecting coupling between mechanical and thermal problems:

$$c(T) = \frac{dU}{dT}, \quad (5-16)$$

Heat conduction is assumed to be governed by the Fourier law.

$$\mathbf{f}_q = -\mathbf{k} \frac{\partial T}{\partial \mathbf{x}} \quad (5-17)$$

where \mathbf{f}_q is the heat flux and \mathbf{k} is the heat conductivity matrix, $\mathbf{k} = \mathbf{k}(T)$. The conductivity can be fully anisotropic, orthotropic, or isotropic.

5.2.4 Coupling of thermal and hydro-mechanical solutions

In ABAQUS the coupled problem is solved through a "staggered solution technique" as sketched in Figure 5.1 and below.

1. First a thermal analysis is performed where heat conductivity and specific heat are defined as functions of saturation and water content. In the first analysis these parameters are assumed to be constant and in the subsequent analyses they are read from an external file.

2. The hydro-mechanical model calculates stresses, pore pressures, void ratios, degree of saturation etc. as function of time. Saturation and void ratio histories are written onto an external file.
3. The material parameters update module reads the file with saturation and void ratio data and creates a new file containing histories for saturation and water content.
4. The saturation and water content histories are used by the thermal model in the following analysis.
5. Steps 1-3 are repeated if parameter values are found to be different compared to those of the previous solution.

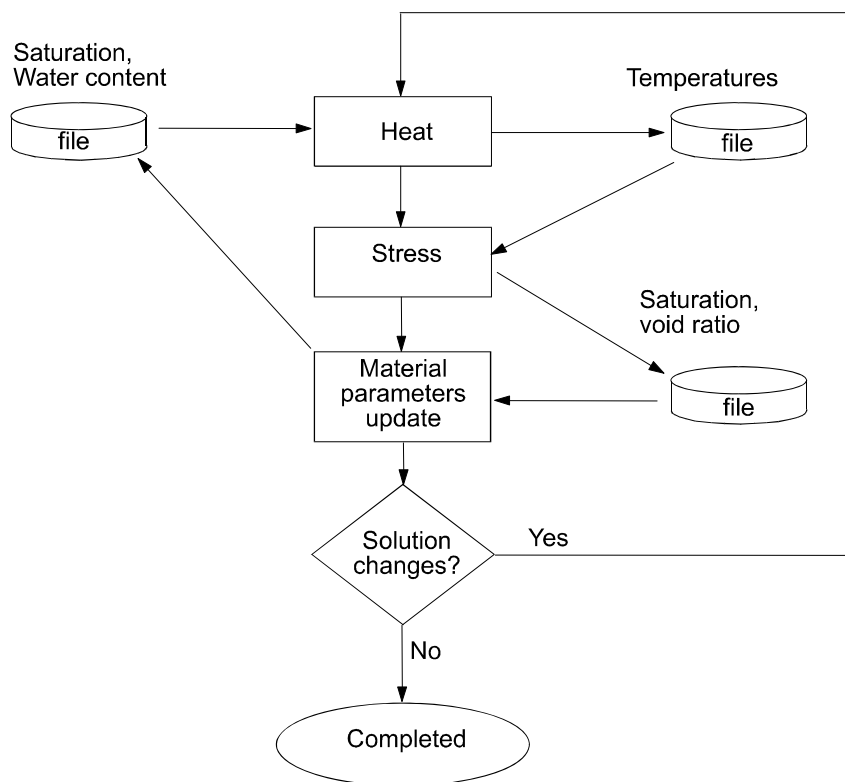


Figure 5.1. In ABAQUS, heat transfer calculations and hydro-mechanical calculations are decoupled. By using the iteration procedure schematically shown above, the effects of a fully coupled THM model are achieved.

5.3 Element mesh

The finite element mesh models a repository, designed in a similar way as the Swedish KBS-3H concept, located 657 m below the ground surface. It is a 3D model and is shown in Figure 5.2. The height of the model is 657 m above the tunnel and 657 m below the tunnel. The basis for the geometry is described in Figure 1-11. All vertical boundaries are symmetry planes:

- A vertical symmetry plane along the axis of the tunnel

- A vertical symmetry plane perpendicular to the tunnel axis that cuts a canister in two halves
- A vertical symmetry plane perpendicular to the tunnel axis half way between two canisters
- A vertical symmetry plane parallel to the tunnel axis half way between two tunnels

The model consists of basically three different materials, namely the rock, the buffer and the canister. The properties of the rock vary with depth.

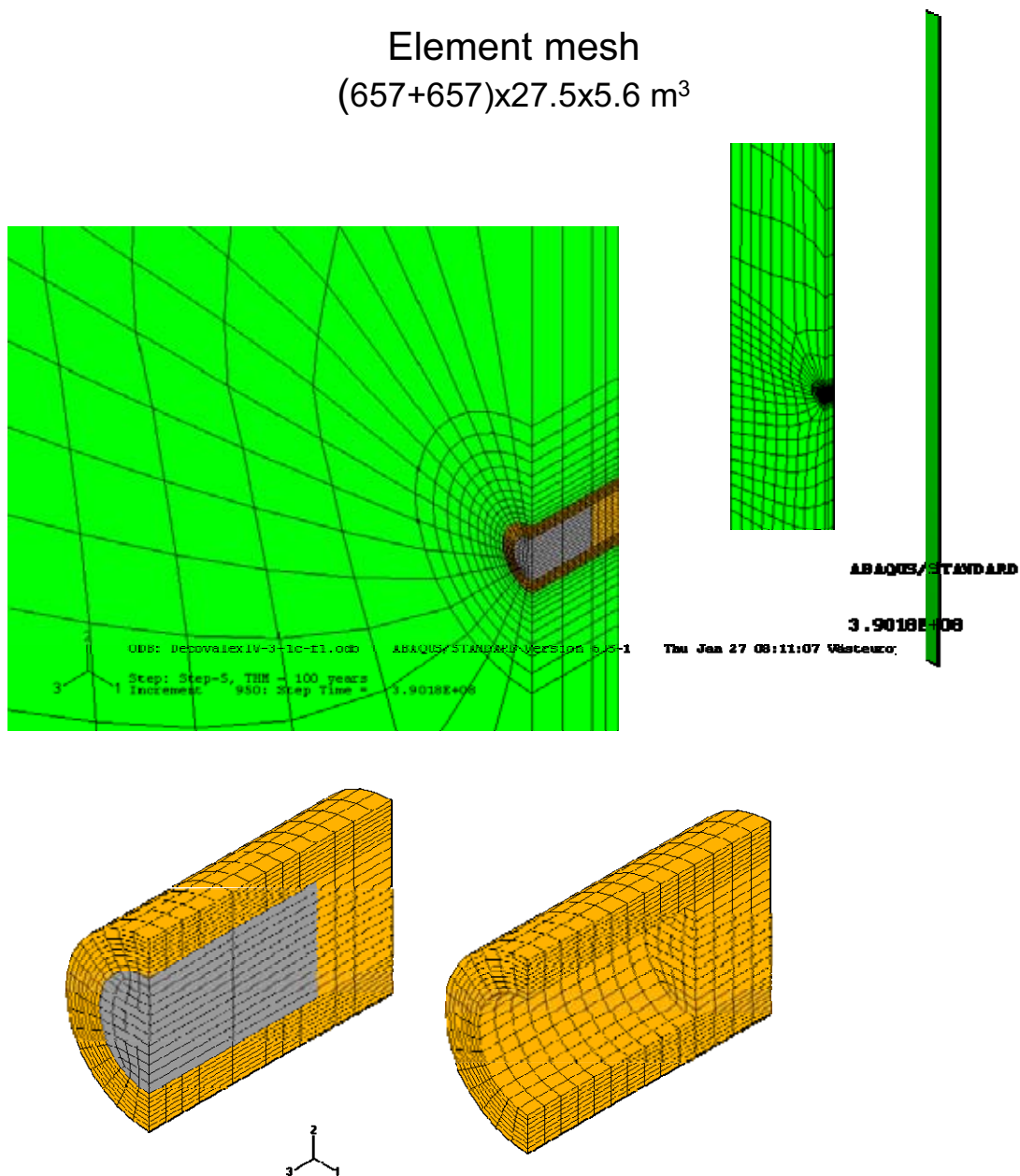


Figure 5.2. Element mesh. Green colour: rock. Orange colour: bentonite buffer. Grey colour: canister.

5.4 Material models and properties

The material models used for modelling the different processes in the three materials and their parameter values will be briefly described in this chapter.

5.4.1 Buffer

The models and data used for the buffer are essentially the same as used for modelling the wetting of KBS-3V (Börgesson and Hernelind, 1999).

a) Thermal flux by conduction

The only thermal flux that is modelled is the thermal conduction with the thermal conductivity κ and specific heat c . The thermal conductivity has been measured as a function of the degree of saturation. The laboratory results at the void ratio 0.8 are shown in Table 5-1 together with the parameter values for the ABAQUS model (linear interpolation between the values). The specific heat has been calculated as the weighed average of the specific heat of water and particles according to Equation 5-18.

$$c=800/(1+w)+4200w/(1+w) \quad (5-18)$$

Equation 5-18 yields the input parameters shown in Table 5-2 (linear interpolation)

Table 5-1. Thermal conductivity κ of the buffer material as a function of the degree of saturation S_r at the void ratio 0.8

S_r	κ (W/m,K)	<i>Measurements</i>
0	0.3	
0.2	0.3	
0.3	0.4	
0.4	0.55	
0.5	0.75	
0.6	0.95	
0.7	1.1	
0.8	1.2	
0.9	1.25	
1.0	1.3	

Table 5-2. Heat capacity c of the buffer material as a function of the water ratio w

w	C (Ws/m,kg)
0	800
0.1	1109
0.2	1367
0.3	1585
1.0	2500

b) Water liquid flux

The water flux in the liquid phase is modeled to be governed by Darcy's law with the water pressure difference as driving force in the same way as for water saturated clay.

The magnitude of the hydraulic conductivity K_p of partly saturated clay is a function of the void ratio, the degree of saturation and the temperature. K_p is assumed to be a function of the hydraulic conductivity K of saturated clay and the degree of saturation S_r according to Equation 5-19.

$$K_p = (S_r)^\delta K \quad (5-19)$$

where

- K_p = hydraulic conductivity of partly saturated soil (m/s)
- K = hydraulic conductivity of completely saturated soil (m/s)
- δ = parameter (usually between 3 and 10)

For the reference material the standard value $\delta = 3$ has been found to be satisfactory according to calibration and validation calculations.

Water transport driven by gravity and density gradients is included in the model as well.

The hydraulic conductivity of water saturated bentonite has been measured at different temperatures and void ratios (Börgesson et al., 1995). Table 5-3 shows the values for the model.

Table 5-3. Hydraulic conductivity K as a function of void ratio e and temperature T

T (°C)	e	K (m/s)
20	0.4	$0.035 \cdot 10^{-13}$
20	0.6	$0.2 \cdot 10^{-13}$
20	0.8	$0.65 \cdot 10^{-13}$
20	1.0	$1.75 \cdot 10^{-13}$
40	0.4	$0.05 \cdot 10^{-13}$
40	0.6	$0.31 \cdot 10^{-13}$
40	0.8	$1.0 \cdot 10^{-13}$
40	1.0	$2.75 \cdot 10^{-13}$
60	0.4	$0.07 \cdot 10^{-13}$
60	0.6	$0.44 \cdot 10^{-13}$
60	0.8	$1.45 \cdot 10^{-13}$
60	1.0	$3.85 \cdot 10^{-13}$
80	0.4	$0.1 \cdot 10^{-13}$
80	0.6	$0.55 \cdot 10^{-13}$
80	0.8	$1.8 \cdot 10^{-13}$
80	1.0	$4.9 \cdot 10^{-13}$

c) Water vapor flux

The water vapor flux is modeled as a diffusion processes driven by the temperature gradient and the water vapor pressure gradient (at isothermal conditions) according to Eq. 5-20.

$$q_v = -D_{Tv} \nabla T - D_{pv} \nabla p_v \quad (5-20)$$

where

- q_v = vapour flow
- D_{Tv} = thermal vapour flow diffusivity
- T = temperature
- D_{pv} = isothermal vapour flow diffusivity
- p_v = vapour pressure

The isothermal vapour flow is neglected and thus $D_{pv} = 0$.

The thermal water vapour diffusivity D_{Tv} can be evaluated from moisture redistribution tests by calibration calculations. The following relations were found to yield acceptable results:

$$D_{Tv} = D_{Tvb} \quad 0.3 \leq S_r \leq 0.7 \quad (5-21)$$

$$D_{Tv} = D_{Tvb} \cdot \cos^a \left(\frac{S_r - 0.7}{0.3} \cdot \frac{\pi}{2} \right) \quad S_r \geq 0.7 \quad (5-22)$$

$$D_{Tv} = D_{Tvb} \cdot \sin^b \left(\frac{S_r}{0.3} \cdot \frac{\pi}{2} \right) \quad S_r \leq 0.3 \quad (5-23)$$

where a and b are factors that regulates the decreased vapour flux at high and low degree of saturation.

The diffusivity is thus constant with a basic value D_{Tvb} between 30% and 70% degree of saturation. It decreases strongly to $D_{Tv} = 0$ at 0% and 100% saturation. The influence of temperature and void ratio on the diffusivity is not known and not considered in the model.

The thermal vapour flow diffusivity D_{Tvb} and the parameters a and b according to Equations 5-21 to 5-23 have been determined with the calibration calculations of the moisture redistribution tests. The following values were chosen: $D_{Tvb} = 0.7 \cdot 10^{-11} \text{ m}^2/\text{s.K}$, $a = 6$ and $b = 6$.

d) Hydraulic coupling between the pore water and the pore gas

The pore pressure u_w of the unsaturated buffer material, which is always negative, is modeled as being a function of the degree of saturation S_r , independent of the void ratio (water retention curve).

$$u_w = f(S_r) \quad (5-24)$$

ABAQUS also allows for hysteresis effects, which means that two curves may be given (drying and wetting curves). The pore air pressure is not modelled.

The water retention curve has been determined from measurements of the total suction, the matrix suction and the swelling pressure. The measurements have been converted to degree of saturation for the reference density. Figure 5.3 shows the relation used in the model.

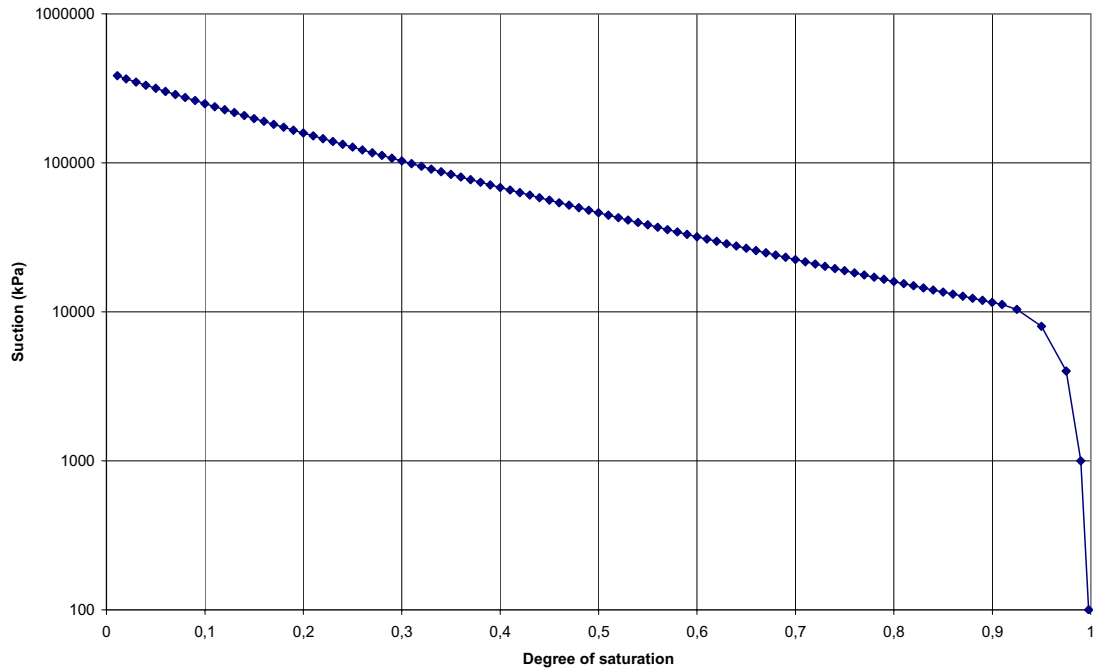


Figure 5.3. Retention curve of MX-80 at the void ratio 0.8.

e) Mechanical behavior of the structure

The mechanical behavior has been modeled with a non-linear Porous Elastic Model and Drucker-Prager Plasticity model. The effective stress theory is applied and adapted to unsaturated conditions according to Eq. 5-4 by Bishop. The shortcoming of the effective stress theory is compensated for by a correction called moisture swelling (see below).

The Porous Elastic Model implies a logarithmic relation between the void ratio e and the average effective stress p according to Equation 5-25. ‘

$$\Delta e = \kappa \Delta \ln p \tag{5-25}$$

where κ = porous bulk modulus and Poisson’s ratio ν is also required.

The Drucker-Prager Plasticity model contains the following parameters:

- β = friction angle in the p - q plane
- d = cohesion in the p - q plane
- ψ = dilation angle
- q = $f(\varepsilon_{pl}^d)$ = yield function

The yield function is the relation between Mises' stress q and the plastic deviatoric strain ε_p^d at a specified stress path. The dilation angle determines the volume change during shear.

The following data has been used for the Porous Elastic model: $\kappa = 0.20$ and $\nu = 0.4$. The value of κ has been derived from oedometer and swelling pressure tests (Börgesson et al., 1995).

The following data was used for the *Drucker-Prager Plasticity* model: $\beta = 16^\circ$, $d = 100$ kPa and $\psi = 2^\circ$.

The friction angle in the q - p plane and the dilation angle were taken from triaxial test results (Börgesson et al., 1995) with the curved failure line approximated to a straight line.

Table 5-4. Yield function

q (kPa)	ε_{pl}
1	0
50	0.005
100	0.02
150	0.04
200	0.1

f) Thermal expansion

The volume change caused by the thermal expansion of water and particles can be modeled with the parameters:

α_s = coefficient of thermal expansion of solids

α_w = coefficient of thermal expansion of water.

Only the expansion of the separate phases is taken into account. The possible change in volume of the structure by thermal expansion (not caused by expansion of the separate phases) is not modelled. However, a thermal expansion in water volume will change the degree of saturation which in turn will change the volume of the structure. The following values have been used: $\alpha_w = 3.0 \cdot 10^{-4}$ and $\alpha_s = 0$.

g) Mechanical behavior of the separate phases

The water and the particles are mechanically modeled as separate phases with linear elastic behavior. The pore air is not mechanically modeled. The following standard values have been used for the properties of the water and solid phases:

$B_w = 2.1 \cdot 10^6$ kPa (bulk modulus of water)

$B_s = 2.1 \cdot 10^8$ kPa (bulk modulus of solids)

$\rho_w = 1000$ kg/m³ (density of water)

$\rho_s = 2780$ kg/m³ (density of solids)

h) Mechanical coupling between the structure and the pore water

The mechanical behaviour is modelled to be governed by the effective stress theory and a procedure called moisture swelling.

Effective stress theory: The effective stress concept according to Bishop is used for modelling the mechanical behaviour of the water-unsaturated buffer material:

$$s_e = (s - u_a) + \chi(u_a - u_w) \quad (5-26)$$

Equation 5-26 is simplified in the following way:

$u_a = 0$ (no account is taken to the pressure of enclosed air)

$$\chi = S_r$$

Moisture swelling: The shortcomings of the effective stress theory can be compensated in ABAQUS by a correction called "moisture swelling". This procedure changes the volumetric strain ε_v by adding a strain that can be made a function of the degree of saturation S_r :

$$\Delta\varepsilon_v = f(S_r) = \ln(p_0/p) \cdot \kappa / (1 + e_0) \quad (5-27)$$

$$p = p_{tot} - u_w \cdot S_r \quad (5-28)$$

where

ε_v = volumetric strain

p_0 = initial effective stress taken from the initial conditions

p = actual effective stress

κ = porous bulk modulus (from Equation 5-25)

e_0 = initial void ratio

p_{tot} = actual total stress

u_w = pore water pressure

S_r = degree of water saturation

The moisture swelling relation (*M.S.*) that is needed as input is the logarithmic volumetric strain according to Equation 5-29 where $\Delta\varepsilon_v$ is taken from Equation 5-27.

$$M.S. = \ln(1 + \Delta\varepsilon_v) \quad (5-29)$$

The data for the *moisture swelling procedure* is derived from the assumption that the relation between total stress and degree of saturation of a confined sample (constant volume) is assumed to be linear when the degree of saturation is increased from its initial

value to 100%. During an increase in degree of saturation from the initial value 61% to 100% the total pressure thus increases from 0 to 8 MPa.

M.S. as a function of degree of saturation is shown in Figure 5.4 together with a verification calculation, which simulates an increased degree of saturation of a confined sample. The calculation confirms that the swelling pressure increases linearly with increasing degree of saturation to the final swelling pressure 8 MPa.

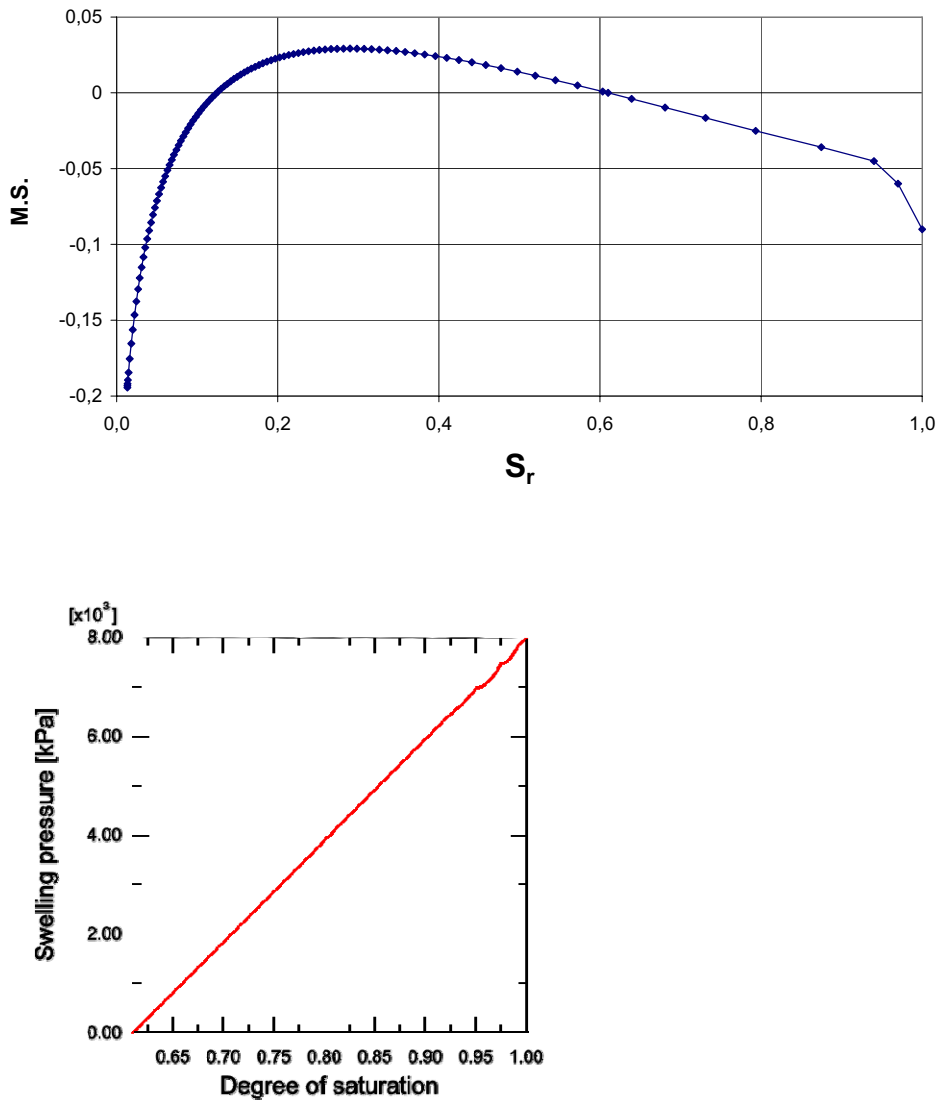


Figure 5.4. Moisture swelling function (top) and verification calculation (bottom).

5.4.3 Canister

The canister is modelled to be made of solid steel with elastic properties $E = 2.1 \cdot 10^8$ kPa, $\nu = 0.3$ and density = 7 850 kg/m³. The heat generation is $P_i = 1139/4$ W as start value and the decay according to the given specifications (see Figure 1-13). The heat is

generated as W/m^3 and since only a quarter of the canister is modelled the total power in the model will correspond to that volume.

5.4.4 Rock

The basic rock properties were given in the specifications and are shown in Table 5-5.

Table 5-5. Basic rock properties

Property	Value
Thermal conductivity ($W/m^{\circ}C$)	3.0
Specific heat ($kJ/kg^{\circ}C$)	0.845
Density (kg/m^3)	2650
Young's modulus (GPa)	60
Poisson's ratio	0.25
Coefficient of thermal expansion ($10^{-6}/^{\circ}C$)	10

The hydraulic properties are rather complicated. They are given as a function of depth, void ratio and degree of saturation and for the unsaturated case there is a retention curve given.

The given transmissivity values have been transformed to hydraulic conductivity for 7 different layers. Table 5-6 shows the variation in hydraulic conductivity with depth.

Table 5-6. Variation in hydraulic conductivity with depth

Layer	Depth (m)	Hydr. cond. $K(m/s)$
1	0-10	$1.0 \cdot 10^{-7}$
2	10-70	$7.0 \cdot 10^{-8}$
3	70-150	$8.0 \cdot 10^{-10}$
4	150-300	$7.0 \cdot 10^{-11}$
5	300-500	$3.0 \cdot 10^{-11}$
6	500-700	$7.0 \cdot 10^{-12}$
7	>700	$1.0 \cdot 10^{-12}$

The hydraulic conductivity is modelled to be constant for all levels except for at repository level at layer 6, where influence in void ratio and degree of saturation has been taken into account. Figure 5.5 shows the given relation between permeability and porosity and Figure 5.6 the same relation transformed to hydraulic conductivity and void ratio. The relation in Figure 5.6 yields $K=7.0 \cdot 10^{-12}$ m/s at $e=0.00311$, which is the base for choosing that value as initial void ratio.

The influence of the degree of saturation on the hydraulic conductivity is described by Equations 5-30 and 5-31 (Thomas et al., 2002). The relation is plotted in Figure 5.7.

$$K(S_r) = K_r \cdot K(S_r=1) \quad (5-30)$$

$$K_r = \sqrt{S_r} \left(1 - \left(1 - S_r^{3.03} \right)^{0.33} \right)^2 \quad (5-31)$$

The retention curve used for the rock is shown in Figure 5.8 (see Thomas et al., 2002).

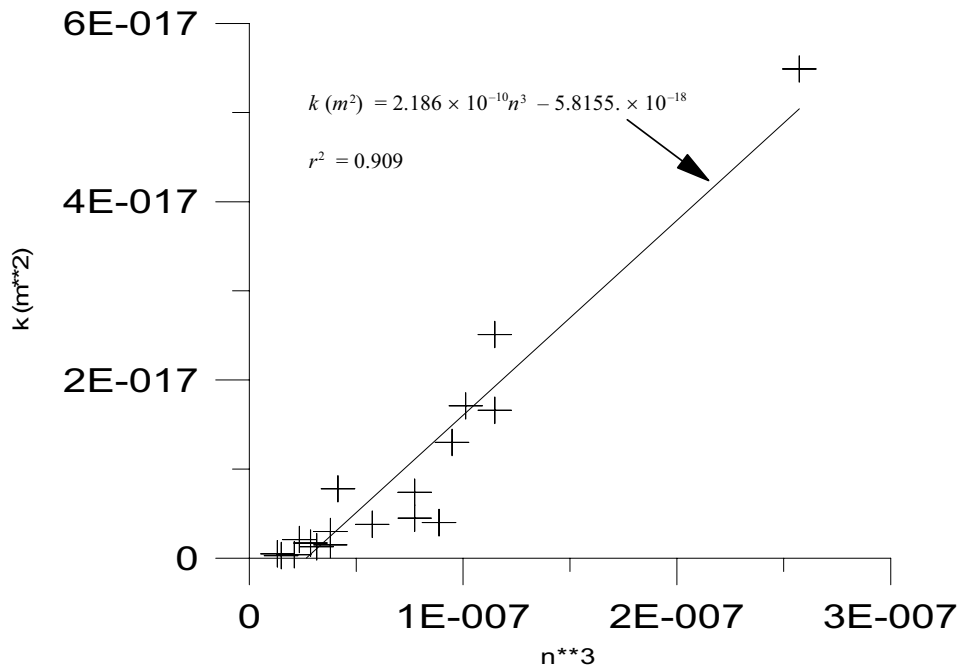


Figure 5.5. Given relation between permeability and porosity of the rock

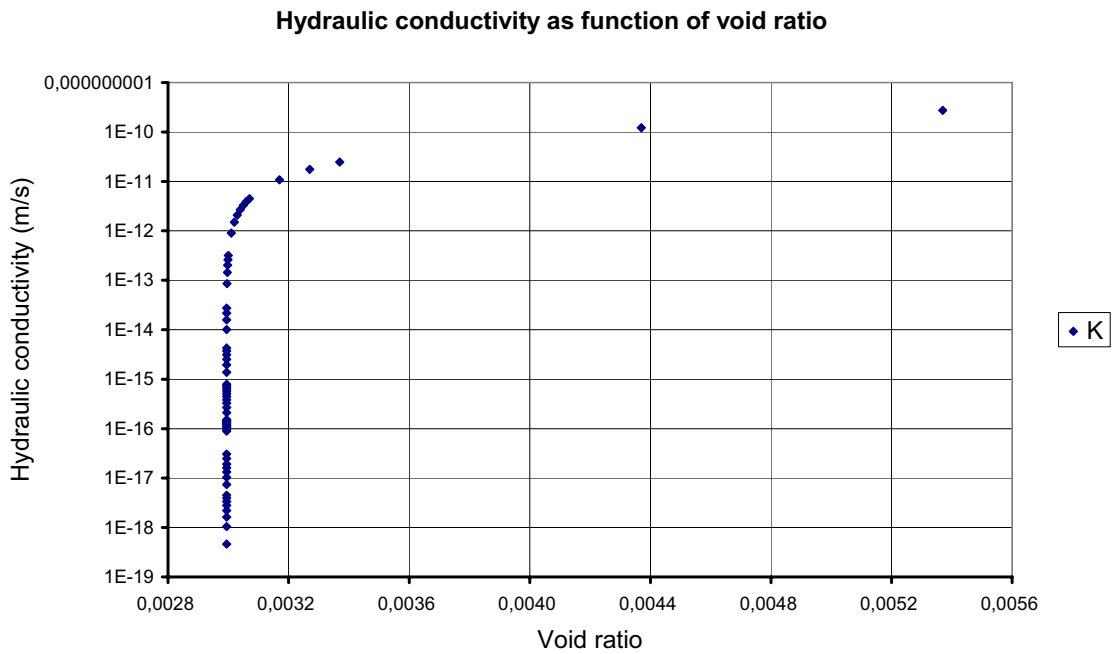


Figure 5.6. Used relation between hydraulic conductivity and void ratio together with the initial void ratio $e=0.00311$.

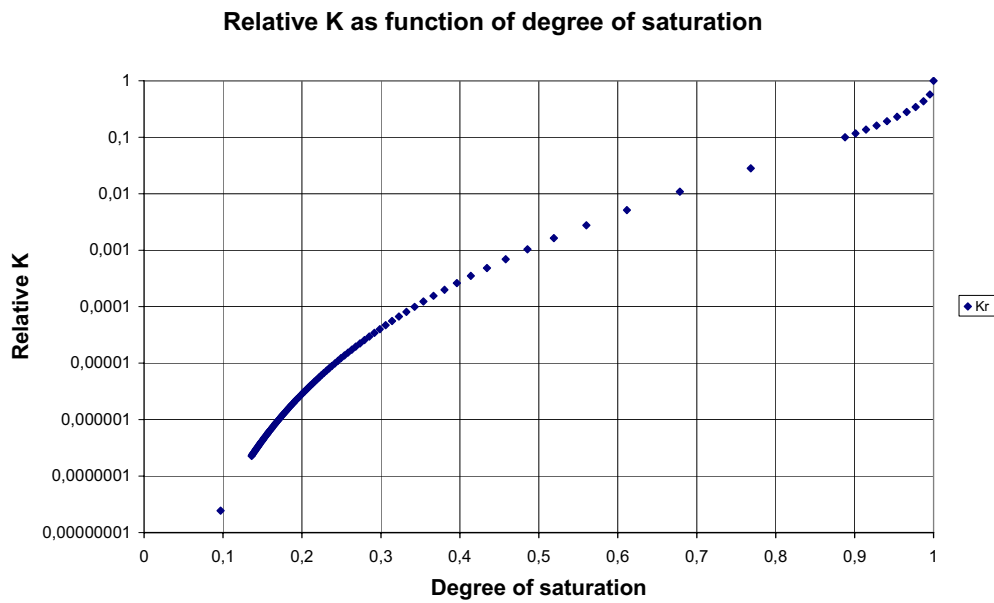


Figure 5.7. Influence of degree of saturation on the relative hydraulic conductivity (Equation 5-31).

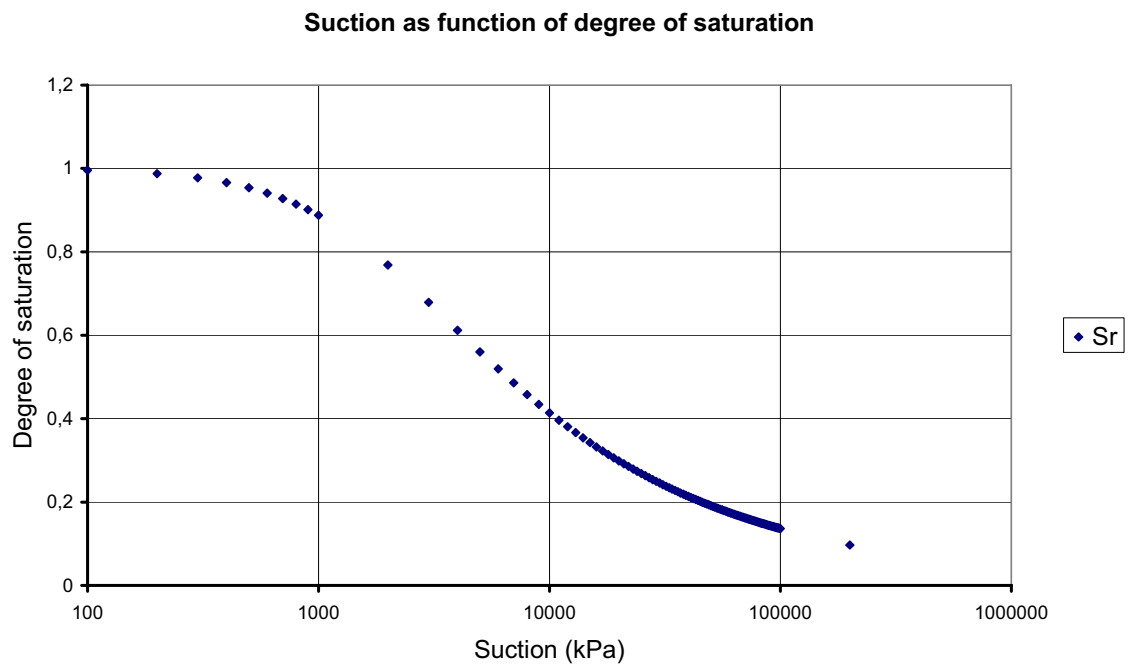


Figure 5.8. Retention curve of the rock.

The rock stresses are rather anisotropic. The following stresses were given for the actual depths and have been used in the calculations:

$$\sigma_1' = 0.00866 \text{ MPa} / m_{depth} + 56.3 \text{ MPa} \quad \text{from 300 m to 1 400m}$$

$$\sigma_2' = 0.00866 \text{ MPa} / m_{depth} + 40.7 \text{ MPa} \quad \text{from 300 m to 1 660m}$$

$$\sigma_3' = \sigma_v = 0.0260 \text{ MPa} / m_{depth}$$

The stresses have been applied as effective stresses according to Terzaghi's theory. The tunnel axis is located parallel to the direction of the intermediate major stresses σ_2 .

Hoek and Brown's failure criterion according to Equation 5-32 has been used.

$$\sigma'_{1f} = \sigma'_{3f} + \left(m \cdot \sigma'_c \cdot \sigma'_{3f} + s \cdot (\sigma'_c)^2 \right)^{1/2} \quad (5-32)$$

with $\sigma'_c = 100 \text{ MPa}$, $m = 16.6$ and $s = 1$, respectively. All stresses are effective stresses.

The factor of safety S_f has been evaluated according to Equation 5-33.

$$S_f = \sigma'_{1f} / \sigma'_{1a} \quad (5-33)$$

where σ'_{1f} = major principle effective stress at failure and σ'_{1a} = actual principle effective stress, respectively.

5.5 Modelling approach and boundary conditions

The calculation has been done in several steps in order to simulate the steady state situation before excavation, the 30 years period after excavation, the installation of buffer and canisters and the period of 1000 years after installation with the thermal pulse.

5.5.1 Initial conditions

The initial values of the variables need to be defined.

The initial *temperature* applied in the rock, buffer and canister is a linear variation with depth between $T=5.0^\circ\text{C}$ at the ground surface and $T=20.77^\circ\text{C}$ at the depth 1 314 m.

The initial *pore water pressure* applied in the rock is hydrostatic pressure from the ground surface, while the buffer has an initial negative pore pressure of $u=-30\,786 \text{ kPa}$ taken from the retention curve at the initial degree of saturation.

The initial *void ratios* are $e=0.00311$ for the rock and $e=0.77$ for the buffer.

The initial *degrees of saturation* are $S_r=1.0$ for the rock and $S_r=0.61$ for the buffer.

The initial *effective stress* of the rock was defined in chapter 5.4.4. For the buffer it is determined as $\sigma'=-u \cdot S_r=18\,779 \text{ kPa}$

5.5.3 Boundary conditions

The conditions at the boundaries are defined in this section. Some boundary conditions are changed or lost at the installation of the buffer after 30 years.

a) Hydraulic boundary conditions

- Ground surface: $u=0 \text{ kPa}$

- Lower boundary: $u=12.9$ MPa (corresponding to hydrostatic pressure)
- Vertical boundaries: No flow (symmetry planes)
- Tunnel surface: $u=-93$ MPa during 30 years then coupled to the buffer.

b) Mechanical boundary conditions

- Ground surface: Free
- Lower boundary: Fixed
- Vertical boundaries: Horizontally fixed and vertically free (symmetry planes)
- Tunnel surface: Free during 30 years then coupled to the buffer.

In addition there are the initial in situ stresses according to chapter 5.4.4.

c) Thermal boundary conditions

- Ground surface: 5.0°C
- Lower boundary: 20.77°C
- Vertical boundaries: No thermal flux (symmetry planes)
- Tunnel surface: Isolated (no flux) during 30 years then coupled to the buffer.

5.5.4 Calculation sequence

Five major steps can be identified for the entire 1000 years simulation.

1. Initial step for establishing equilibrium before excavation. Hydro-mechanical calculation.
 - a. Apply mechanical boundary conditions for the rock
 - b. Apply hydraulic boundary conditions for the rock
 - c. Apply gravity
 - d. Apply temperature: Linear variation with depth between 5.0°C and 20.77°C
2. Time 0. Excavation of the tunnel
 - a. Eliminate tunnel elements
 - b. Apply RH=50% in the tunnel ($u=-93\ 000$ kPa)
3. Time 0-30 years
 - a. Transient HM-calculation
4. Time 30 years
 - a. Install canister and buffer
 - b. Tie buffer nodes to the rock
 - c. Apply initial thermal load
5. Time 30-1000 years
 - a. Transient THM-calculation
 - b. Heat decay of the canister

The thermal calculation is coupled to the hydro-mechanical calculation with the staggered technique described in Figure 5.1.

5.6 Primary results

Results of temperature, pore water pressure, water content, degree of saturation, void ratio, total stress, hydraulic conductivity of the rock and the safety factor of the rock will be presented.

a) Temperature

The evolution of the temperature in mainly the rock is illustrated in Figure 5.9 in two sections. History plots of the temperature in the nodal points in a horizontal section between the canister and the outer rock symmetry boundary are shown as well as the temperature distribution along the vertical path at the outer rock symmetry boundary at different times.

Figure 5.9 shows that the temperature half-way between the tunnels is 35 °C and still increasing after 1000 years. The results also show that the maximum temperature in the canister is about 58 °C and is reached about 10 years after installation. The temperature distribution in the buffer after about 11 years is illustrated in Figure 5.10.

The temperature evolution in the requested points (see chapter 1.5) is shown in Figure 5.11.

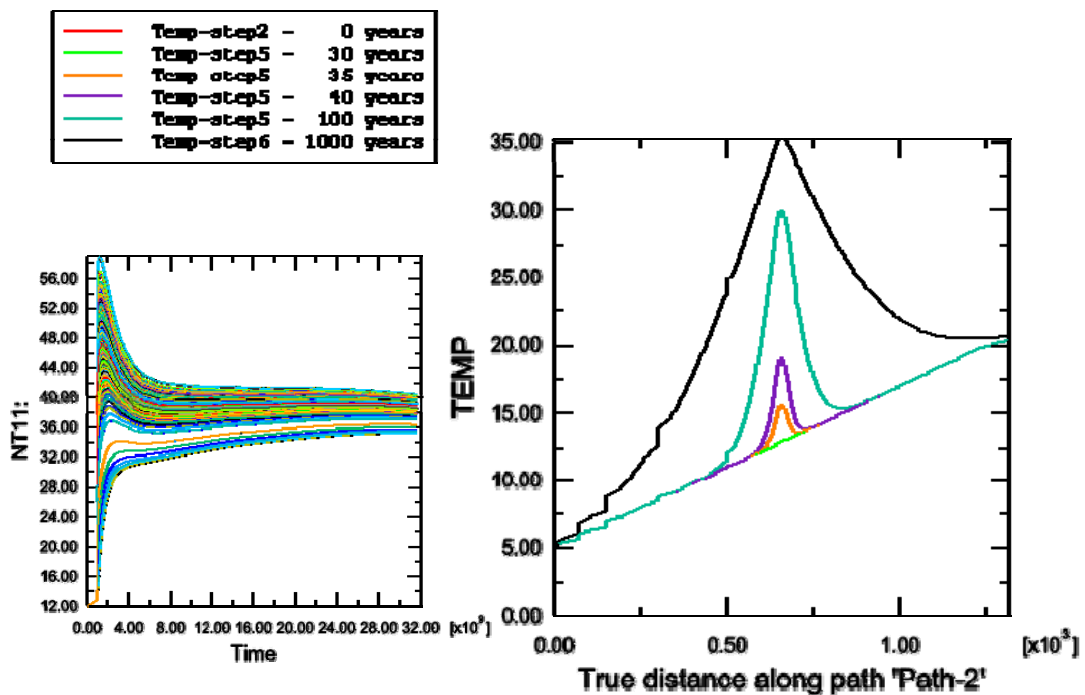


Figure 5.9. Illustration of the temperature evolution in two sections. Left picture: Temperature (°C) as function of time (s) in the nodal points along the horizontal section between the canister and the outer rock boundary. Right picture: Temperature (°C) distribution along the vertical path (m from ground surface) at the outer rock symmetry boundary at different times (after tunnel excavation).

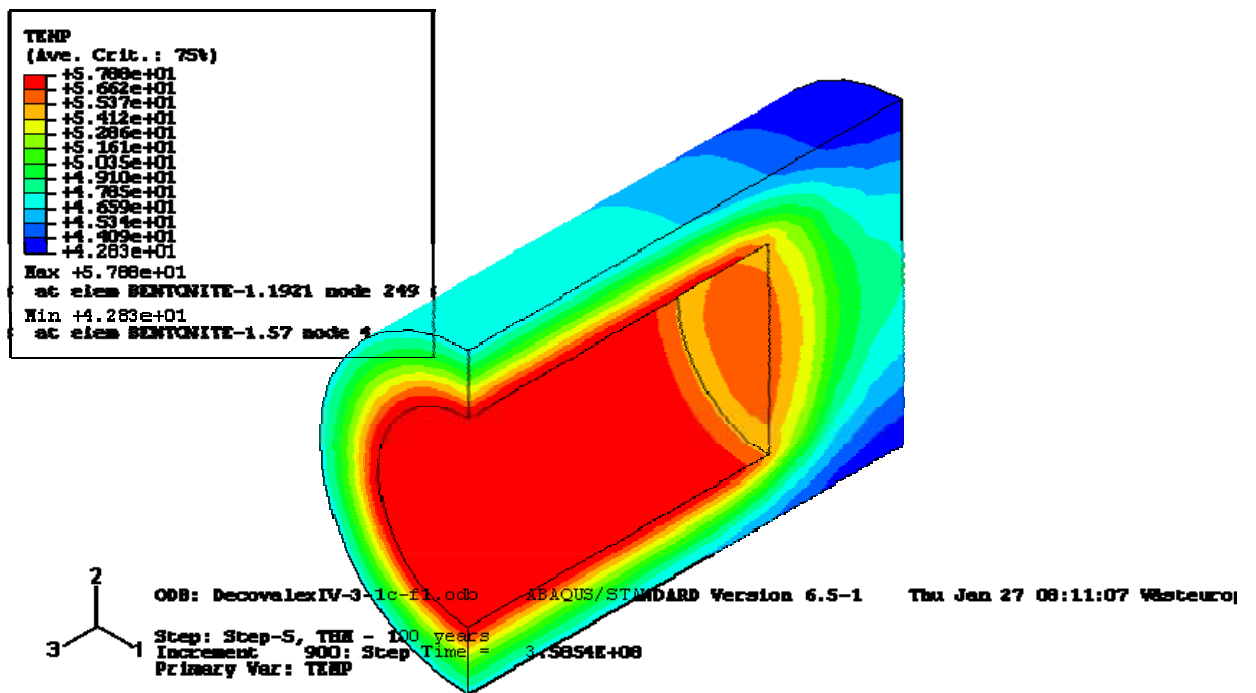


Figure 5.10. Temperature distribution in the buffer about 11 years after installation

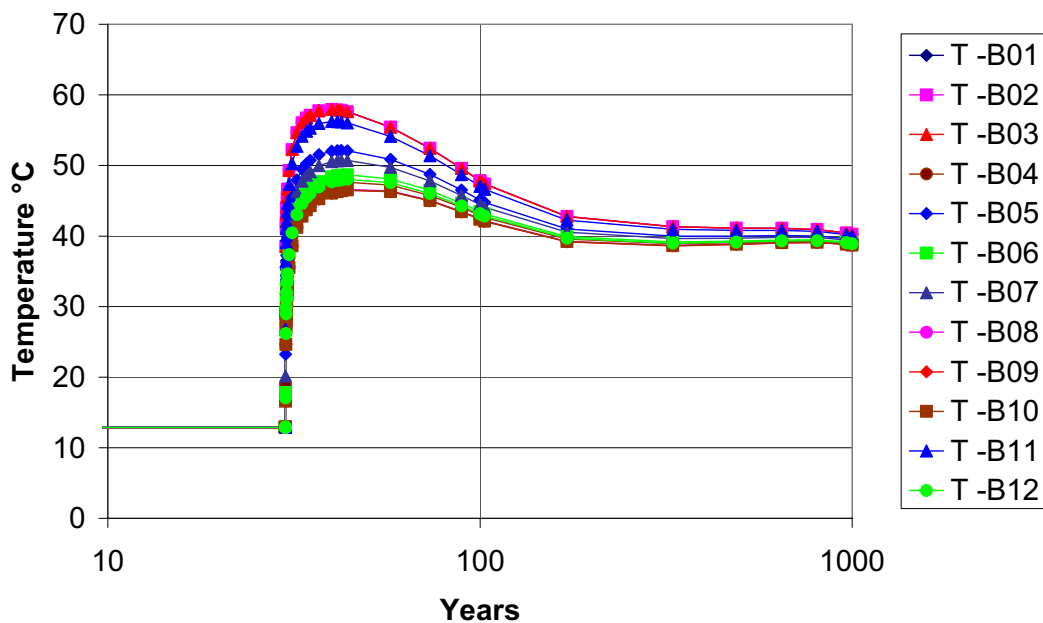


Figure 5.11. Temperature evolution in requested points. The additional point B11 is located in the tunnel axis on the lid of the canister and point B12 is located in the tunnel axis half-way between the canisters.

b) Pore water pressure

The pore water pressure distribution along a vertical line through the entire rock and the tunnel at different times is shown in Figure 5.12. The figure shows the ground water drawdown 30 years after tunnel excavation and the fast recovery. After 1000 years there is a pressure bulb below the tunnel, which is caused by the heating in combination with the low hydraulic conductivity of that rock.

The pore water pressure evolution during the first 100 years in a number of points in the rock is illustrated in Figure 5.13. The figure shows the pore pressure decrease in the rock during the 30 years the tunnel was left open resulting in a de-saturation of the rock close to the tunnel. It also shows the fast recovery that is completed 30-40 years after the buffer installation.

Finally Figure 5.14 shows the pore water pressure distribution in the rock at different times. The figures show a strong difference in behaviour above and below the tunnel in comparison with at the side. This difference is caused by the difference in stresses which causes a difference in void ratio and hydraulic conductivity as shown later. The dark blue colour that represents negative pore water pressure shows how the negative water pressure changes with time. The pore water pressure is still negative at the floor and roof of the tunnel after 5 years due to that the buffer is not fully saturated at that time.

c) Water content

History plots of the water content in requested points in the buffer are shown in Figure 5.15.

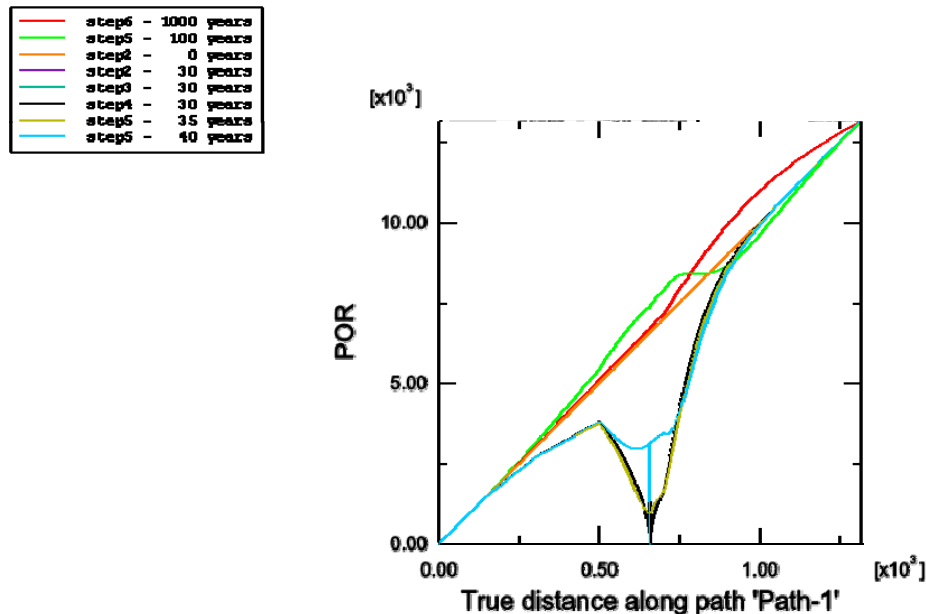


Figure 5.12. Pore pressure (kPa) as a function of the distance from ground surface (m) along a vertical path intersecting the centre of the tunnel at different times (after tunnel excavation).

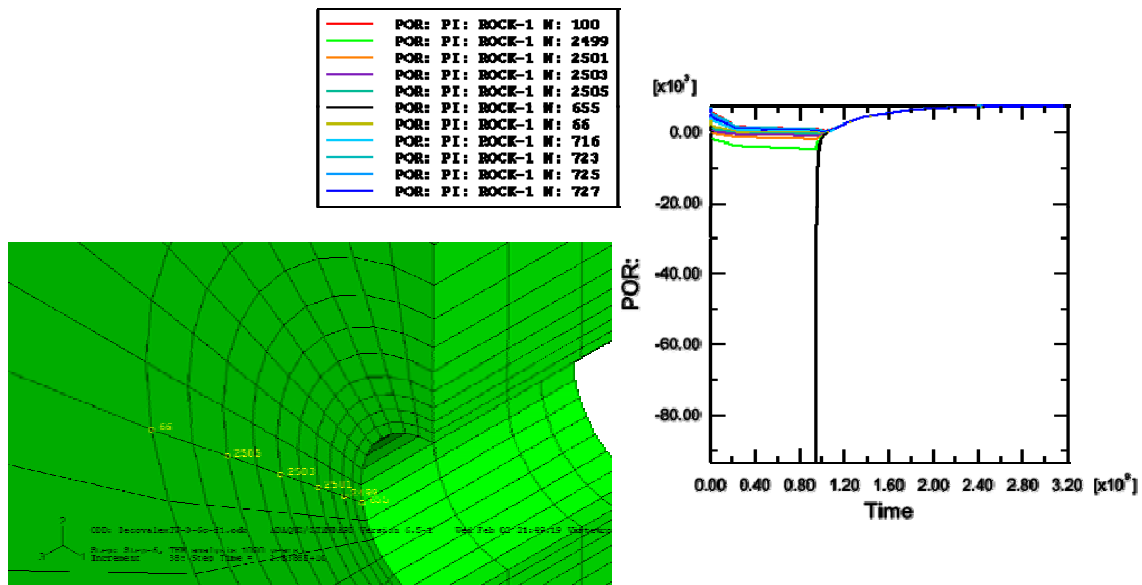


Figure 5.13. Pore water pressure (kPa) evolution during the first 100 years in a number of points in the rock located at different horizontal distances from the tunnel wall according to the left figure (time in seconds).

d) Degree of saturation

The evolution of the degree of water saturation during the first 100 years in a number of points in the rock is illustrated in Figure 5.16. The figure shows the de-saturation of the rock close to the tunnel. It also shows the fast re-saturation that is completed within a few years after the buffer installation.

Figure 5.17 shows the degree of saturation in the buffer at two times. These figures clearly show the inhomogeneous wetting that takes place due to the low hydraulic conductivity in the rock above and below the tunnel.

e) Void ratio

The models permit changes in void ratio caused by the changes in effective stress. Figure 5.18 shows examples of void ratio distribution in the rock and the buffer 5 years after installation. Reduced void ratio above and below the tunnel and increased void ratio at the side of the tunnel caused by the stress concentrations are developed. In the buffer the drying at the end of the canister and corresponding wetting at the rock surface causes rather large changes in void ratio varying from 0.72 at the driest point to 0.82 at the wettest.

f) Total stress

Evolution of total stresses in the buffer was requested for 10 points. Figure 5.19 shows the results in those points together with the two additional points. There is a peak stress after about 100 years, which is an effect of a pore water pressure higher than the

hydrostatic caused by the temperature in the rock. After 1000 years this overpressure has dissipated in the tunnel but not below the tunnel (see Figure 5.12).

The increased temperature also effects the stresses in the near-field rock as illustrated in Figure 5.20 showing the total average stress in the rock just before installation of the buffer and canister and 70 years later. The average stress is about two times higher after 70 years.

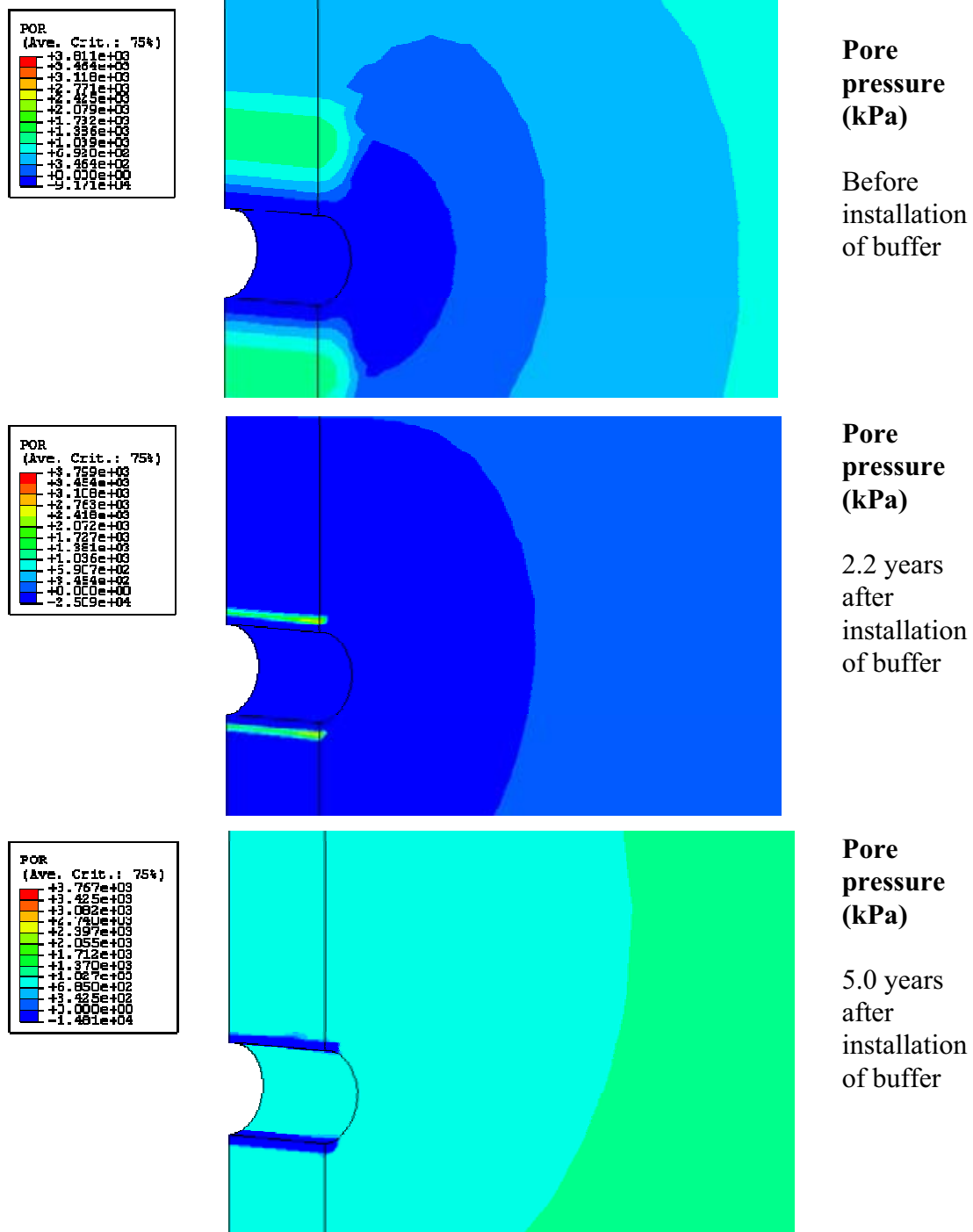


Figure 5.14. Pore pressure (kPa) in the rock at different times after installation of the buffer. The darkest blue represents negative pore pressure.

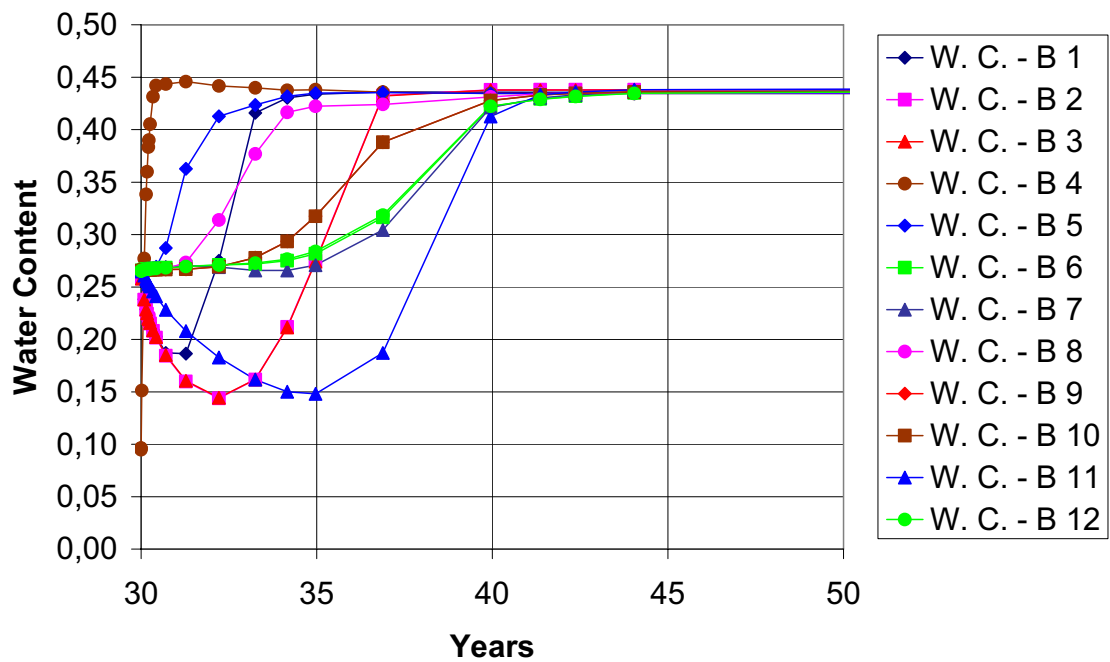


Figure 5.15. Evolution of volumetric water content in the buffer in requested points. The additional point B11 is located in the tunnel axis on the lid of the canister and point B12 is located in the tunnel axis half-way between the canisters.

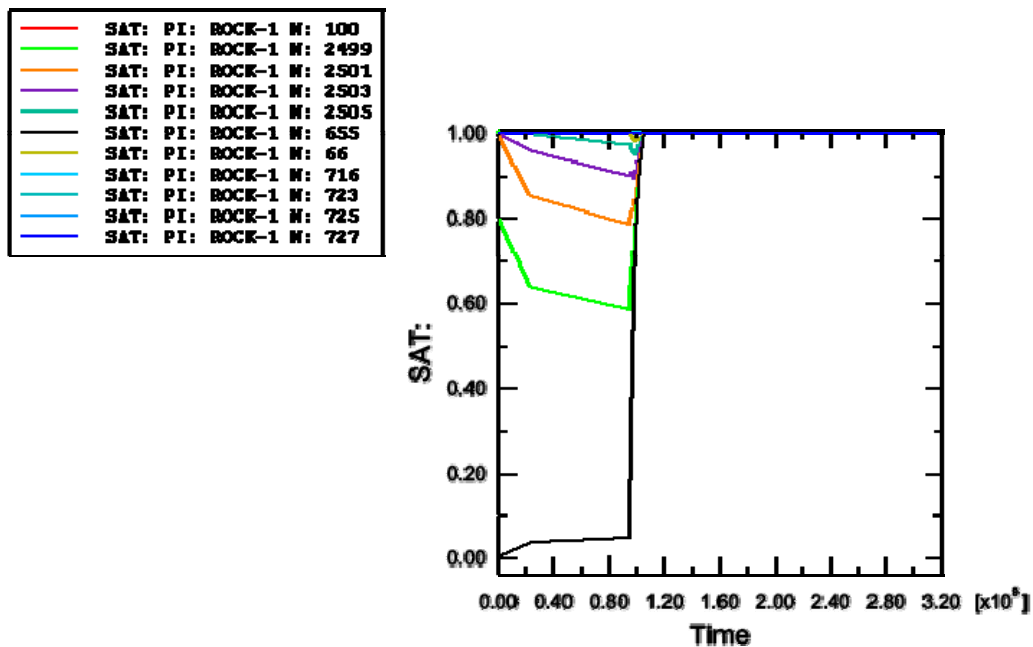
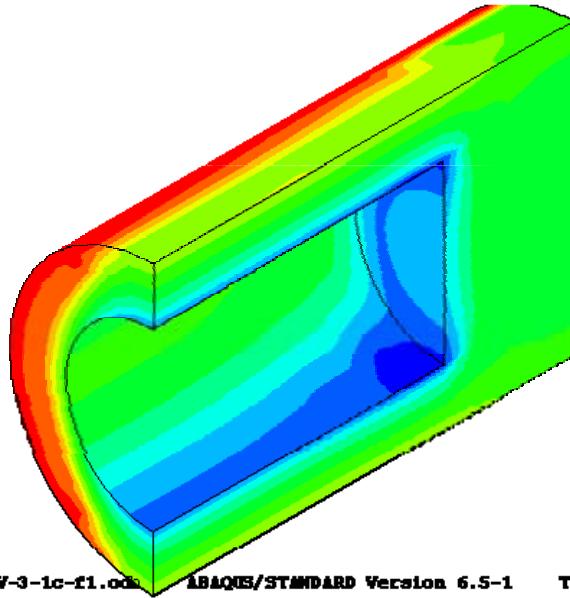
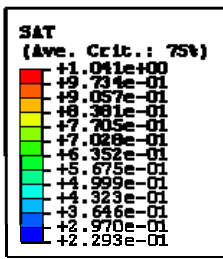
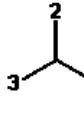
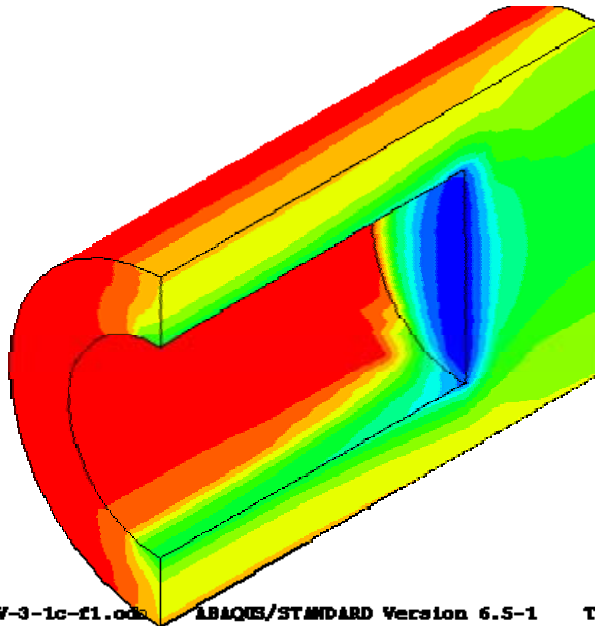
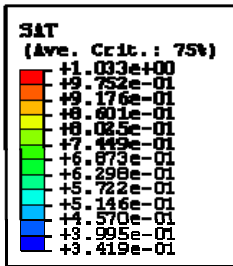


Figure 5.16. Evolution of degree of saturation during the first 100 years in a number of points in the rock located at different horizontal distances from the tunnel wall (time in seconds. See Figure 5.13).




 ODB: DecovaLexIV-3-1c-f1.odb ABAQUS/STANDARD Version 6.5-1 Thu
 Step: Step-5, TRN - 100 years
 Increment: 600: Step Time = 6.9838E+07
 Primary Var: SAT




 ODB: DecovaLexIV-3-1c-f1.odb ABAQUS/STANDARD Version 6.5-1 Thu
 Step: Step-5, TRN - 100 years
 Increment: 750: Step Time = 1.5667E+08
 Primary Var: SAT

Figure 5.17. Degree of saturation in the buffer 2.2 years (top) and 5.0 years after installation (bottom). The two red colours denote more than about 90% degree of saturation while the five blue colours denote drying from the initial state.

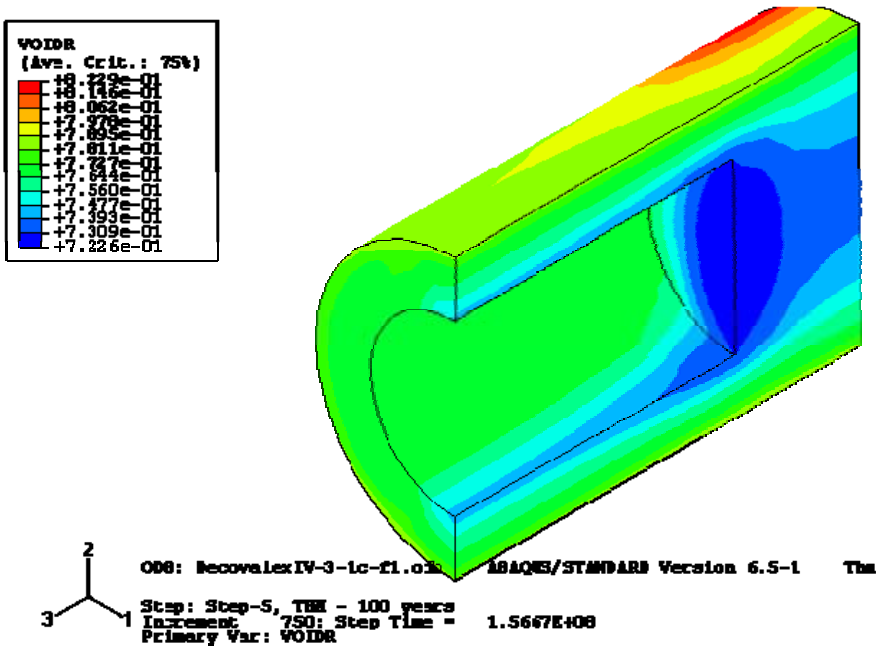
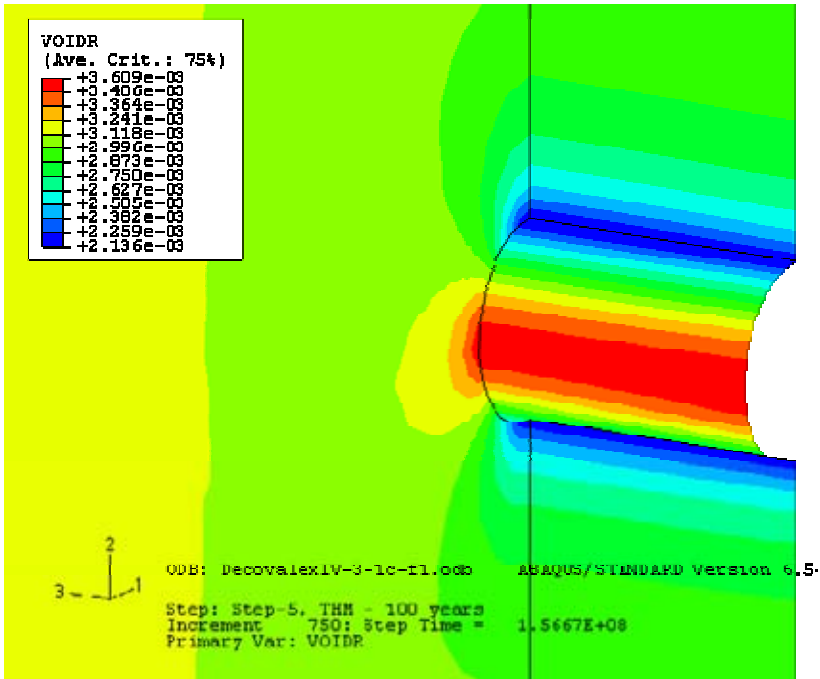


Figure 5.18. Void ratio in the rock and buffer 5 years after installation of the buffer (top) and canister (bottom)

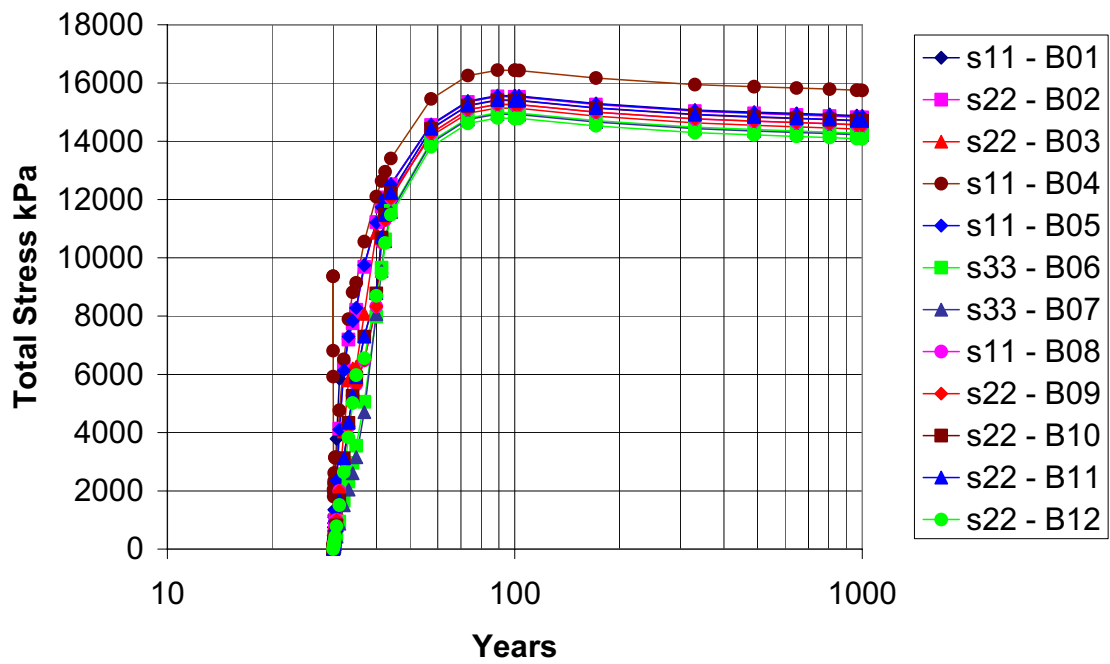


Figure 5.19. Evolution of total stresses in requested points in the buffer.

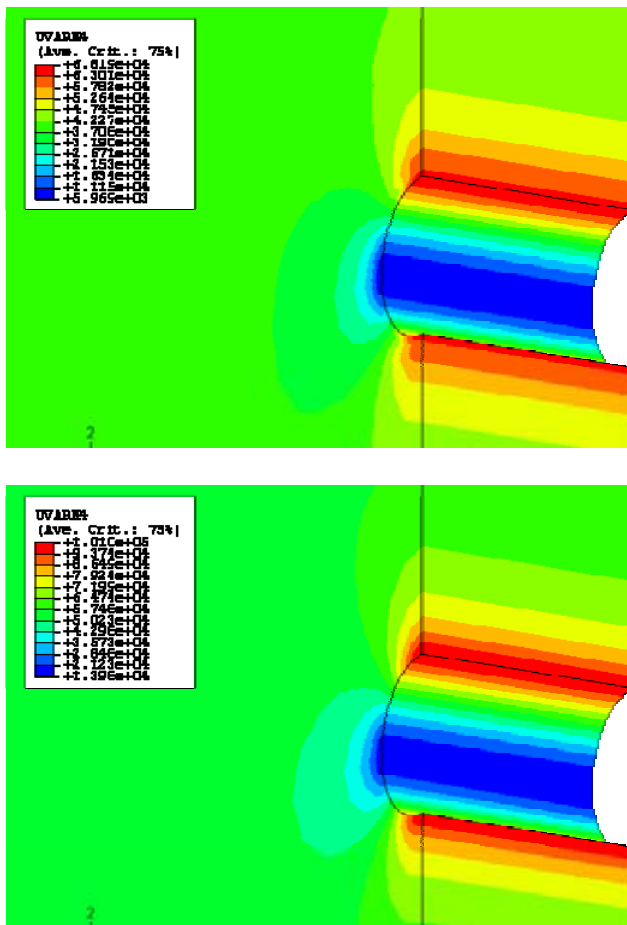


Figure 5.20. Total average stress (kPa) in the near-field rock before installation of the buffer (top) and 70 years after (bottom).

g) Hydraulic conductivity

The hydraulic conductivity of the rock is affected by both changes in degree of saturation and void ratio as described in chapter 5.4.4. Since the near field rock around the tunnel is subjected to stress concentrations due to the excavation, drying due to the low RH in the tunnel and thermal expansion and resulting stress changes due to the generated heat, it is obvious that the resulting hydraulic conductivity may change dramatically during the studied 1000 years of the repository life time.

Figure 5.21 shows the distribution of the hydraulic conductivity value in the near field rock at three different points of time. After excavation but before installation of the buffer the hydraulic conductivity is strongly reduced from the original value $K=7 \cdot 10^{-12}$ m/s to below $K=1 \cdot 10^{-13}$ m/s around the entire tunnel due to stress concentrations and drying. After installation of the buffer and canister the hydraulic conductivity remains below $K=1 \cdot 10^{-13}$ m/s above and under the tunnel in a zone with increased depth, but at the side of the tunnel the hydraulic conductivity increases to above $K=1 \cdot 10^{-11}$ m/s in a zone that reaches about 1 m into the rock wall.

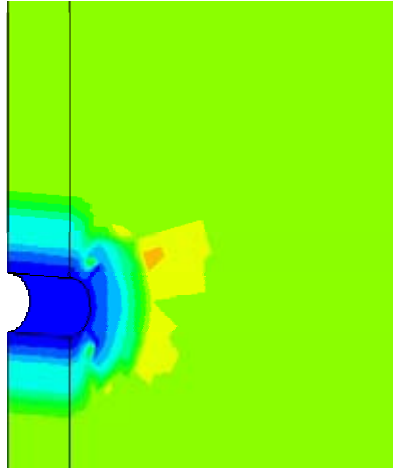
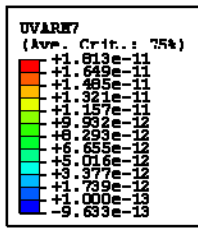
h) Factor of safety

The factor of safety of rock failure, defined according to Equations 5-32 and 5-33, is shown in Figure 5.22 at three different times. The safety margin is good just before installation of the buffer and canister with the lowest factor 1.3 located at the roof and floor of the tunnel, while the safety factor is very large (about 3) at the wall. 10 years after installation the factor has decreased to below 1.0 both in the floor, roof and in the walls. After 70 years the safety factor is clearly below 1.0 especially in the wall where it is even negative. The reason for this very strong reduction in safety in the wall is not quite clear, but the void ratio is increased in this region at that time indicating that tension stresses occur.

5.7 Summary and conclusions

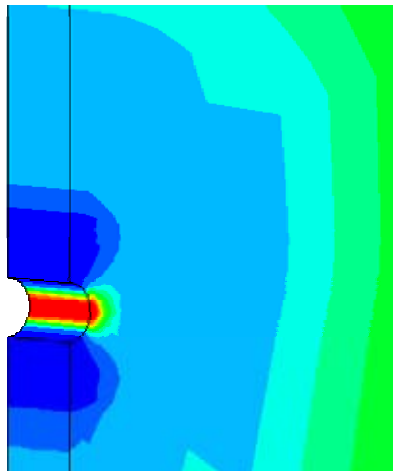
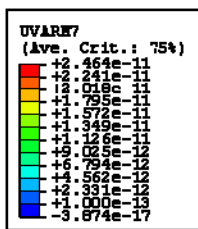
A fully coupled THM modeling of the first 1000 years of a repository lifetime has been performed with the finite element code ABAQUS. The excavation of the tunnels in the rock, the installation of canisters and buffer and the evolution of temperature, degree of saturation, water pressure and mechanical response in the rock and buffer have been simulated. The following primary results and conclusions were reached:

- The maximum temperature in the canister is only 58 °C and is reached after about 10 years.
- The temperature half-way between the tunnels is 35 °C and still increases after 1000 years.
- The drawdown of the pore water pressure disappears 30-40 years after installation of the buffer.
- After 1000 years there is a pore water overpressure beneath the tunnels due to the increased temperature and low hydraulic conductivity of that rock.



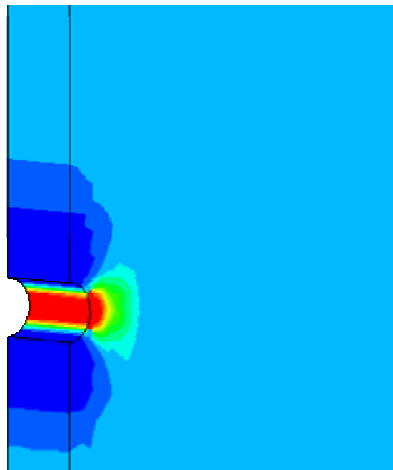
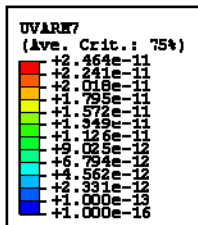
K (m/s)

Before installation of buffer



K (m/s)

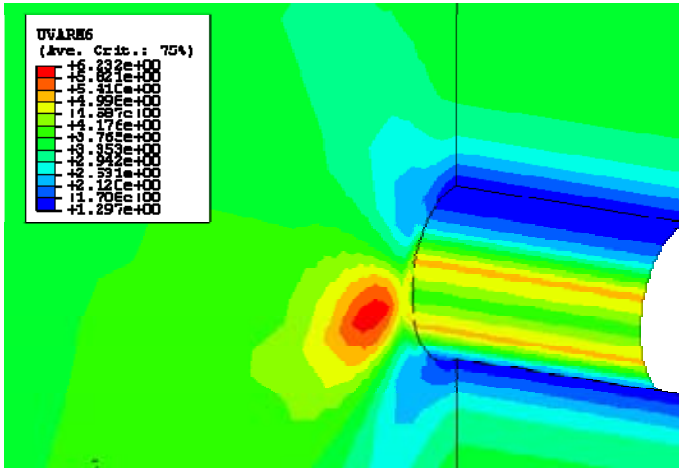
10 years after installation of buffer



K (m/s)

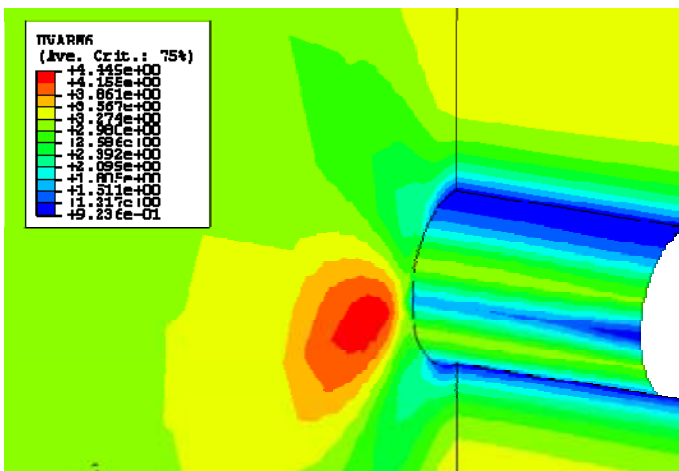
70 years after installation of buffer

Figure 5.21. Hydraulic conductivity in the rock at different times. Dark blue represents very low hydraulic conductivity ($<10^{-13}$ m/s)



S_f

*Before
installation of
buffer*



S_f

- The rock is desaturated before installation of the buffer but will be rather quickly resaturated after installation.
- The buffer is inhomogeneously wetted after installation due to the changed hydraulic conductivity of the rock that is caused by the rock stress redistribution.
- The total average stress in the rock is very inhomogeneous around the tunnel and is almost doubled 70 years after installation compared to just before installation of the buffer due to the temperature increase.
- The hydraulic conductivity of the rock is strongly changed during the first 100 years since it is affected both by changes in degree of saturation and changes in void ratio. The hydraulic conductivity increases in the walls of the tunnel while it is strongly reduced at the roof and floor.
- The safety factor of the rock is well above 1.0 before installation of the canisters and buffer but 10 years after installation the factor decreases to below 1.0 both in the floor, roof and in the walls. After 70 years the safety factor is clearly below 1.0 especially in the wall where it becomes even negative.
- The hydraulic behaviour is dominated by the rather strange dramatic reduction in hydraulic conductivity of the rock at a decrease in void ratio from the initial value 0.00311 to 0.003.

References

- ABAQUS Inc. *ABAQUS manuals*. 2005
- Börgesson, L. and Hernelind, J., *Coupled thermo-hydro-mechanical calculations of the water saturation phase of a KBS3 deposition hole – influence of hydraulic rock properties on the water saturation phase*. SKB TR-99-41. 1999.
- Börgesson, L, Johannesson, L.-E., Sandén, T. and Hernelind, J., *Modelling of the physical behaviour of water saturated clay barriers. Laboratory tests, material models and finite element application*. SKB Technical Report TR 95-20, SKB, Stockholm. 1995.
- Thomas, H.R., Cleall, P.J. and Mitchell, H.P. *Comparison of physical measurements and a finite element numerical simulation of water uptake and distribution in the isothermal test*. OPG report 0818-REP-01300-10042-R00, OPG, NWMD, 700 University Av. Toronto, Canada, M5G 1X6. 2002.

6. Report of Task A-1:Preliminary THM analysis of the near field

Masakazu Chijimatsu, *Hazama Corporation, Japan*

Tomoo Fujita, *Japan Atomic Energy Agency, Japan*

6.1 Introduction

The objective of Task A of DECOVALEX-THMC is to assess the implications of coupled THM processes in the near field of a typical repository on long term repository performance. This is intended to replicate an actual working example where the engineering experts would work in collaboration and interact with performance/safety analysts and experimentalists on a realistic case study of a repository. The proposed work is an example of integration of model development/calibration and interpretation of laboratory and in-situ data towards the final goal of building confidence to the PA process. Several Research Teams within the DEOCALEX-THMC will analyze the problem using various conceptual and numerical approaches. The repository we consider is a hypothetical repository in crystalline rocks. The geological setting, the physical characteristics of the spent fuel, engineered barriers and host rock, as well as the geometrical configuration of the repository are given detailed in Chapter 1.

This chapter presents the modeling results by the JAEA Research Team for Task A-1. As a first step of Task A-1, simple thermal calculation was performed to determine the combination of borehole to borehole and container to container centerline distance that would result in an outside temperature of 100°C for the container. After that, preliminary THM simulation in the near field of the repository was performed. In Task A-1, a linear elastic medium is considered without influences of mechanically induced changes in permeability (e.g. induced by rock damage). Rock damage in the excavation disturbed zone (EDZ) and its effect on permeability and THM evolution will be considered in later stages of Task A.

6.2. Results of the thermal analysis

6.2.1 Introduction

As a first step of Task A-1, simple thermal calculation was performed to determine the combination of borehole to borehole and container to container centerline distance that would result in an outside temperature of 100°C for the container. The borehole to borehole centerline distance varies in a range of 25 to 70 m, and the centerline spacing between containers in a range of 5.6 to 8 m. It is assumed that the bentonite remains at the emplaced water content of 16 %, corresponding to a 60 % degree of saturation. The model geometry for simulation is shown in Figure 6.1 and Table 6.1 shows the points in bentonite where time history curves are requested. Some points are shown in Figure 6.1. Thermal properties of rock mass that are needed for calculation is shown in Table 6.2. Thermal conductivity λ_m and specific heat c of bentonite MX-80 are obtained as functions of degree of saturation as shown in Figure 6.2 and Figure 6.3, and the equations are as follows:

$$\lambda_m = 0.29992 - 0.22103S_r - 1.27634S_r^2 + 16.40662S_r^3 - 23.14611S_r^4 + 8.44418S_r^5 + 0.793S_r^6 \quad (6.1)$$

$$c = \frac{80 + 4.2w}{100 + w} \quad (6.2)$$

In this calculation, the initial degree of saturation of the bentonite is 60 %, and then thermal conductivity and specific heat are as follows,

$$\lambda_m = 0.945 \quad (\text{W/mK}) \quad (6.3)$$

$$c = 1.25 \quad (\text{kJ/kgK}) \quad (6.4)$$

Figure 6.4 shows the heat output per one container as a function of time after the post-closure. In this calculation, we assume that the fuel is disposed 30 years after it comes out of the reactor. Figure 6.5 shows the relationship between time after disposal and heat output, it means that 30 years of the x-axis in Figure 6.4 is zero in Figure 6.5. For calculation, the relationship as shown in Figure 6.6 is used. In this figure, the y-axis is heat output per unit volume.

Figure 6.7 shows the finite element mesh for calculation. Materials considered in

calculation are rock mass, buffer and container. 12 cases as shown in Table 6.3 are performed. Model length along x-axis is 12.5, 20.0, 27.5 and 35.0 m. Model length along y-axis is 2.8, 3.4 and 4.0 m.

6.2.2 Result

Figure 6.8 shows the time history of temperature at the output points in Case 01. Time histories of temperature at points B1, B2 and B3 are almost the same and these points show higher temperature than other points. Maximum temperature at these points is approximately 80°C and it occurs at 25 years after disposal.

Figure 6.9 shows the time history of temperature distribution along the horizontal line ($Y=0$ and $Z=0$) in Case 01. For dozens of years since disposal of waste, only the region around the container experiences a big temperature rise. After that, the temperature around the container decreases, and the temperature in the rock rises. The temperature in the container, the buffer and rock remain constantly high to approximately 10000 years later. After 1000 years, temperature in all points decreases as shown in Figure 6.8. Figure 6.10 shows the time history of temperature distribution along the horizontal line ($X=0$ and $Z=0$) in Case 01. This figure shows the same tendency with Figure 6.9, but the speed of temperature increasing at the end of model along the y-axis ($Y = 2.8\text{m}$) is faster than that at the end of model along the x-axis ($X = -12.5\text{ m}$) in Figure 6.9 because container to container centerline distance is longer than borehole to borehole centerline distance. Figure 6.11 shows the time history of temperature distribution along the vertical line ($X=0$ and $Y=0$). This figure also shows the same tendency with Figure 6.9 and Figure 6.10. In other words, temperature only around the container suddenly rises in the early times, and temperature in rock rises with decrease of temperature around the container. And then temperature decreases in all parts at the same time. Figure 6.12 is a close-up of the part of $-5.0\text{m} < Z < 5.0\text{m}$ in Figure 6.11. Until approximately 100 years after disposal of waste, high temperature remains in the center of container. However, the temperature distribution becomes flat after that time.

Figure 6.13 shows the relationship between maximum temperature in the buffer and time when the temperature is maximal. Temperature in Case 01 is the highest in all cases and it is approximately 80°C. Temperature in Case 12 is the lowest in all cases and it is approximately 60°C. It is also shown that a long time is needed to reach the maximum temperature so that the highest temperature in the buffer is high. Time when the temperature is maximal in Case 01 is approximately 25 years, and it is approximately 5 years in Case 12. Figure 6.14 shows the relationship between occupied area (disposal-tunnel spacing \times the container pitch) and maximum temperature. The maximum temperature in the buffer becomes low when the occupied area becomes large,

but a ratio of reduction becomes small if occupied area grows more than 300m^2 . Figure 6.15 shows the relationship between the disposal-tunnel spacing (X) and the maximum temperature in the buffer. When the disposal-tunnel spacing (X) is the same, the maximum temperature in the buffer becomes small so that the container pitch (Y) is large. Temperature change from $X=25\text{ m}$ to $X=40\text{m}$ is large but after that temperature decreasing rate is small. Figure 6.16 shows the relationship between the container pitch (Y) and the maximum temperature in the buffer. In Figure 6.15, it is shown that temperature decreasing rate becomes small when the disposal-tunnel spacing is more than 40 m. However, about the container pitch, the highest temperature becomes a tendency to reduce in a constant ratio with increase of the container pitch by a range of $Y= 5.6\text{ m}$ to 8.0 m . In all cases in this section, maximum temperature in the buffer is under 100°C .

6.3. Result of preliminary THM analysis

6.3.1 Introduction

From the results of thermal analysis, geometry of model for THM analysis is determined as shown in Figure 6.17. In this section, disposal-tunnel spacing is 55 m (27.5m in 1/4 model) and container pitch is 5.6 m (2.8 m in 1/4 model). By using this model, THM analysis is performed. Analysis cases are shown in Table 6.4. In Case-A01, excavation of disposal tunnel is not considered. Engineered barrier is emplaced at first, in other word, water pressure decreasing in rock mass is not considered. In Case-A02 and Case-A03, excavation of disposal tunnel is considered. During excavation of disposal tunnel, temperature and water pressure at element corresponding to the disposal tunnel is fixed at predetermined value as shown in Table 6.4. In Case-A02, relative humidity is fixed at 50%R.H. and it is corresponding to negative pressure -9500m. In Case-A03, disposal tunnel is fixed at atmospheric pressure. Temperature at excavation part is 25°C .

Initial water content of bentonite is 16 %, corresponding to a 60 % degree of saturation. Table 6.5 shows the output points. Properties of rock mass that needs for calculation is shown in Table 6.5. Heat out put from the container is shown in Figure 6.18.

6.3.2 Property of bentonite MX-80

For the simulation of Prototype Repository, SKB carried out many laboratory experiments about the bentonite MX-80 (Borgesson et al., 1994, 1995; Ledsmas and Chen, 2003). The initial conditions of bentonite MX-80 at the laboratory experiments are as follows: dry density: $\rho_d = 1.67 \text{ g/cm}^3$, water content: $\omega = 0.17$, void ratio: $e = 0.77$ and degree of saturation: $S_r = 0.61$.

In this chapter, we show the parameters of materials for simulation by THAMES. Almost all parameters except for the hydraulic conductivity, thermal vapor flow diffusivity and swelling pressure parameter are the same with those used for the simulation conducted by SKB (Borgesson and Hernelind, 1999). Hydraulic conductivity, thermal vapor flow diffusivity and parameter for swelling pressure are the same as those used for the simulation of the Prototype Repository Project by THAMES (Chijimatsu et al., 2003).

a) Thermal property

The thermal conductivity of MX-80 is obtained as a function of degree of saturation S_r . Figure 6.18 shows the measurement result. For the simulation, we used the function as shown in equation (6.5).

$$\lambda_m = 0.29992 - 0.22103S_r - 1.27634S_r^2 + 16.40662S_r^3 - 23.14611S_r^4 + 8.44418S_r^5 + 0.793S_r^6 \quad (6.5)$$

Specific heat c (kJ/kgK) is a function of water content (%) as shown in equation (6.6).

$$(\rho c)_m = \rho_w \frac{80.0 + 4.2w}{100 + w} \quad (6.6)$$

b) Hydraulic property

The hydraulic conductivities (k) of MX-80 are measured with different void ratio (e) under the different temperature (T) conditions. Figure 6.19 shows the example of measurement results. This figure shows the relationship between the void ratio and the hydraulic conductivity. From these experiment results, SKB used the tabulated data shown in Table 6.7 for the simulation. In this table, hydraulic conductivity is a function

of void ratio and temperature. From this table, the relationship between the hydraulic conductivity and temperature at each void ratio is calculated as shown in Figure 6.20. From this figure, it is known that hydraulic conductivity increase with temperature increasing. Therefore, we estimated the intrinsic permeability K (m^2) from the hydraulic conductivity k (m/s) by using the equation (6.7).

$$K = \frac{k\mu}{\rho g} \quad (6.7)$$

where μ (Pa s) is the viscosity of water, ρ (kg/m^3) is the density of water and g (m/s^2) is the gravitational acceleration.

Figure 6.21 shows the relationship between the intrinsic permeability and the temperature at each void ratio. From this figure, it is known that the intrinsic permeability is a function of void ratio. Figure 6.22 shows the relation between the intrinsic permeability and the void ratio. This relationship is expressed in the following equation.

$$K = 1.81 \times 10^{-20} (e)^{4.30} \quad (6.8)$$

For the simulation by THAMES, equation (6.7) is used as the intrinsic permeability, where, e_0 is 0.75, then $K_0 = 5.25 \times 10^{-21} \text{m}^2$.

The unsaturated permeability is defined (Chijimatsu et al., 2003) as shown in equation (6.9). In this equation, the unsaturated permeability is a function of the degree of saturation.

$$k_r = S_r^{2.2} \quad (6.9)$$

Water retention curve is obtained as shown in Figure 6.23 by SKB. For simulation, we use the van Genuchten curve and parameters are as follows (Chijimatsu et al., 2003)

$$S_r = \left\{ 1 + |\alpha \psi|^n \right\}^{-m} \quad (6.10)$$

where,

$$m = 1 - 1/n \quad (6.11)$$

$$\alpha = 5.2 \times 10^{-5} [1/\text{kPa}], n = 1.70 [-] \quad (6.12)$$

The thermal vapor flow diffusivity is determined by temperature gradient test conducted by SKB. Test apparatus is shown in Figure 6.24. The size of specimen is 50mm in diameter and 50mm in height. The temperature of top and bottom side of specimen was controlled at fixed different temperature. After the several time, specimen was picked up and measured the water content distribution in the specimen.

SKB used the equation (6.13), (6.14) and (6.15) as the thermal vapor flow diffusivity. In these equations, the thermal vapor flow diffusivity D_{Tv} is a function of the degree of saturation.

$$D_{Tv} = D_{Tvb} \quad (0.3 < S_r < 0.7) \quad (6.13)$$

$$D_{Tv} = D_{Tvb} \cdot \cos^a \left(\frac{S_r - 0.7}{0.3} \cdot \frac{\pi}{2} \right) \quad (0.7 < S_r) \quad (6.14)$$

$$D_{Tv} = D_{Tvb} \cdot \sin^b \left(\frac{S_r}{0.3} \cdot \frac{\pi}{2} \right) \quad (S_r < 0.3) \quad (6.15)$$

The parameters D_{Tvb} , a and b were determined by back analysis of temperature gradient test as follows.

$$D_{Tvb} = 2.0 \times 10^{-13} \text{ m}^2/\text{s/K} \quad (6.16)$$

$$a = 6 \quad (6.17)$$

$$b = 6 \quad (6.18)$$

c) Mechanical property

The e -log p curve is obtained by oedometer test and volumetric elastic modulus is obtained as follows.

$$\kappa = 0.2 \quad (6.19)$$

The Poisson's ratio is as follows.

$$\nu = 0.4 \quad (6.20)$$

The elastic modulus is

$$E = 3K(1 - 2\nu) = 3(1 + e_0) \frac{P}{\kappa} (1 - 2\nu) \quad (6.21)$$

From equation (6.21), it is known that the elastic modulus depends on confined pressure p . However, because the density change during re-saturation is small, it is assumed that it is the linear elasticity in a minute strain region and the confined pressure is 2.5MPa. Then elastic modulus is 13MPa.

6.3.3 Result

Figure 6.25 shows the temperature distribution along the horizontal line ($Y=0$ and $Z=0$) before and after the excavation of tunnel in Case-A02. Initial temperature at this line is approximately 13 °C. After the excavation, temperature in the rock mass is increased because temperature at the tunnel is fixed at 25 °C. Figure 6.26 shows the water head distribution along the same line. In this case, boundary condition at the tunnel is negative pressure at -9500m that is corresponding to 50%R.H., and then water head in the rock mass near tunnel becomes negative. Figure 6.27 and Figure 6.28 show the water head distribution along the vertical line ($X=0$ and $Y=0$). In the vertical line, negative pressure occurs between -9m to 9m. Figure 6.29 and Figure 6.30 show the temperature distribution along the vertical line. Figure 6.31 to Figure 6.34 show the results after excavation of tunnel in Case-A03. The temperature distribution is not different from that in Case-A02. However the water head distribution is different because the tunnel is fixed at atmospheric pressure. For that reason, negative pressure is not seen in the rock mass and the region that experiences pressure decreases is smaller than Case-A02.

Figure 6.35 and Figure 6.36 show the time history of degree of saturation and temperature after the emplacement of the engineered barrier in Case-A01, respectively. In the buffer, the degree of saturation rises sequentially from the outside that is near to rock, and it is known that the point B13 needs most time to saturate. Re-saturation time is approximately 10 years. The time for maximal temperature is approximately 10 years and the maximum temperature is approximately 60 °C. Figure 6.37 and Figure 6.38 show the time history of degree of saturation and temperature after the emplacement of engineered barrier in Case-A02, respectively. Because the water pressure becomes negative in the rock after the excavation of tunnel in Case-A02 as shown in Figure 6.26, the re-saturation time of the buffer in Case-A02 is longer than that in Case-A01, at approximately 30 years. Because the re-saturation time is longer, the maximum

temperature in the buffer becomes higher in comparison with Case-A01.

Figure 6.39 and Figure 6.40 show the time history of degree of saturation and temperature after the emplacement of engineered barrier in Case-A03, respectively. In this case, decreasing of water pressure is considered but it is not negative, thus the re-saturation time is faster than that in Case-A02. There is not a so big difference in comparison with Case-A01 that does not consider the excavation of tunnel. However, the maximum temperature is higher than that in Case-A01.

Figure 6.41 shows the time history of temperature by thermal analysis. Figure 6.42 shows the relationship between maximum temperature and time when the temperature is maximal in each case. Figure 6.43 shows the relationship between the maximum temperature and the re-saturation time in each case. Re-saturation time varies between 10 and 30 years by effect of excavation of tunnel and the boundary condition of excavation tunnel, but maximum temperature in the buffer does not so much have an influence in each case.

6.3.4 Calibration of parameters

Calibration of relative permeability and thermal vapor flow diffusivity is performed by using the results by laboratory experiments carried out by SKB. Figure 6.44 shows the comparison between the results of infiltration test and simulation. The straight line is the result of laboratory test and dotted line is the result of simulation. Figure 6.45 shows the result of thermal gradient test by SKB. Figure 6.46 shows the result of simulation of thermal gradient test. The relative permeability k_r and thermal vapor flow diffusivity D_{Tv} used in the simulations are as follows

$$k_r = S_r^{3.0} \quad (6.22)$$

$$D_{Tv} = D_{Tvo} \left(\alpha \frac{T - T_0}{T_0} \right) \quad (6.23)$$

with $D_{Tvb} = 9.0 \times 10^{-12} \text{ m}^2/\text{s/K} = -0.4$ and $T_0 = 10^\circ\text{C}$, respectively.

For the rock mass, the water retention curve as shown in Figure 6.47 and the relative permeability as shown in Figure 6.48 are used. These unsaturated properties are based on the van Genuchten model in equations (6.24) and (6.25).

$$Se = \frac{\theta - \theta_r}{\theta_s - \theta_r} = \left[\frac{1}{1 + (a\psi)^n} \right]^{1-\frac{1}{n}} \quad (6.24)$$

$$k_r = Se^{1/2} \left[1 - (1 - Se^{1/m})^m \right]^2 \quad (6.25)$$

where, Se : effective saturation, θ : volumetric water content, θ_s : saturated volumetric water content, θ_r : residual volumetric water content, ψ : water potential (kPa), a , n , m : the coefficients of van Genuchten model with $a = 6.0 \times 10^{-4}$ (1/kPa), $n = 1.5$ and $m = 1-1/n$, respectively.

Re-analysis by using the calibrated parameters is performed. The analysis conditions are shown in Table 6.7. This analysis considers the excavation of tunnel before emplacement of engineered barrier system. Conditions at in the excavation are 50% R.H. and initial temperature of 13°C

Figure 6.49 shows the distribution of the water head along the horizontal line ($Y=0$ and $Z=0$) before and after the excavation of the tunnel in Case-C01. That is not so different from Case-A02. Figure 6.50 shows the distribution of degree of saturation of rock mass along the same line as in Figure 6.49. This degree of saturation of the rock mass is calculated by equation (6.24). It is shown that the unsaturated zone spreads out to distance of around 6m from the center of tunnel to the horizontal direction.

Figure 6.51 and Figure 6.52 show the distribution of the water head along the vertical line ($X=0$ and $Y=0$). In the vertical line, negative pressure occurs between -6m and 6m. Figure 6.53 shows the distribution of degree of saturation along the vertical line. Unsaturated zone spreads out to distance of around 6m from the center of tunnel to the vertical direction. Figure 6.54 shows the temperature distribution along the vertical line. Differently from Case-A02, the temperature remains at the initial value after the excavation of tunnel because the temperature at excavation tunnel is not changed.

Figure 6.55 shows the time history of the degree of saturation in the buffer after the emplacement of engineered barrier system. The degree of saturation decreases due to thermal gradient as shown in this analysis since the thermal vapor flow diffusivity is higher than in the previous case. The behaviors at points B1, B2 and B3 are almost the same and the degree of saturation after 3 years is the smallest, at approximately 30%. At point B13, the degree of saturation becomes the lowest after the approximately 10 years from the emplacement of engineered barrier system. The re-saturation time is approximately 50 years and it is later than that of Case-A02.

Figure 6.56 shows the time history of temperature in the buffer. The maximum temperature is approximately 60°C and it occurs after 4 years from the emplacement of engineered barrier system.

6.4 Conclusions

From the work of Task A-1, following conclusions were obtained.

By thermal analysis, effect of occupied area on maximum temperature in the buffer was examined. As a result, when length of X-axis is 12.5m and Y-axis is 2.8m (the smallest occupied area per container in this parametric study), maximum temperature in the buffer is under 100°C. At that time, occupied area per container is 35m².

From the preliminary THM analysis, following results were obtained. When the excavation of drift is considered at a RH50%, the re-saturation time is about 30 years. The maximum temperature is 63 °C after 4 years of emplacement of engineered barrier. After that, calibration of parameters of bentonite (unsaturated permeability, thermal vapor flow diffusivity and swelling pressure) was completed. By using these parameters, following results were obtained. When the excavation of drift is considered at a RH50%, the re-saturation time is about 50 years. The maximum temperature is 60 °C after 4 years of emplacement of engineered barrier.

References

- Börgesson, L. Johannesson, L.-E., Sanden, T. and Hernelind, J., *Modelling of the physical behaviour of water saturated clay barriers. Laboratory tests, material models and finite element application*, SKB Technical Report TR 95-20, SKB, 1995.
- Börgesson, L., Fredriksson, A. and Johannesson, L.-E., *Heat conductivity of buffer materials*. SKB Technical Report TR 94-29, 1994.
- Börgesson, L. and Hernelind, J., *Preliminary modeling of the water-saturation phase of the buffer and backfill material*, SKB IPR-00-11, 1999.
- Chijimatsu, M., Kurikami, H. and Sugita, Y., *Coupled Thermo-hydro-mechanical analysis of the Prototype Repository Project using numerical code THAMES, Large Scale Field Tests in Granite –Barrier Behaviour and THM Modelling*, Sitges, 2003.
- Ledesma, A. and Chen, G.J., *T-H-M Modelling of the Prototype Repository Experiment. Comparison with Current measurements Large Scale Field Tests in Granite –Barrier Behaviour and THM Modelling*, Sitges, 2003.

Table 6.1 Output points for thermal simulation

Point	X (m)	Y (m)	Z (m)
B1	0.585	0	0
B2	0	0	0.585
B3	0	0	-0.585
B4	0.96	0	0
B5	0.7725	0	0
B6	0	2.45	0
B7	0	-3.43	0
B8	0.585	2.45	0
B9	0	2.45	0.585
B10	0	2.45	-0.585
B11	0	0	Y_{\max}
B12	X_{\max}	0	0

Table 6.2 Property of rock mass

Property	Value
Thermal conductivity (W/mK)	3.0
Specific heat (kJ/kgK)	0.845
Density (kg/m ³)	2650
Porosity (%)	0.3

Table 6.3 analysis cases

Analysis case	X_{\max} (m)	Y_{\max} (m)
Case01	12.5	2.8
Case02	20.0	2.8
Case03	27.5	2.8
Case04	35.0	2.8
Case05	12.5	3.4
Case06	20.0	3.4
Case07	27.5	3.4
Case08	35.0	3.4
Case09	12.5	4.0
Case10	20.0	4.0
Case11	27.5	4.0
Case12	35.0	4.0

Table 6.4 Analysis case

Analysis case	Excavation	Condition at excavation part		
Case-A01	Not considered	—	—	—
Case-A02	Considered	RH50%	-9500m	25°C
Case-A03	Considered	Atmospheric	0m	25°C

Table 6.5 Output points for THM simulation

Points	X (m)	Y (m)	Z (m)
B1	0.585	0	0
B2	0	0	0.585
B3	0	0	-0.585
B4	0.96	0	0
B5	0.7725	0	0
B6	0	2.45	0
B7	0	-3.43	0
B8	0.585	2.45	0
B9	0	2.45	0.585
B10	0	2.45	-0.585
B11	0	0	2.8
B12	27.5	0	0
B13	0	0	1.95

Table 6.6 Property of rock mass

Property	Value
Density (kg/m ³)	2,650
Porosity (%)	0.3
Young's modulus (GPa)	60
Poisson's ratio (-)	0.202
Thermal conductivity (W/mK)	3.0
Specific heat (kJ/kgK)	0.845
Thermal expansion coefficient (1/°C)	1×10 ⁻⁵
Intrinsic permeability (m ²)	7×10 ⁻¹⁹

Table 6.7 Tabulated data of hydraulic conductivity k with function of void ratio e and temperature T for the SKB simulation

T [°C]	e	k [m/s]
20	0.4	0.035×10^{-13}
20	0.6	0.200×10^{-13}
20	0.8	0.650×10^{-13}
20	1.0	1.750×10^{-13}
40	0.4	0.050×10^{-13}
40	0.6	0.310×10^{-13}
40	0.8	1.000×10^{-13}
40	1.0	2.750×10^{-13}
60	0.4	0.070×10^{-13}
60	0.6	0.440×10^{-13}
60	0.8	1.450×10^{-13}
60	1.0	3.850×10^{-13}
80	0.4	0.100×10^{-13}
80	0.6	0.550×10^{-13}
80	0.8	1.800×10^{-13}
80	1.0	4.900×10^{-13}

Table 6.7 Analysis condition after calibration

Analysis case	Excavation	Condition at excavation part	
		Case-C01	Considered

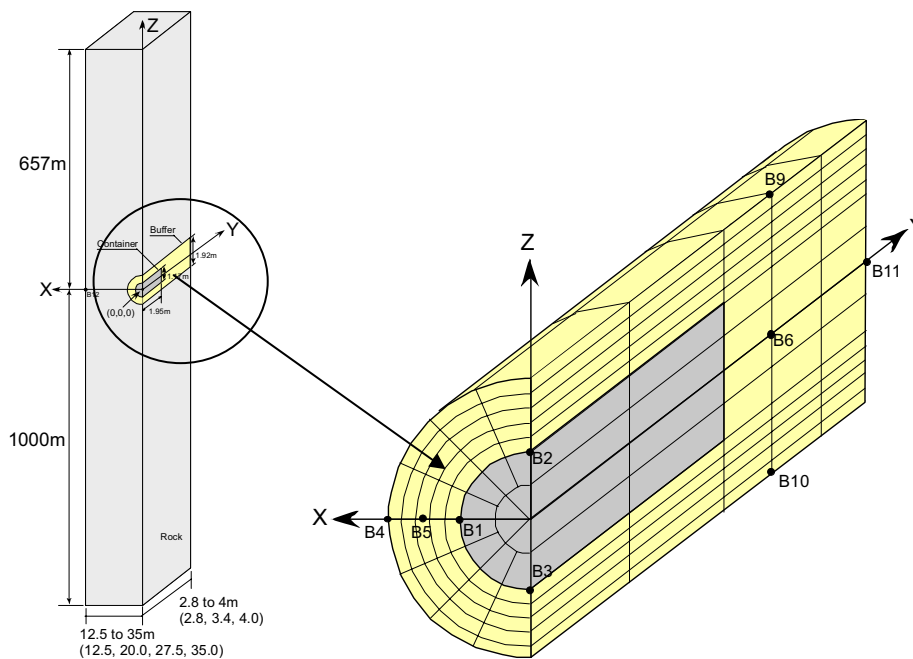


Figure 6.1 Geometry and output points for thermal simulation

7. Comparison and discussion

7.1 Comparison of Task A-1 Results between models

All research teams used models with full THM coupling capabilities. For all teams (except STUK), the governing equations in these models were derived from an extension of Biot's theory of poroelasticity (Chijimatsu et al., 2006) in order to include thermal effects, variable degrees of saturation, and swelling behaviour of bentonite.

The STUK team uses a multiphase flow model (Jussila, 2006) and considers both gas and liquid flow in a porous medium. The model is based on thermomechanics and mixture theory and describes the behaviour of the mixture via proper choices of free energy and dissipation function.

Transient analysis was performed by all teams according to the following sequence:

- i) Perform first a steady state HM analysis to establish pre-excavation conditions using the boundary conditions (cf. Figs. 1.11 and 1.12).
- ii) Perform a transient HM analysis for 30 years to simulate the excavation phase of the repository. The borehole is assumed to be open during that phase, with a relative humidity maintained between 50 to 100%.
- iii) At time 30 years, assume all boreholes are instantaneously filled with containers and bentonite. The container heat output is consistent with CANDU fuel characteristics (cf. Figure 1.13), and the transient THM analysis is performed for up to 1000 years.

The main input parameters of the models for the bentonite and rock mass are given in Chapter 1. Basic properties such as Young modulus of the rock and thermal properties of the rock and the bentonite are relatively well defined, and there is not much difference in the input values used by the teams. On the other hand, the special properties required for coupling between processes and as dictated by specific features of the different models are not available at this stage, and the teams have to rely on past experience with similar projects in order to come with best estimates for these values. Even so, there is considerable consistency between the results as follows.

The maximum temperature is developed near the waste canister (point B1 shown in Figure 1.14). Figure 7.1 shows the results for temperature evolution from different teams. All teams used well-defined thermal properties of the bentonite that vary as a function of the moisture content. All teams consistently found that the peak temperature of approximately 60°C occurs within 10 years after waste emplacement.

The evolution of the degree of saturation at point B1 in the buffer is shown in Figure 7.2. All teams found that there is a de-saturation of the buffer near the canister due to vapour flow from the heat source, followed by a resaturation. Most teams predict that resaturation would be complete within 10 years after wastes emplacement, except for STUK with a re-saturation time of 40 years.

The evolution of total stress in the buffer near the canister is shown in Fig. 7.3. The total stress is the sum of pore pressure, swelling pressure and thermal stresses. CNSC, JAEA, SKB and SKI obtained maximum compressive stresses of approximately 15 MPa. The STUK team did not take into account swelling pressure; consequently their maximum stresses are much smaller compared to the other teams. The CNSC, SKB and JAEA predict that the maximum stress is attained within the first 10 years after wastes emplacement, while SKI predicts a much longer time beyond 1000 years. This difference is due to the predicted time when full hydrostatic pressure is re-established, as discussed later.

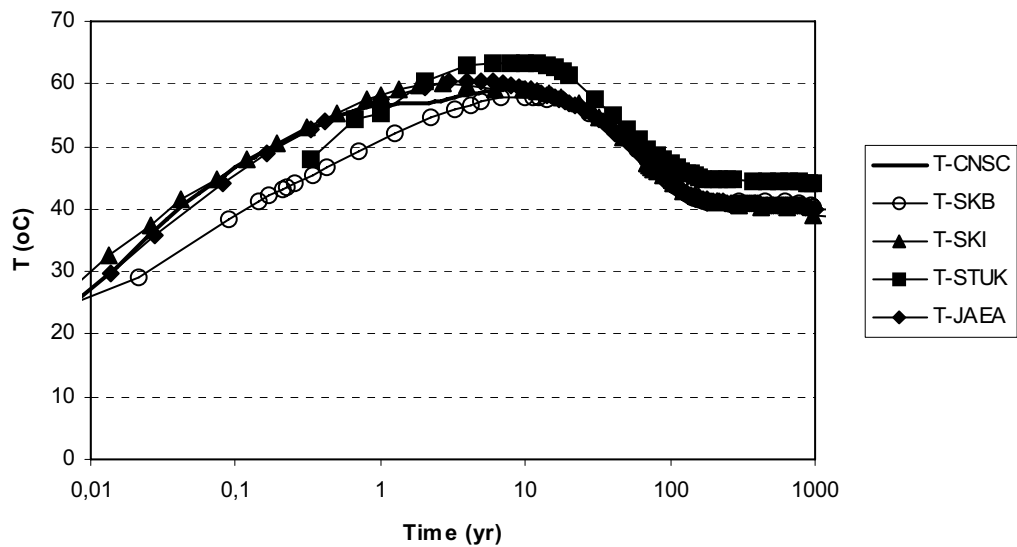


Figure 7.1 Temperature in buffer at container.

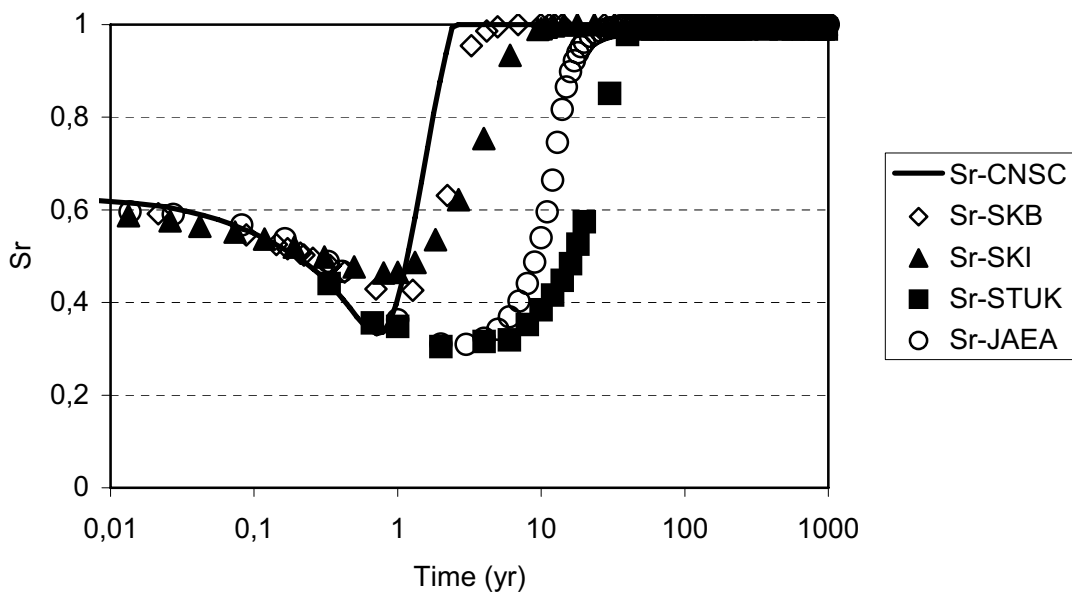


Figure 7.2 Buffer resaturation at container

Most teams predict local failure of the rock mass around the borehole. For example, SKI's results for effective stress (total stress minus pore pressure) evolution at the top and the sidewall of the borehole are illustrated in Fig.7.4. The stresses at these two points are compared with the Hoek-Brown failure criterion. It is shown that at the top of the borehole, failure of the rock can occur right after excavation due to an increase of the major principal stress and a decrease of the minor principal stress. For the point on the sidewall, excavation induces a decrease in both minor and major principal stresses. At waste emplacement, these stresses increase due to a combination of buffer swelling and thermal effects. However, when the hydrostatic pressure gradually re-establish, these stresses decrease again, and failure in tension is predicted within 1000 years after wastes emplacement.

The change in the stress regime would change the permeability in the rock mass. For example, as shown in Figure 7.5, SKB team predicts that due to an increase in the mean stress, a practically impermeable zone is formed at 70 years on the top and bottom of the borehole. On the other hand, due to stress decrease, the sides of the borehole would experience an increase of permeability by one order of magnitude. It should be noted that these results are based on the assumption of linear elastic behaviour of the rock mass and empirical functions relating permeability to the change in volumetric strain (or compressive stress) in the rock (cf. Fig 1.15).

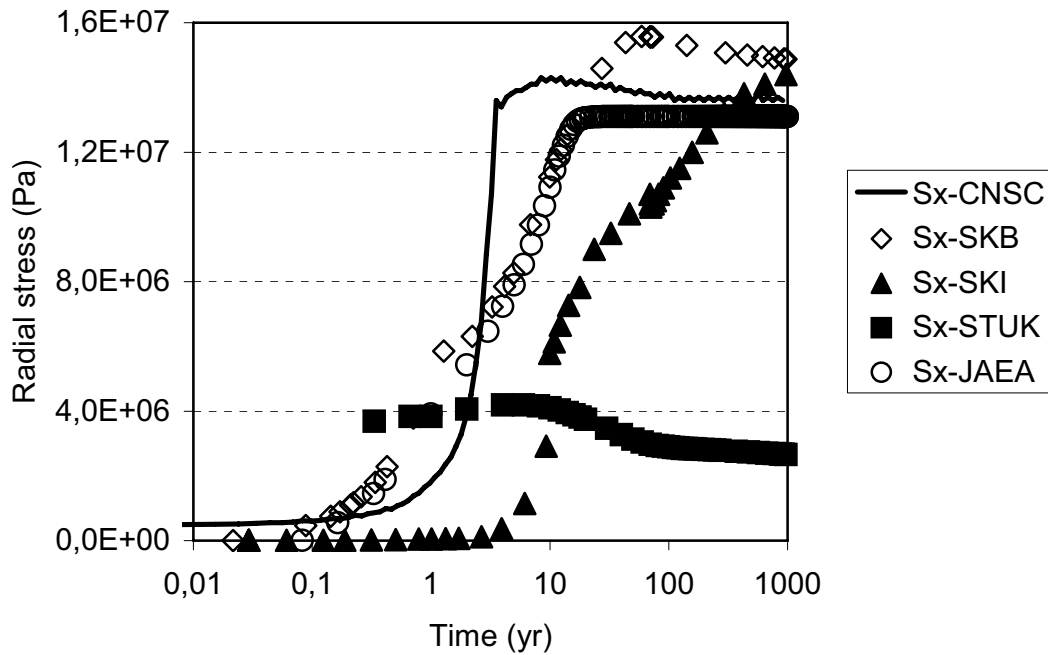


Figure 7.3 Total stress in buffer at container

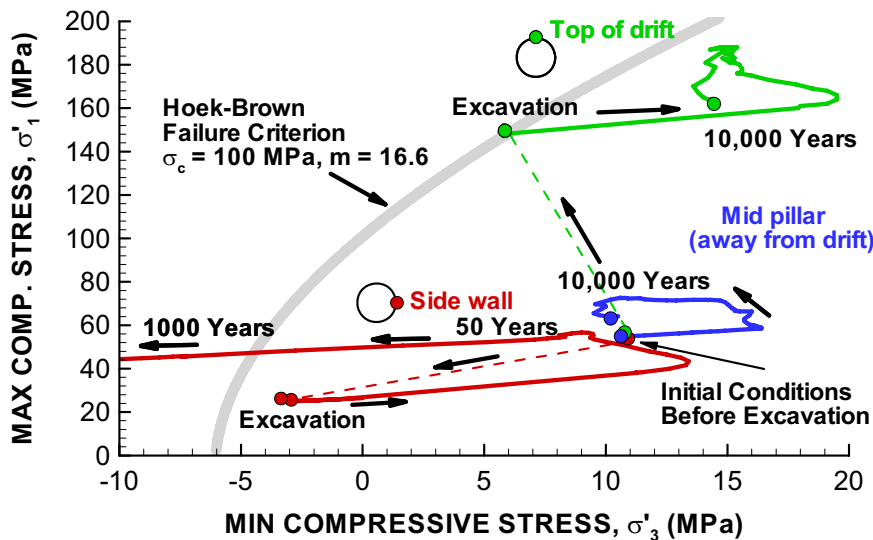


Figure 7.4 Effective stress evolution and failure conditions around the drift (SKI team's results)

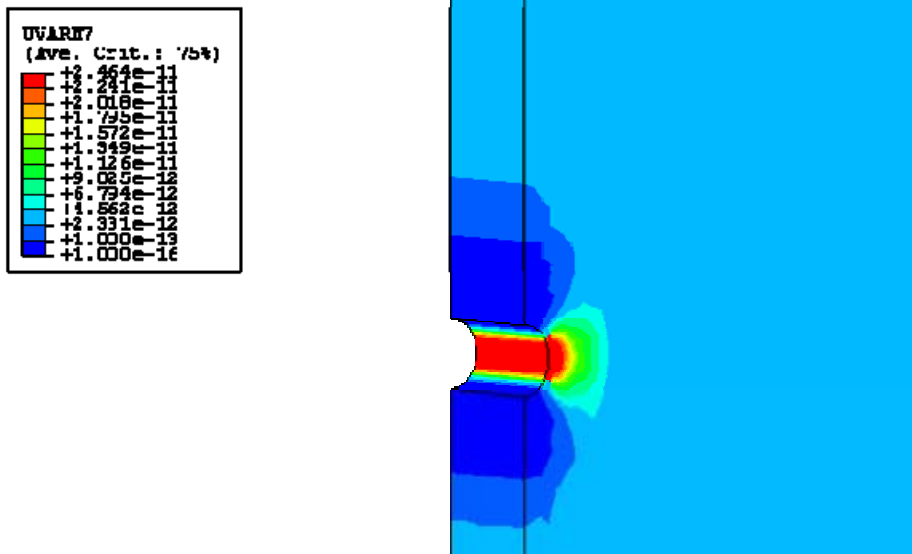


Figure 7.5 Permeability(m/s) of rock mass 70 years after waste emplacement (from SKB team's results)

The predicted time when full hydrostatic pressure is re-established at the repository level depends on the assumed permeability function for the rock used by the different teams. It also depends on whether the team assumed an initial relative humidity of 100% or less in the borehole during the 30 years operational period of the repository. Assuming a 50% relative humidity would induce de-saturation of the rock mass during that period and subsequently, a full hydrostatic re-establishment of the water pressure would take longer. The results for pore pressure evolution at point B4 (indicated on Figure 4) in the rock mass are compared in Figure 7.6. It is shown that SKI and JAEA predict a longer period for full restoration of the hydrostatic stress as compared to CNSC and SKB.

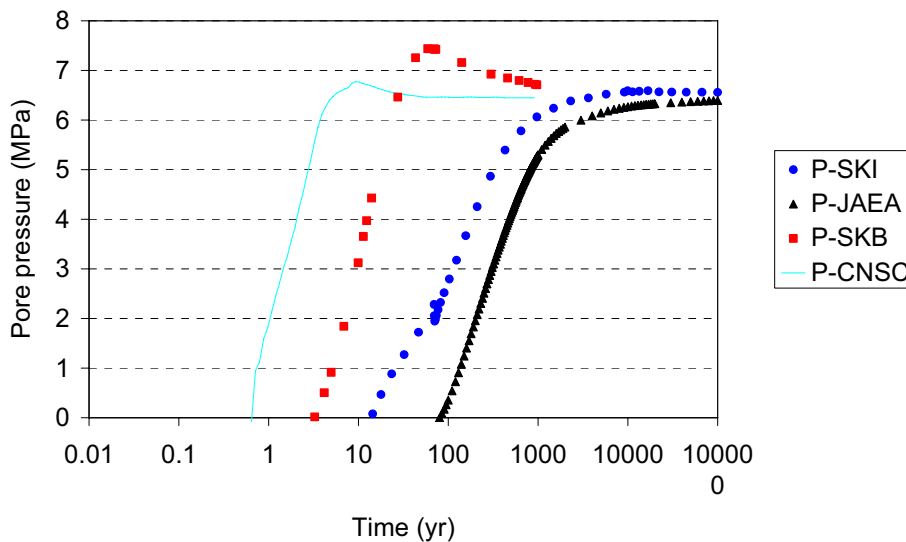


Figure 7.6 Pore pressure evolution in rock mass near buffer on sidewall.

7.2 Concluding remarks

The ultimate objective of any research program related to geological disposal of nuclear wastes should be to provide additional confidence on the long term performance of the repository. In the international DECOVALEX-THMC project, researchers have been developing coupled THMC mathematical models in order to predict the long term evolution of the repository for different scenarios. The results of these predictions should be communicated to the SA analysts so that they can be considered in system models for predicting the overall performance of the repository. In this paper we presented the definition of a Task A of the project which is a working example of how interaction between THMC modelling and SA analysis could be performed. We also presented results of preliminary THM calculations by the teams involved in the project. The purpose of the preliminary THM modelling is to have an initial appreciation of the phenomena and properties that must be better understood in subsequent phases. Many simplifications and assumptions were introduced and the results should be considered with caution. However, a few points of concern were identified and would guide us in the next phases of the project:

1. The predicted maximum total stress in the MX-80 bentonite could slightly exceed the 15 MPa design pressure for the container. The MX-80 bentonite exhibits very nonlinear THM behaviour and small variations in the assumed input properties could significantly influence the results. A systematic model calibration with laboratory data will have to be performed in order to predict stresses in the bentonite with more confidence.
2. The preliminary results show that a damage zone could be formed around the waste emplacement boreholes; the extent of this damage zone, as well as its hydraulic and mechanical properties, should be better predicted.
3. In addition to unsaturated properties of both the rock and buffer, the variation of rock permeability with stress or strain could have significant effects on the re-saturation time of the bentonite. Permeability functions specific to the granite under consideration will have to be developed.

In preparation for a final THM model of the test case considered here, our next step would be to refine constitutive relationships and parameters for both the bentonite and the granite, using data from laboratory and in-situ tests. Some results of these efforts are presented by Chijimatsu et al. (2006).

References

- Borgesson, L. & Hernelind, J. 1999. *Coupled thermal-hydro-mechanical calculations of the water saturation phase of a KBS-3 deposition hole- Influence of hydraulic rock properties on the water saturation phase*. SKB report TR-99-41, SKB, 102 40 Stockholm, Box 5864.
- Chijimatsu, M., Nguyen, T.S., Jing, L., De Jonge, J., Kohlmeier, M., Millard, A., Rejeb, A., Rutqvist, J., Souley, M. & Sugita Y. 2005. *Numerical study of the THM effects on the near-field of a hypothetical nuclear waste repository-BMT1 of the DECOVALEX III project. Part 1: Conceptualization of the problems and summary of results*. Int. J. Rock Mech. And Min. Sci. 42 (5-6).

- Chijimatsu, M., Borgesson, L., Fujita, T., Hernelind, J., Jussila, P., Nguyen, T.S., Rutqvist, J. & Jing L. 2006. *Model calibration of small and large scale laboratory THM experiments of the MX-80 bentonite*. Proc. GeoProc 2006.
- Garisto, F., Avis, J., Calder, N., Gierszewski, P., Kitson, C., Melnyk, T., Wei, K. & Wojciechowski, L. 2005. *Horizontal borehole concept case Study*. OPG, NWMD, 700 University Avenue, Toronto, Ont. Canada M5G 1X6, report 06819-REP-01200-10139-R00
- Gierszewski, P., Avis, J., Calder, N., D'Andrea, A., Garisto, F., Kitson, C., Melnyk, T., Wei, K. & Wojciechowski, L. 2004. *Third case study – postclosure safety assessment*. OPG, NWMD, 700 University Avenues, Toronto, Ont. Canada M5G 1X6, report 06819-REP-01200-10109-R00.
- Herget, G. & Arjang, B. 1990. *Update on ground stresses in the Canadian Shield*. Proc. Specialty Conf. Stresses in Underground Structures, Ottawa, Canada. CANMET, Canadian Government Publishing Centre Supply and Services, Ottawa, Canada.
- Jussila, P. 2006. *Thermo-hydro-mechanical model for unsaturated swelling porous medium-application to Task A of the Decovalex THMC project*. Proc. GeoProc 2006.
- Millard, A., Rejeb, A., Chijimatsu, M., Jing, L., De Jonge, J., Kohlmeier, M., Nguyen, T.S., Rutqvist, J., Souley, M. & Sugita Y. 2005. *Numerical study of the THM effects on the near-field of a hypothetical nuclear waste repository-BMT1 of the DECOVALEX III project. Part 2: Effects of THM coupling in continuous and homogeneous rocks*. Int. J. Rock Mech. And Min. Sci. 42 (5-6).
- McMurry, J., Dixon, D.A., Garroni, J.D. Ikeda, B.M., Stroes-Gascoyne, S., Baumgartner, P. & Melnyk, T.W. 2003. *Evolution of a Canadian deep geologic repository. Base scenario*. OPG, NWMD, 700 University Avenues, Toronto, Ont. Canada M5G 1X6, report 06819-REP-01200-10092-R00,
- NEA. 2004. *Post-closure safety case for geological repositories*. Nuclear Energy Agency ISBN 92-64-02075-6
- NEA. 2005. *Linkage of geoscientific arguments and evidence in supporting the safety case*. Second AMIGO workshop, Toronto, Canada. Nuclear Energy Agency (in press).

www.ski.se

STATENS KÄRNKRAFTINSPEKTION
Swedish Nuclear Power Inspectorate

POST/POSTAL ADDRESS SE-106 58 Stockholm

BESÖK/OFFICE Klarabergsviadukten 90

TELEFON/TELEPHONE +46 (0)8 698 84 00

TELEFAX +46 (0)8 661 90 86

E-POST/E-MAIL ski@ski.se

WEBBPLATS/WEB SITE www.ski.se